

UNCLASSIFIED

AD NUMBER

ADB028457

LIMITATION CHANGES

TO:

Approved for public release; distribution is unlimited.

FROM:

Distribution authorized to U.S. Gov't. agencies only; Test and Evaluation; 13 JUL 1978. Other requests shall be referred to Army Missile Research and Development Command, Redstones Arsenal, AL 35809.

AUTHORITY

OASD ltr 27 Apr 1983

THIS PAGE IS UNCLASSIFIED

AD BD28457

AUTHORITY:

OASD 1527 Apr



DISCLAIMER NOTICE

**THIS DOCUMENT IS THE BEST
QUALITY AVAILABLE.**

**COPY FURNISHED CONTAINED
A SIGNIFICANT NUMBER OF
PAGES WHICH DO NOT
REPRODUCE LEGIBLY.**

128900-9-F1 (1)

LEVEL #2
B5

Final Technical Report

L-BAND RADAR CLUTTER STATISTICS FOR TERRAIN AND ICE

Volume I: Technical Discussion and Results

Electronic Systems Program Development Office

FEBRUARY 1978

~~Classification: Not Authorized~~
~~Released for Public Release~~
~~By [redacted]~~

DDC
REF ID: A
JUL 13 1978

Prepared for:
US Army Missile Research and
Development Command,
Redstone Arsenal, Alabama 35809

ID No.
DDC FILE COPY

ENVIRONMENTAL
RESEARCH INSTITUTE OF MICHIGAN
FORMERLY WILLOW RUN LABORATORIES, THE UNIVERSITY OF MICHIGAN
BOX 8618 • ANN ARBOR • MICHIGAN 48107

NOTICE

Sponsorship. This final report was submitted by the Electronic Systems Program Development Office of the Environmental Research Institute of Michigan, Ann Arbor, Michigan 48107, under Contract DAAK40-77-C-0112, Amendment P00002, with the U.S. Army Missile Research and Development Command, Redstone Arsenal, Alabama 35809. Mr. Samuel T. Uptain, Project Manager, DARPA Projects Office was the Contract Monitor. Mr. John McNamara, Rome Air Development Center/OCTF was the RADC Laboratory Project Engineer-in-Charge.

Disclaimer. The views and conclusions contained in this document are those of the authors and should not be interpreted as necessarily representing the official policies, either expressed or implied, of the Defense Advanced Research Projects Agency of the U.S. Government.

Distribution. ~~Unlimited distribution is authorized until cleared for public release by competent authority.~~

Final Disposition. After this document has served its purposes, it may be destroyed. Please do not return it to the Environmental Research Institute of Michigan.

UNCLASSIFIED

SECURITY CLASSIFICATION OF THIS PAGE (When Data Entered)

REPORT DOCUMENTATION PAGE		READ INSTRUCTIONS BEFORE COMPLETING FORM	
1 REPORT NUMBER	2. GOVT ACCESSION NO	3. RECIPIENT'S CATALOG NUMBER	
4. TITLE (and Subtitle) L-BAND RADAR CLUTTER STATISTICS FOR TERRAIN AND ICE, Volume I. Technical Discussion and Results.		(9) TYPE OF REPORT & PERIOD COVERED Final Report 26 July 1977 - Jan. 1978	
5. AUTHOR(S) A. Maffett, H. Klimach, A. Liskow, R. Rawson, R. Heimiller, and P. Tomlinson		(14) PERFORMING ORG. REPORT NUMBER 128900-9-F-1(I)	
6. PERFORMING ORGANIZATION NAME AND ADDRESS Environmental Research Institute of Michigan, P.O. Box 8618, Ann Arbor, Michigan 48107		(15) CONTRACT OR GRANT NUMBER(S) DAAK40-77-C-0112 ARPA Order-3169	
7. CONTROLLING OFFICE NAME AND ADDRESS Defense Advanced Research Projects Agency, 1400 Wilson Blvd., Arlington, VA 22209		10. PROGRAM ELEMENT, PROJECT, TASK & WORK UNIT NUMBERS Amendment Nr. P00002 Tech. Requirement Nr. N032	
11. MONITORING AGENCY NAME AND ADDRESS (if different from Controlling Office) U.S. Army Missile Research and Development Command, Redstone Arsenal, Alabama 35809		12. REPORT DATE February 1978	
13. NUMBER OF PAGES 101		14. SECURITY CLASS (of this report) Unclassified	
15. DECLASSIFICATION/DOWNGRADING SCHEDULE		16. DISTRIBUTION STATEMENT (of this Report) Distribution limited to U.S. Gov't. agencies only, Test and Evaluation; 13 JUL 1978. Other requests for this document must be referred to (abstract entered in Block 20, if different from Report) 17. DISTRIBUTION STATEMENT (of abstract entered in Block 20, if different from Report) 12 108p. (10) am: DRDM5-NS	
18. SUPPLEMENTARY NOTES ARPA Order Number 3169 Effective Date of Contract: 17 May 1977 Contract Expiration Date: 31 January 1978		19. KEY WORDS (Continue on reverse side if necessary and identify by block number) Radar Clutter Measurements Radar Clutter Statistics Synthetic Array Radar 20. ABSTRACT (Continue on reverse side if necessary and identify by block number) This final report addresses radar clutter statistics for terrain and ice and the generation of clutter data tapes by means of a radar signal simulation. These data cover pack ice (and refrozen lead), bare mountains, tundra and black ice. For comparison purposes, data are also included for a city (Toronto) and three homogeneous fields. These clutter data are described by statistical quantities. The clutter data	

DD FORM 1473 EDITION OF 1 NOV 65 IS OBSOLETE
1 JAN 73

UNCLASSIFIED

SECURITY CLASSIFICATION OF THIS PAGE (When Data Entered)

408 392

AB

UNCLASSIFIED

SECURITY CLASSIFICATION OF THIS PAGE (When Data Entered)

20. ABSTRACT (continued)

sigma sub 0

for the pack ice, bare mountain, and field provide σ_0 values which are in reasonable agreement with the small amount of L-band clutter data presently existing in the literature.

A description is also given of a radar signal simulation which was used to provide magnetic tape data for use in testing radar signal processor techniques. This simulation is capable of accepting as input the clutter data and statistics generated on this program. ↗



UNCLASSIFIED

SECURITY CLASSIFICATION OF THIS PAGE (When Data Entered)

FOREWORD

This document is the final report for Contract DAAK40-77-C-0112, Distributed Spaceborne Radar Study, Amendment P00002, L-band Radar Clutter Statistics for Terrain and Ice covering the period from 26 July 1977 to 31 January 1978. The analyses and studies described in this report were conducted principally in the Radar and Optics Division of the Environmental Research Institute of Michigan (ERIM), P.O. Box 8618, Ann Arbor, Michigan 48107 and by a subcontractor, Decision Science Applications, Inc. (DSA), 1500 Wilson Blvd., Arlington, Virginia 22209. The effort was sponsored by U.S. Army Missile R&D Command, DARPA Projects Office and Rome Air Development Center. Mr. Samuel T. Uptain, Project Manager, DARPA Projects Office, U.S. Army Missile Research and Development Command/DRDMI-NS was the Contract Monitor. Mr. John McNamara, Rome Air Development Center/OCTF was the RADC Lead Engineer-in-Charge. The Program Manager at ERIM was R. C. Heimiller, the principle investigator on this task was R. Rawson. Prof. Andrew Maffett, a consultant for ERIM was responsible for the clutter statistical analysis. Ms. Abby Liskow was responsible for generating the clutter statistics from radar data using computer programs generated by Mr. Herb Klimach.

The Program Manager at DSA was Mr. Jerry Belyea. Dr. Guy Ackerson and Philip Tomlinson of DSA performed radar signal analysis and derived the programs for generating the magnetic data tapes.

CONTENTS

Volume I

1. INTRODUCTION.....	1
1.1 Background and Objective.....	1
1.2 Summary of Report.....	2
2. LABRADOR TEST DATA.....	4
2.1 Data Measurement and Recording Method.....	4
2.1.1 Radar Imagery of Selected Test Sites.....	6
2.1.2 Digitization of Radar Images.....	10
2.2 Data Processing.....	17
2.2.1 Calibration of Radar Data.....	17
2.2.2 Clutter Distribution Software Documentation.....	36
3. STATISTICS FOR TERRAIN CLUTTER.....	43
3.1 Standard Statistics and Correlation.....	43
3.2 Fitting Data with Standard Frequency Distributions.....	45
3.2.1 Normal, Log-Normal, and Gamma Distributions.....	46
3.2.2 Other Distributions.....	53
3.2.3 Contaminated Distributions.....	54
3.2.4 Statistical Tests.....	56
3.3 Distributions for Various Terrain Clutter Types at Various Resolution Sizes.....	60
3.4 Correlation Results.....	74
4. SIMULATION OF RADAR SIGNALS FROM AN R, \hat{R} CLUTTER MAP.....	81
5. SUMMARY.....	91
6. CONCLUSIONS AND RECOMMENDATIONS.....	95
REFERENCE LIST.....	99

Volume II

APPENDIX I - STATISTICAL DISTRIBUTIONS OF CLUTTER DATA.....	1
APPENDIX II - DISTRIBUTION COMPUTER PROGRAM.....	333
APPENDIX III - DIGITAL TAPE LOGS.....	343

FIGURES

1. X-L Band Radar--Complete Route Imaged.....	5
2. Data Flow Diagram.....	7
3. Radar Image of Pack Ice.....	8
4. Radar Image Mountainous Terrain, File No. 1.....	9
5. Radar Image Mountainous Terrain, File No. 3.....	11
6. Radar Image of Toronto, Ontario.....	12
7. Radar Image of Field A.....	13
8. Radar Image of Field B.....	14
9. Radar Image of Field C.....	15
10. Radar Resolution Cell.....	16
11. CCT Data Format.....	18
12. Radar Image of Corner Reflectors at Goosebay Airport.....	20
13. Relative Calibration Curve.....	24
14. Intensity Vs. Depression Angle.....	28
15. Computer Numbers Vs. Depression Angle.....	29
16. Plot of Computer Numbers Vs. Depression Angle for Constant γ	33
17. Plot of Computer Numbers Vs. Depression Angle for Constant σ_0	35
18. Plot of Computer Numbers Vs. σ_0	37
19. Computer Program Flow Chart.....	39
20. Histogram and Normal Density Fit for Pack Ice.....	47
21. Cumulative Distribution for Pack Ice.....	48
22. Histogram and Fitting Log-Normal Distribution for Pack Ice...	50

FIGURES (Continued)

23. Mountainous Terrain (x) with Log-Normal Fit (-).....	51
24. Histogram for Bare Mountain Data and Gamma Density Fit.....	57
25. Histogram for Bare Mountain Data and Contaminated Gamma Density Fit.....	58
26. Histogram for Bare Mountain Data and Contaminated Gamma Density Fit.....	59
27. Standard Deviation Vs. Resolution.....	69
28. Comparison of Histograms.....	72
29. Comparison of Histograms.....	75
30. Correlation Coefficients.....	78
31. Correlation Coefficients.....	80
32. Comparison of L-Band Clutter Data from Various Terrain Types.....	92

TABLES

1. L-band Radar Cross Section of Corner Reflector at Goosebay....	21
2. Calculated Intensity Variation.....	23
3. Computed and Measured Intensity Values.....	25
4. Apparent Reduction in RCS of Corner Reflectors.....	27
5. Values of γ and Computer Numbers.....	32
6. Relation of Computer Numbers to σ_0 Values.....	34
7. Normalization Factors for All IPL Tapes.....	38
8. Data Inventory.....	62
9. Figure Numbers.....	67
10. Fitting Distributions.....	73

1
INTRODUCTION

This is the final report on the clutter statistics task on Contract DAAK40-77-C-0112, Distributed Spaceborne Radar Study. On this task, Amendment P0002 to the contract, the Environmental Research Institute of Michigan (ERIM) with the assistance of Decision-Science Applications, Inc. (DSA) as subcontractor obtained the radar clutter distributions of L-band data collected on recent flights of the ERIM X-L band SAR (synthetic array radar) system and generated clutter tapes by means of a radar signal simulation. The principle tasks included:

1. SAR image data digitization,
2. SAR image data calibration,
3. obtaining radar clutter cross-section distributions,
4. generating clutter models,
5. preparing radar system models, and
6. generating clutter tapes, and synthesizing target signals.

1.1 BACKGROUND AND OBJECTIVE

The objective of this program was to produce clutter distributions of three different terrain types at three different elevation angles and at two different resolutions. These clutter statistics would be used as realistic inputs for radar clutter models.

A meeting was held at ERIM with representatives from RADC, DSA, and ERIM to determine the values of the parameters described above. As a result of this meeting, the L-band horizontal transmission-horizontal receive data collected by ERIM, of Labrador, Canada, during February and March, 1977 was selected as the data set. Data at 20°, 30°, and 60° depression angles would be used. An angular interval of 2° centered on these 3 depression angles would be digitized. The

scenes selected were to include mountains, ice, and a city. The data would be analyzed at 3 meter resolution and 30 meter resolution.

The general approach used was to form a radar image using the optical processor. This optical image would be converted to a digital format using ERIM's image dissector facility. The dissected and digitized image would be stored on CCT's in a format suitable for statistical analysis using the University of Michigan's computer. After the numerical analysis had been performed, the numbers stored on tape would be converted to σ_0 values.

1.2 SUMMARY OF REPORT

This report is divided into 6 sections (Volume I) and 3 appendices (Volume II). This first section, the Introduction, briefly describes the objectives of the program and the methods used to satisfy these objectives.

Section two, Test Data, of the report describes the data selected for analysis and how the data was converted from optical images to clutter statistics. Included in section two are digitization and calibration methods.

Section three, Statistics for Terrain Clutter, describes the data analysis and discusses the distributions used to fit the data. Examples of the density distribution and cumulative distributions for various terrain are given in this section.

Section four, Simulation of Radar Signals from an R, R Clutter Map, taken from a technical memorandum by Philip Tomlinson of DSA, describes a method of generating simulated radar signals using clutter statistics.

Section five, Summary, summarizes the results and compares the results obtained from this program to results published in the literature. Section six contains the Conclusions and Recommendations.

Appendix I consists of copies of the computer print-out of the statistics generated on this program. Appendix II is a copy of the computer program and is included to make the documentation complete. Appendix III is a copy of the IPL logs associated with each data file generated during this program. Its function is to allow the data user the opportunity to retrace the data back to its origin, namely the radar imagery archived at ERIM. Thirty-seven different data files were generated on this program and are stored on 9 CCTs in ERIM's radar image library.

This section describes the test sites, shows examples of radar imagery of these test sites, and discusses the digitization and calibration procedures used and the computer program which calculated the statistics. The radar imagery used in this program was collected by ERIM during February and March of 1977 as part of a program called "SAR-77" and sponsored by the Canadian Cold Oceans Resources Engineering Laboratory, Memorial University, St. John, Newfoundland. During SAR-77, four-channel imagery was obtained from Lake Erie along the St. Lawrence River to the Gulf of St. Lawrence, north to Goosebay and Hopdale, Labrador. The imagery continues from Goosebay to St. John, Newfoundland; from St. John, Newfoundland to Quebec City via New Brunswick; and finally, returning to Lake Erie along the St. Lawrence River. A map of this route is shown in Figure 1. Each image swath appears in four separate output films corresponding to the four channels of radar data. These channels are:

- X-band parallel polarized,
- X-band cross-polarized,
- L-band parallel polarized, and
- L-band cross-polarized.

The majority of the data was collected using horizontal transmission although some data is available using vertical polarization for transmission. Although four-channel imagery is available, only the L-band parallel (horizontal transmit, horizontal receive) imagery was used in this program.

2.1 DATA MEASUREMENT AND RECORDING METHOD

Radar data is collected on board the imaging aircraft and stored as Doppler phase histories on photographic film. This film is called a signal film and is photographically developed after the aircraft

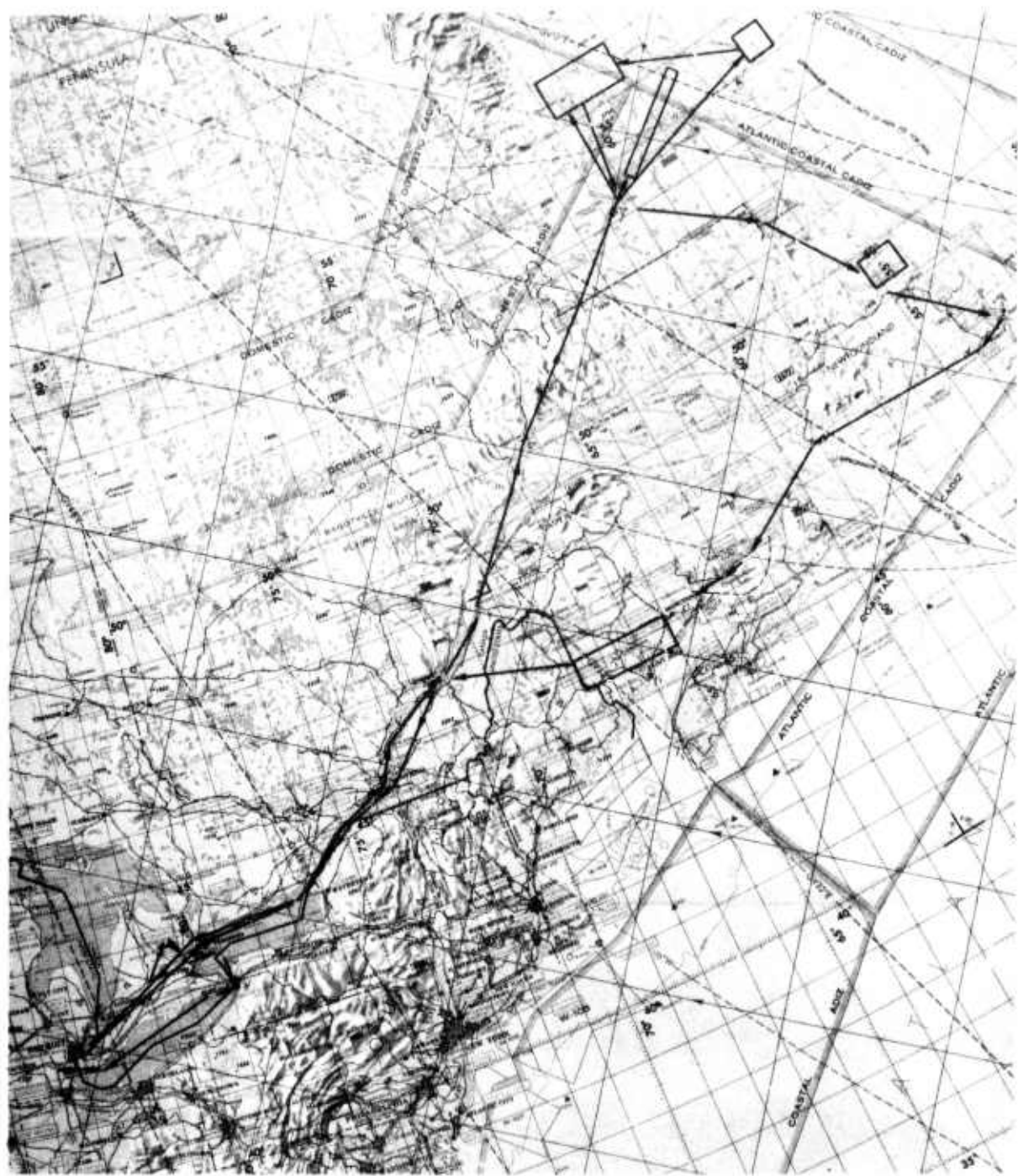


Figure 1. X-L Band Radar--Complete Route Imaged

lands. This film transparency is used as the input to the optical processor. The optical processor converts the Doppler histories into a radar image which normally is recorded on 70mm photographic film called the image film. On the image film, intense echo signals appear as high photographic density areas while weak radar echo components are low density areas.

Because one of the program goals was to generate clutter statistics, the image was converted into a digital tape for use in a digital computer. This is accomplished using a device called an image dissector. Similar to the optical image processor, the dissector converts data from the signal film to an optical image. Instead of storing this image on photographic film, it is (at this point) converted into numbers proportional to radar reflectivity (or square root of reflectivity) for each image element selected. These numbers are stored on computer compatible tape and are used as inputs to a digital computer to generate clutter statistics. This procedure is shown in block diagram form in Figure 2.

2.1.1 FADAR IMAGERY OF SELECTED TEST SITES

The ice imagery digitized was from the Labrador Sea and was selected because it contains both homogeneous pack ice and pack ice made nonhomogeneous by including large sections of refrozen leads. The refrozen leads are classified as black ice because of their appearance. A radar image of the pack ice is shown in Figure 3. The areas within the narrow strips are the areas digitized and used in the analysis.

As can be seen from Figure 4, there are many frozen mountain lakes in this selected scene of mountain terrain. During the analysis (section 3), it was noticed that the mountain data, at 30° depression angle, had a σ_0 about 10 dB below the σ_0 at 22° and 60°. Upon examination of the imagery, it was noticed that most of the data at 30° was shadowed by a mountain peak. A new area at 30° depression angle was

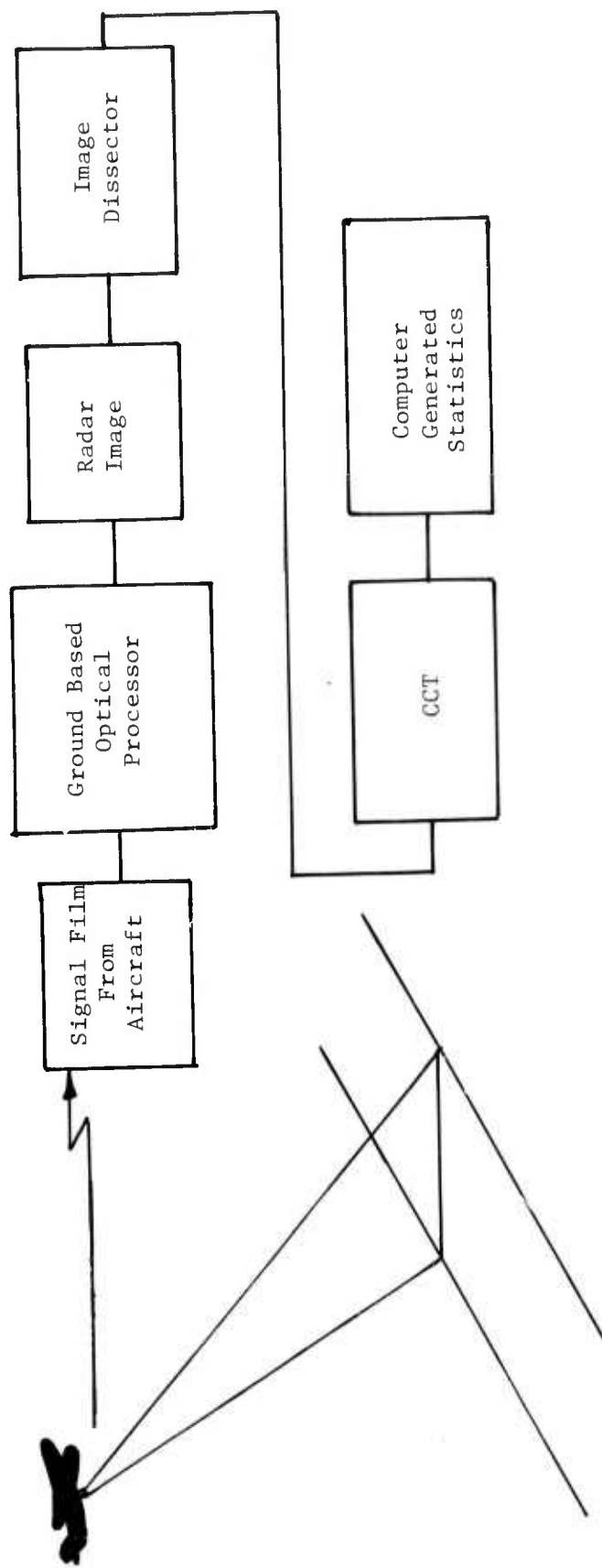


Figure 2. Data Flow Diagram

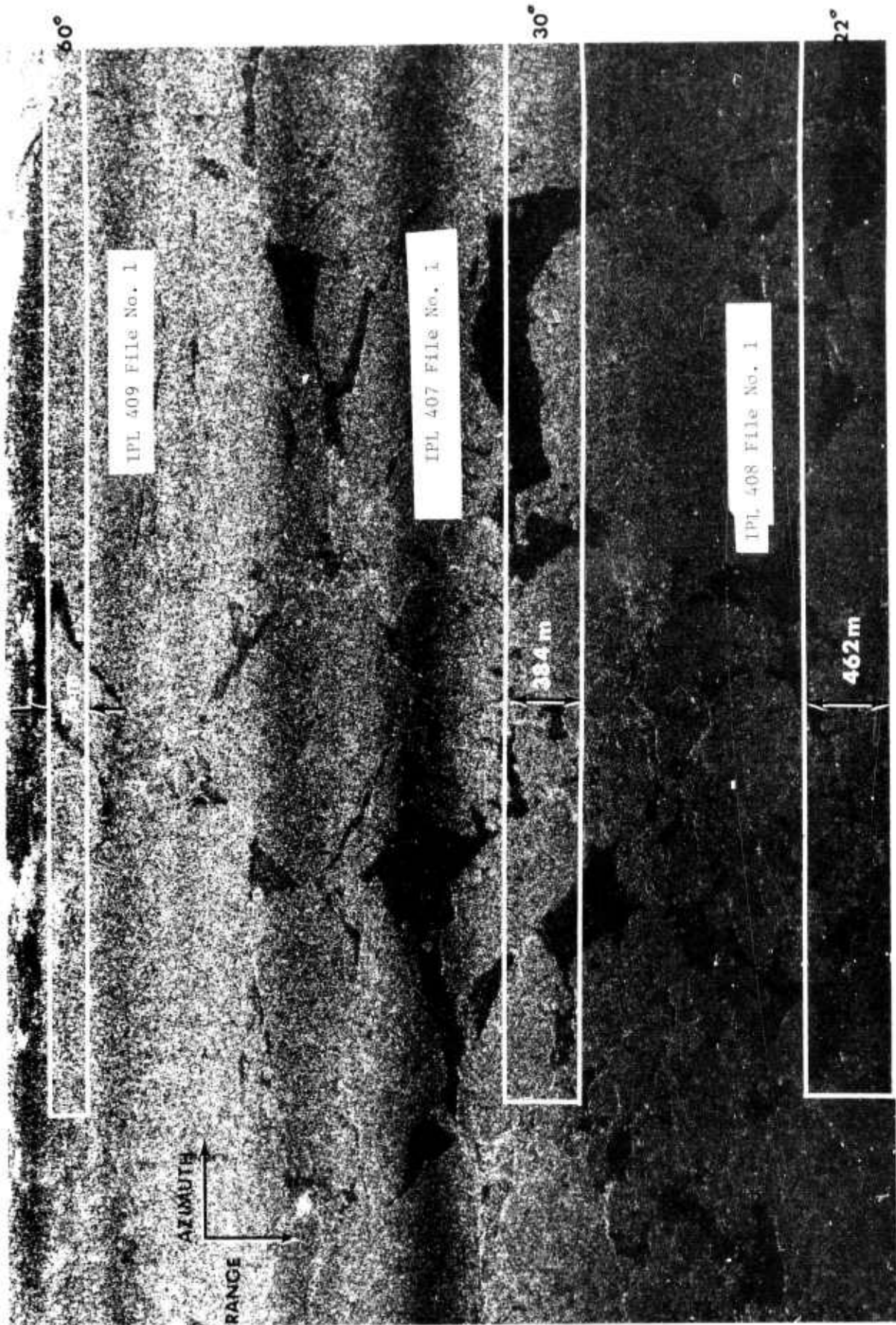
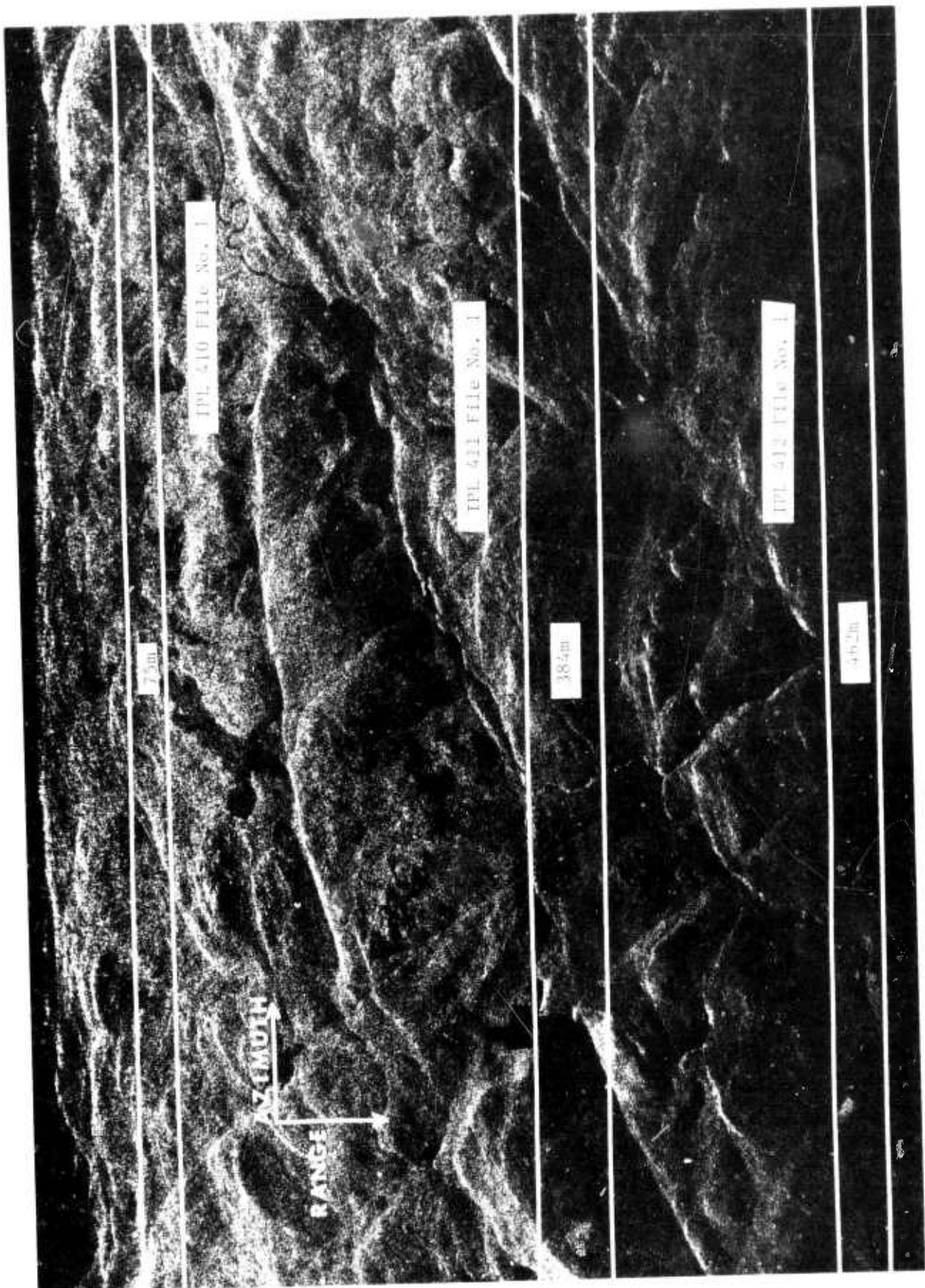


Figure 3. Radar Image of Pack Ice.

Figure 4. Radar Image Mountainous Terrain, File No. 1



selected and analyzed and its σ_0 value is more in agreement with the values at 22° and 60° . This area is shown in Figure 5.

The city of Toronto was used for the analysis of clutter statistics of cities. The entire scene shown in Figure 6 was digitized. Only the areas included in the narrow strips were used for analysis. Data from the large scene is available for future large area analysis.

The data from three "fields" in Ontario were digitized and analyzed to provide homogeneous data that would yield statistics which would be easier to interpret. Also its averaging characteristics should be better behaved than some of the nonhomogeneous clutter data. These fields subtend a small angular dimension in elevation so data were only digitized for one elevation angle. Radar images of the three fields are shown in Figures 7, 8, and 9.

2.1.2 DIGITIZATION OF RADAR IMAGES

As mentioned in section 2.1, the ERIM image dissector facility [1] was used to convert the radar images of various terrain types into computer compatible tapes. These CCT's were then used to compute the clutter statistics on the University of Michigan's Amdahl 470 computer. The software used to compute the statistics was developed on this program and is described in section 2.2.2.

The images used in this program were processed to a resolution cell of 3 meters in range and 4.5 meters in cross range or azimuth but was sampled by the image dissector using a 1.5 meter by 1.5 meter pixel size. This was accomplished by adjusting the optical magnification between the optical processor and the image dissector so that the radar azimuth resolution element was twice the size of the dissector azimuth resolution element. Figure 10.

To study the effect of different resolution on the clutter statistics, different quantities of data were averaged during the statistical computation process. All the initial image data was processed to 3 m by

1. D. A. Ausherman, "Radar Data Processing and Exploitation Facility, Record from the IEEE International Radar Conference, 1975.

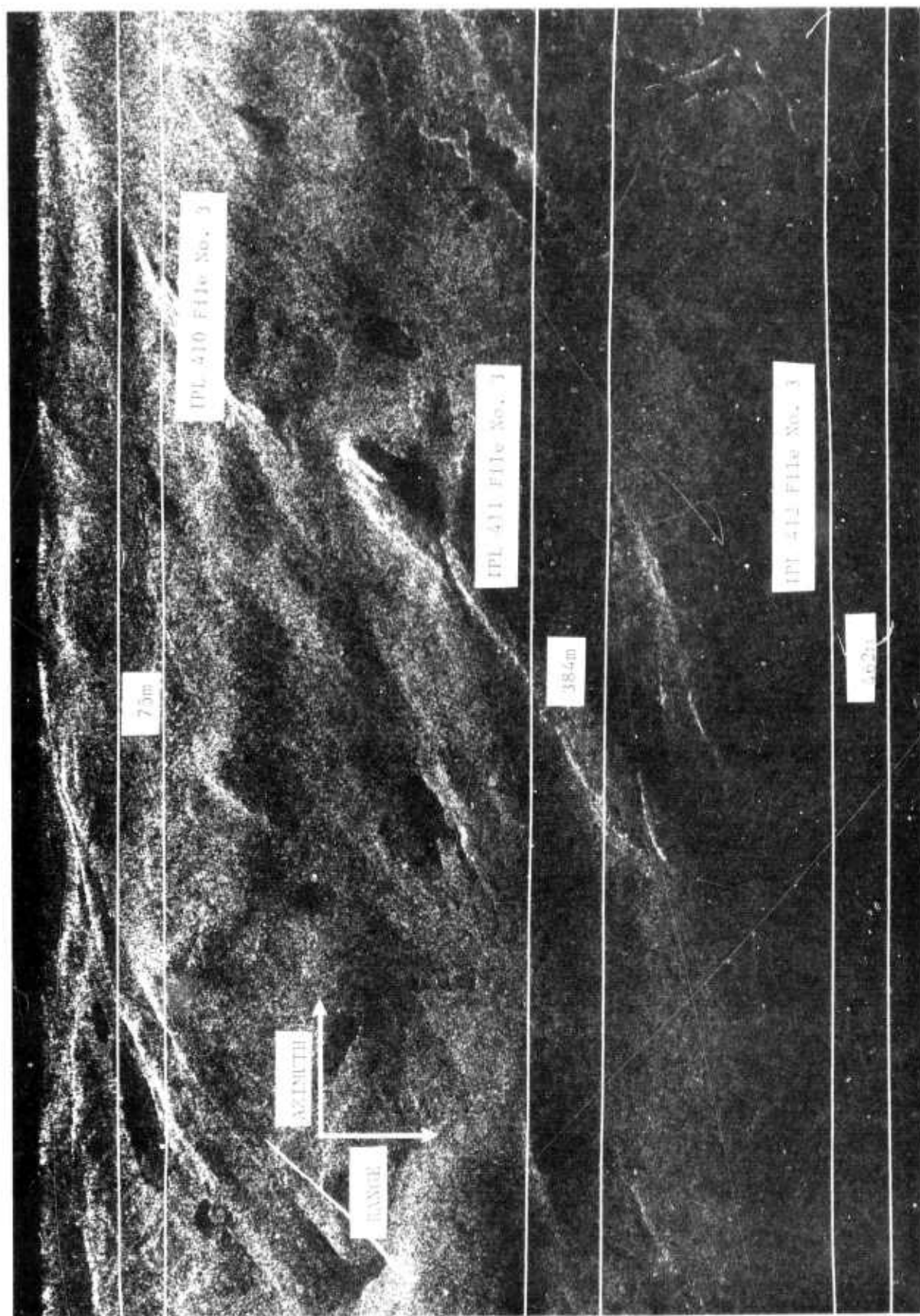


Figure 5. Radar Image Mountainous Terrain, File No. 3

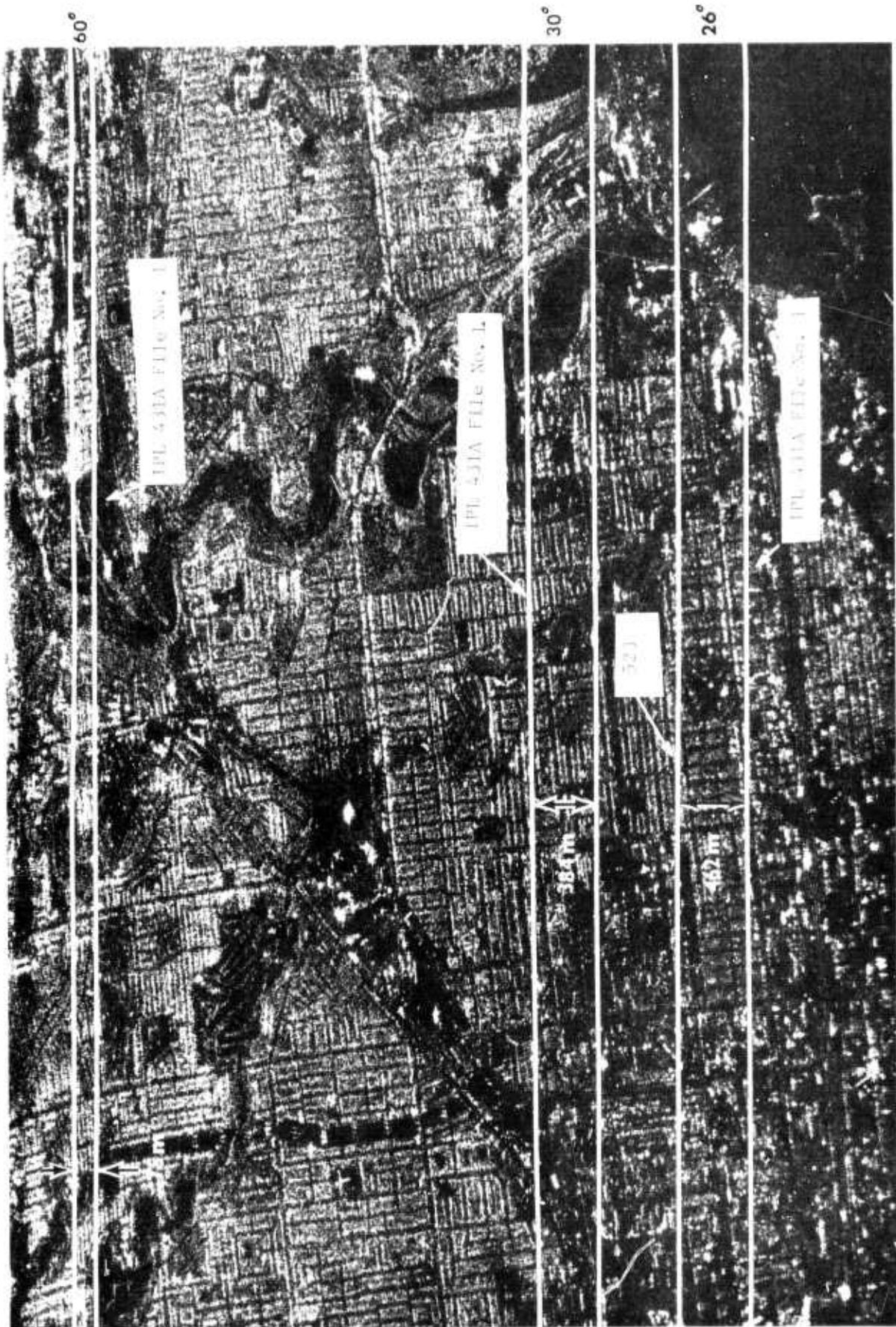


Figure 6. Radar Image of Toronto, Ontario



Figure 7. Radar Image of Field A.

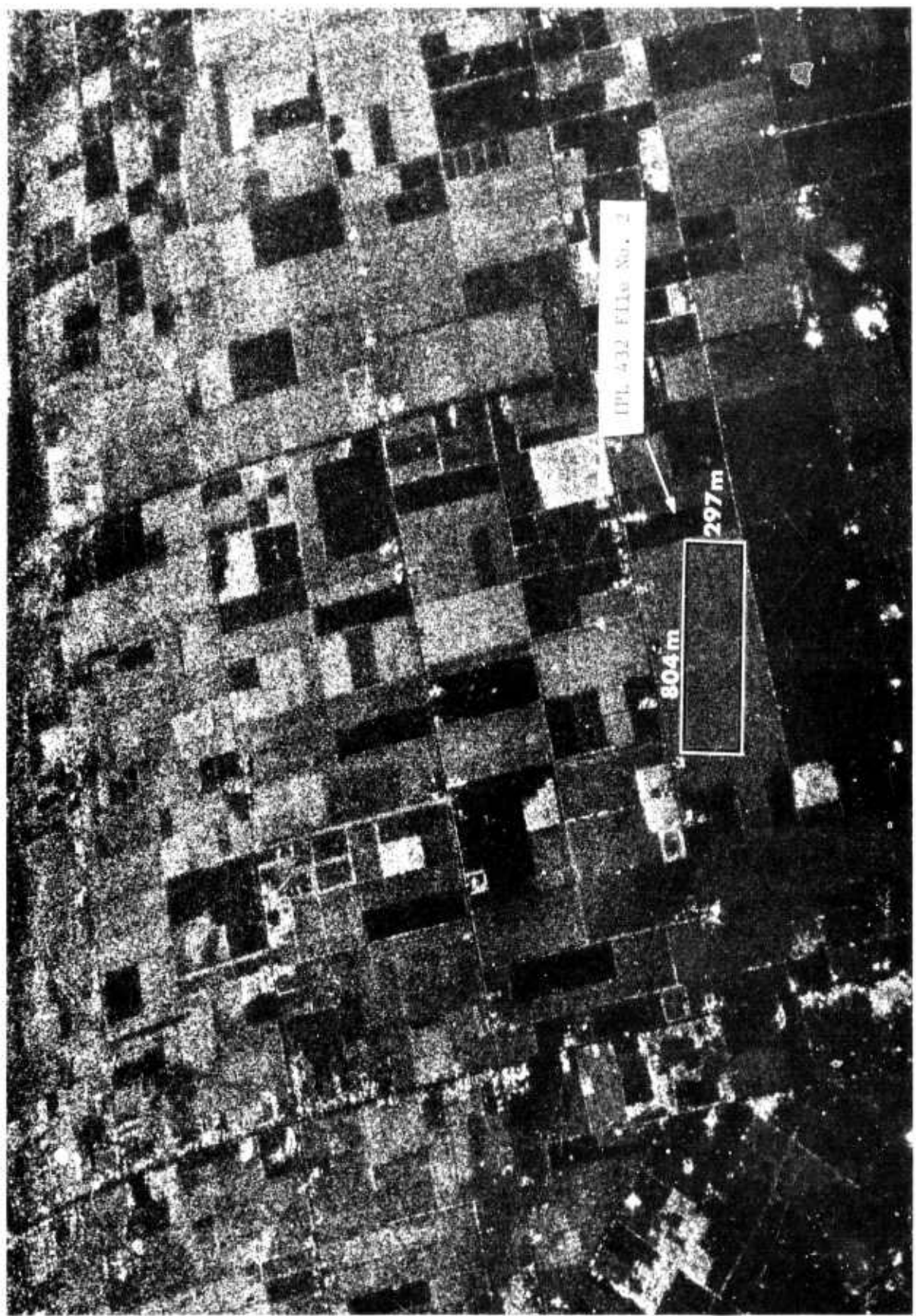
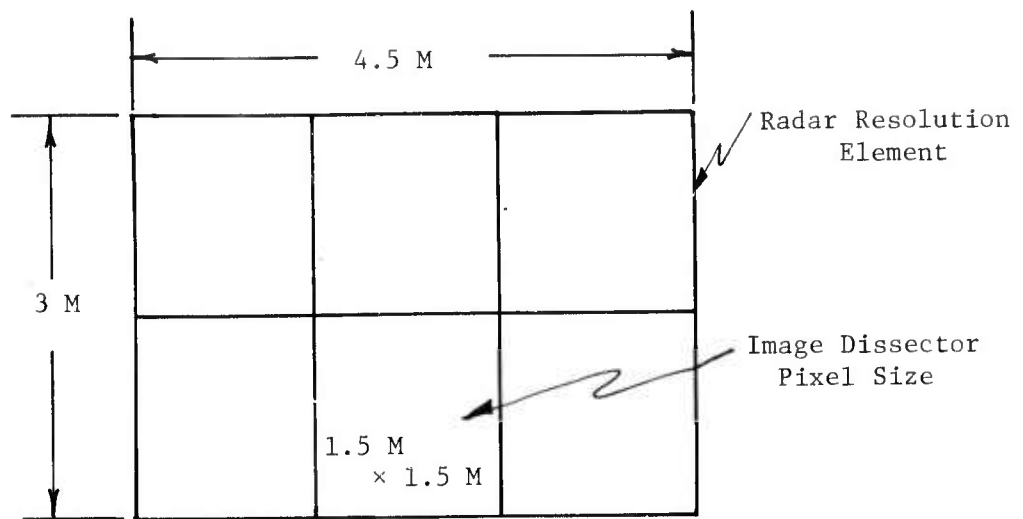


Figure 8. Radar Image of Field B.



Figure 9. Radar Image of Field C.



2 Pixels Per Range Resolution Element
3 Pixels Per Azimuth Resolution Element

Figure 10. Radar Resolution Cell

4.5 m resolution. The resolution of the clutter patches was then varied by changing the number of resolution cells averaged. Clutter patch resolution is determined by simply multiplying the pixel size by the averaging number. For example, 10 x 10 averaging will result in an effective resolution of the clutter patch of 15 m by 15 m. The 1 x 1 averaging is an exception, however, because the test resolution is restricted by the image resolution of 3 meter x 4.5 meter. Therefore, the clutter patch size for 1 x 1 averaging is 3 m by 4.5 m, not 1.5 m x 1.5 m.

The output of the image dissector facility is 9-track 800 BPI CCT. Each tape is given a unique number that is recorded in the ERIM image processing laboratory. This number is called the IPL number. Every scene digitized is recorded in a separate file on a tape. The length of the file is proportional to the size of the digitized scene. Each file is terminated by a single tape mark. The first record of each file consists of 120 byte ASCII characters. These characters are used to describe the contents of the file and are keyed in by the operator. The data files are composed of n records where n is the number of range scan lines to be digitized. The length of each record is determined by the number of image elements of pixels contained in a single range scan line and each pixel is represented by an 8-bit word. The maximum record length is restricted to 3000 pixels by the image dissector tube. The maximum scan length of the dissector is 30 mm. A schematic diagram of the CCT tape format is shown in Figure 11.

2.2 DATA PROCESSING

2.2.1 CALIBRATION OF RADAR DATA

In order to predict performance of an imaging radar system, the designer must establish values of numerous radar parameters and calculate signal levels within the system. Many of these, such as transmitter power, antenna gain, signal compression ratios, and noise levels, can be determined within relatively small tolerance. However, target reflectivity at the radar's wavelength is a factor that exhibits large

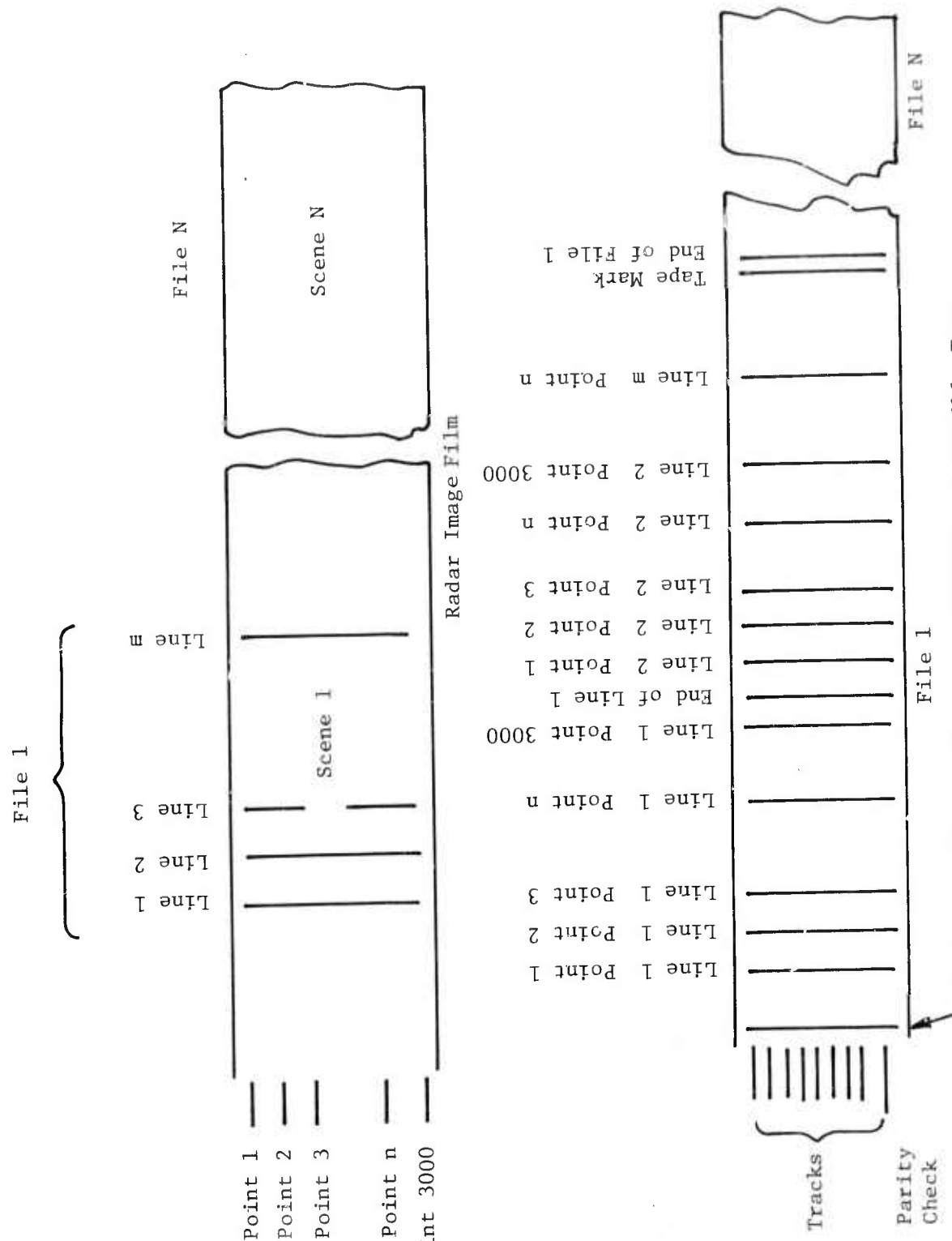


Figure 11. CCT Data Format

variation. Airborne radars used to image features of the earth's surface encounter a variety of reflectivities. Many objects reflect specularly at radar wavelengths. Some of these reflect away from the radar and produce weak echos in the radar, and some reflect toward the radar and produce very strong echo signals in the radar. There are reflecting surfaces that have high conductivity and reflect nearly all of the incident radar illumination and there are surfaces that absorb radiation.

In addition to the large dynamic range of radar echo signals, there is uncertainty due to limited measured values. The radar cross section (RCS) of simple objects can be calculated from the size and geometry of the object, the radar wavelength, and illumination angle [2]. Of course, when the reflecting object becomes more complex, the mathematical model increases in complexity. Expressions for RCS require knowledge of surface roughness, incident angle, complex dielectric constant, wavelength, and polarization. It has been found useful to consult experimentally derived listings for various target types [3,4].

Although there is no built-in calibration in this radar system, calibration of the data was attempted by including objects of known RCS within the imagery. All of the radar imagery obtained in Labrador utilized only two altitudes with their corresponding two antenna depression angles. An array of corner reflectors was installed at Goosebay Airport and imagery of the array was obtained at each of the two depression angles. A radar image of the Goosebay corner reflector array is shown in Figure 12. This array was constructed to provide calibration points in the imagery. The size and orientation of these five corners is known and their expected reflecting areas can be calculated. The reflectors were all the same size, but the illumination angles differed enough to provide considerable variation of effective radar cross section. The values are shown in Table 1.

The absolute value of the numbers comprising a digitized image is a function of digitizing parameters such as laser power, amplifier

2. G. T. Ruck, "Radar Cross Section Handbook," Plenum Press, 1970.
3. R. L. Cosgriff, W. H. Peake, R. C. Taylor, "Terrain Scattering Properties for Sensor System Design," Engineering Experiment Station Bulletin 181, Ohio State University, 1960.
4. Maurice W. Long, "Radar Reflectivity of Land and Sea," D. C. Heath and Company.

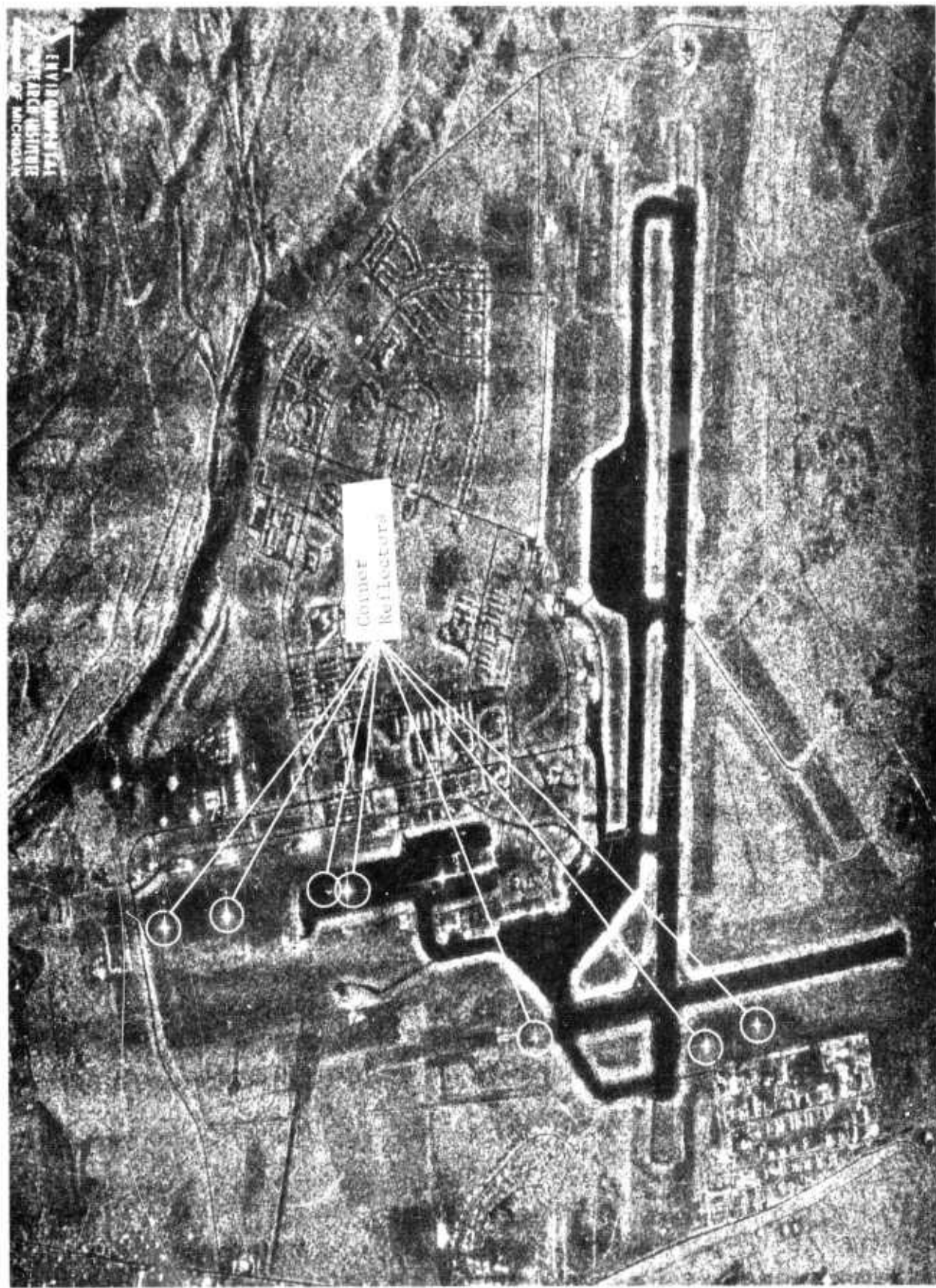


Figure 12. Radar Image of Corner Reflectors at Goosebay Airport.

Table 1. L-Band Radar Cross Section of Corner Reflector at Goosebay

<u>Corner</u>	<u>Depression Angle</u>	<u>Radar Cross Section</u>
A	44.06°	1845 - 6.4 dB = 423 sq. ft.
B	41.88°	1845 - 6.8 dB = 385 sq. ft.
C	30.12°	1845 - 1.8 dB = 1219 sq. ft.
D	27.46°	1845 - 6.2 dB = 443 sq. ft
E	26.36°	1845 - 6.2 dB = 443 sq. ft.

gain, photo multiplier tube calibration, and integration time. Most of the digitizing parameters were held constant for all of the digitized data. However, the laser power and the integration time were changed to accomodate high intensity images in the city and in the corner reflector array at Goosebay Airport. The recorded numbers were normalized to a laser power of 500 milliwatts and an integration time of 900 microseconds.

It is desirable to calibrate these recorded digital numbers in terms of radar cross-section or target reflectivity. Images of reflectors of equal radar cross section should vary across the image swath due to a number of factors. These factors include:

1. antenna gain variation with depression angle,
2. echo signal attenuation with range,
3. image compression ratio variation with range, and
4. diffraction efficiency variation across the signal film.

The magnitudes of these factors have been measured and calibration curves can be drawn. Table 2 lists these factors at several points across the image swath. These values were calculated for the altitude, antenna depression angle, and range used by the ERIM radar on February 23, 1977, in Pass 5.

A relative calibration curve using the values of Table 2 is shown in Figure 13. This curve indicates that there is about 14 dB of image intensity variation across the parallel polarized L-band imagery due to known radar characteristics. The downward slope at smaller depression angles is due to the signal reduction with range which has not been compensated for by antenna gain variation. Signal reflection from portions of the aircraft (multipath radiation) may also contribute to this signal variation. Diffraction efficiency values were obtained by interpolation from measured values.

This relative calibration data in conjunction with the reflecting area values (Table 1) were used to compute the intensity values of Table 3. The measured values of image intensity obtained from the digitized data were also added to Table 3, and the differences between the calculated and the measured relative values shown.

Table 2. Calculated Intensity Variation

<u>Location</u>	<u>Depression</u>	<u>Ant. Gain</u>	<u>Attenuation & Comp.</u>	<u>Diffraction</u>	<u>Total</u>
Near Edge	90°	6. dB	+5.5 dB	-3 dB	+ 8.5 dB
Nadir	90°	6. dB	+4.73 dB	-3 dB	+ 7.73 dB
.14 Range	63.77°	6.2 dB	+2.52 dB	-2.74 dB	+ 5.98 dB
Corner A	44.06°	12.6 dB	0 dB	-0.16 dB	+12.44 dB
Corner B	41.88°	13.2 dB	-0.53 dB	-0.14 dB	+12.53 dB
Corner C	30.12°	12.6 dB	-1.42 dB	-0.54 dB	+10.64 dB
Corner D	27.46°	9.2 dB	-1.78 dB	-0.36 dB	+ 7.06
Corner E	26.36°	8.6 dB	-1.95 dB	-0.19 dB	+ 6.46
.81 Range	25.05°	8.4 dB	-6.46 dB	0 dB	+ 1.94
Far Edge	21.78°	7.2 dB	-8.19 dB	0 dB	- 0.99

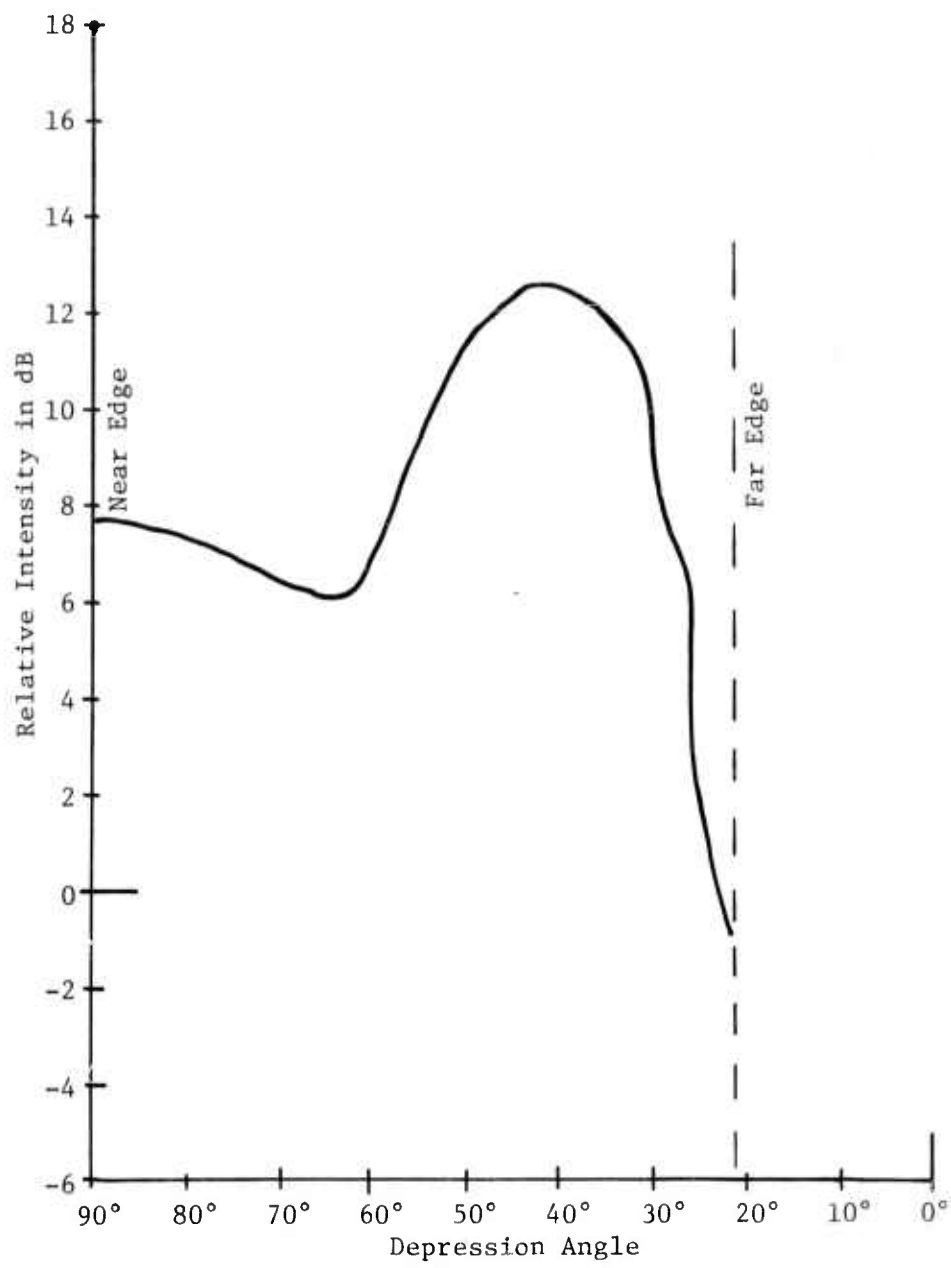


Figure 13. Relative Calibration Curve

Table 3. Computed and Measured Intensity Values

<u>Corner</u>	<u>Comp. Int.</u>	<u>Meas. Int.</u>	<u>Meas.-Comp.</u>
A	6.04 dB	0 dB	-6.04 dB
B	5.73 dB	+7.33 dB	+1.61 dB
C	8.84 dB	+9.14 dB	+0.30 dB
D	.86 dB	+6.07 dB	+5.21 dB
E	.26 dB	+2.23 dB	+1.97 dB

If the reflectivities of the corner reflectors were as calculated and the relative calibration curve was correct, the differences between the calculated and measured values should have been zero. There was a difference, however, and this difference was assumed to be due to reduced reflecting area of individual corner reflectors. The effective area of a corner reflector can only be decreased from the theoretical value due to mechanical deficiencies. With this practical consideration in mind, one can use corner D, which has the greatest positive difference, as a reference by assuming its area is correct, and then scale the other corner reflectors with respect to D as shown in Table 4.

This scaling appears reasonable although the 11.25 dB reduction for A is rather large. This corner reflector was probably damaged or misaligned. If corner D is truly exhibiting its calculated radar cross section of 443 sq. ft., an absolute calibration curve could be derived from the relative calibration curve by labeling it 443 sq. ft. The computer print-out numbers can be associated with this curve by placing the corner D computer print-out number, 179, on the corner D spot at 27.46° depression angle as indicated in Figure 14. A scale of numbers proportional to the square root of intensity has been inserted at the right of Figure 14. These numbers are also stored on the digital tape. Curves for radar cross-sections of 1,000 sq. ft., 100 sq. ft., and 10 sq. ft., have been added to Figure 14.

These curves can be used to determine the radar cross section of any cell in the radar image. Interpolation is facilitated by the logarithmic scale.

The information of Figure 14 has been rearranged in Figure 15 to make the computer intensity numbers easy to read. Interpolation in this figure requires use of a square root relationship between numbers and image intensity.

For working with radar imagery of extended target surfaces rather than point reflectors, it has been found helpful to consider target reflectivity rather than target cross section. Reflectivity is intended to represent a target characteristic without dependence

Table 4. Apparent Reduction in RCS of
Corner Reflectors

<u>Corner</u>	<u>Reduction</u>
A	-11.25 dB
B	- 3.60 dB
C	- 4.91 dB
D	0 dB
E	- 3.24 dB

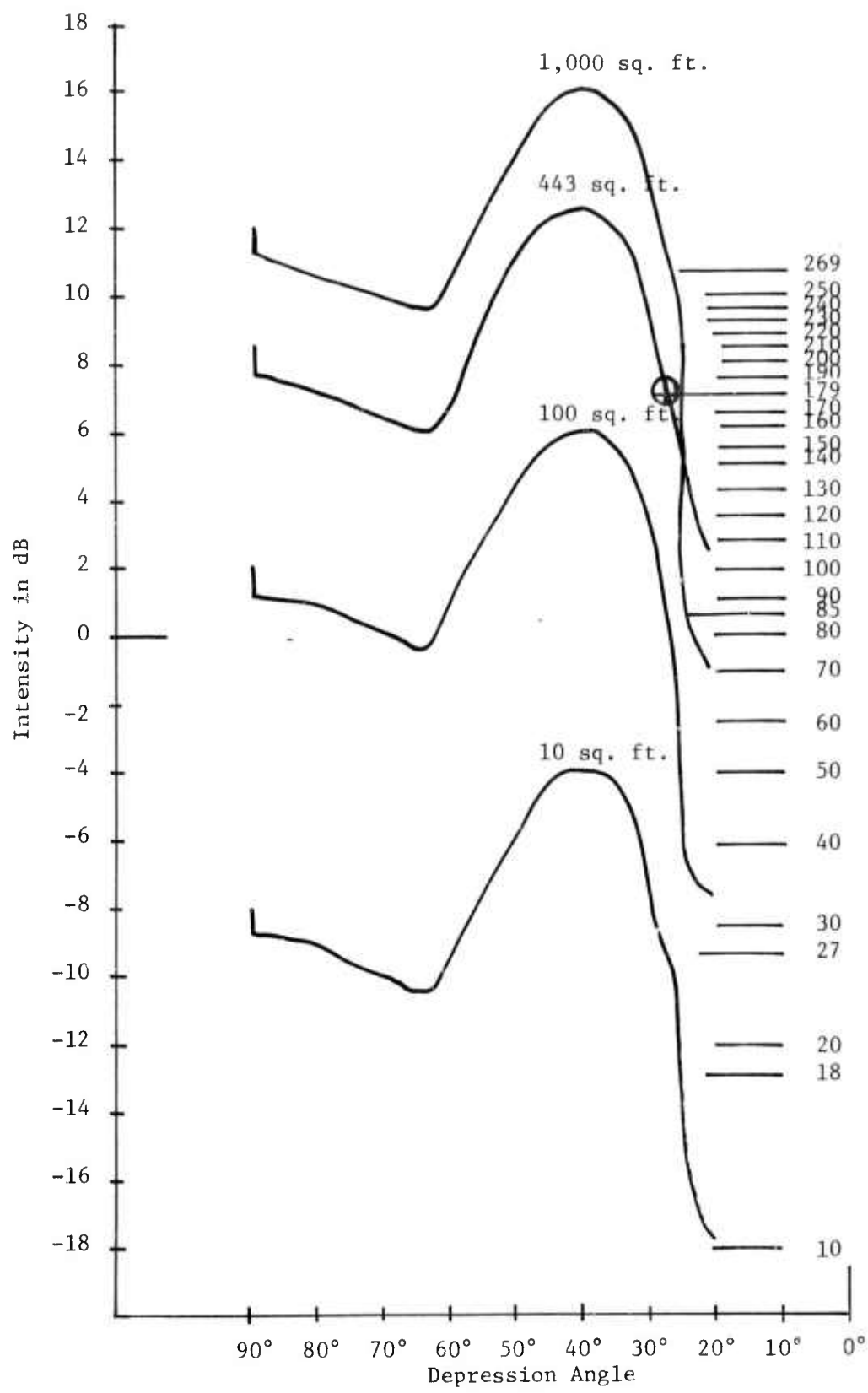


Figure 14. Intensity Vs. Depression Angle

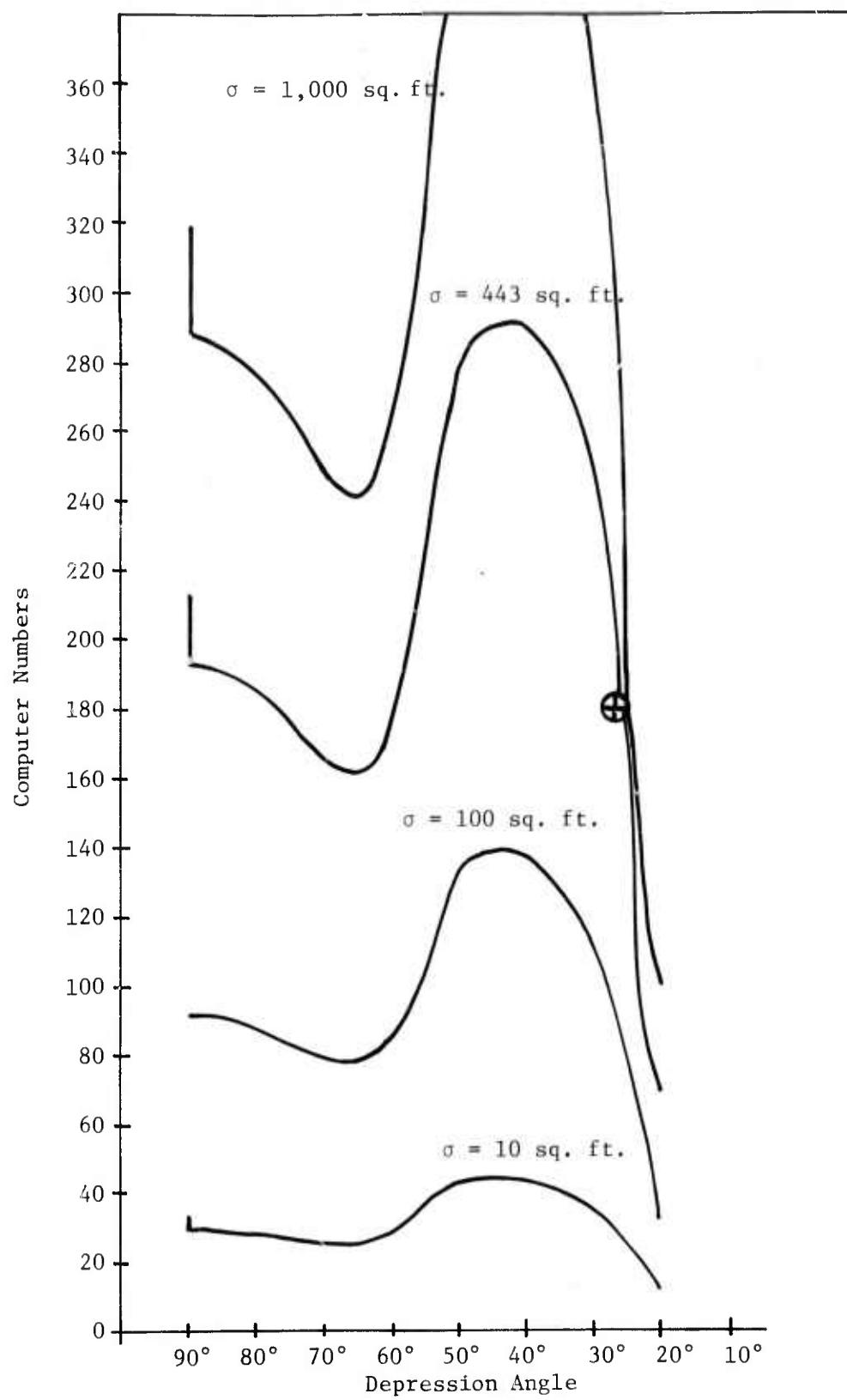


Figure 15. Computer Numbers Vs. Depression Angle

upon radar parameters. Reflectivity is defined as the ratio of radar cross section to target intercept area [3]:

$$\gamma = \frac{\sigma}{A_i} \quad (1)$$

Specular reflectors are observed to have reflectivities much greater than 1.0 while absorbing surfaces may have reflectivities much less than 1.0.

Extensive horizontal surfaces within the radar's imaged swath produce images that extend over many resolution cells. In studying imagery of cropland, snow covered areas, or ice packs, reflectivity of each resolution cell is of interest. The reflectivity of horizontal surfaces can be expressed as:

$$\gamma = \frac{\sigma}{P_R P_{CR} \tan \theta} \quad (2)$$

where P_R is range resolution

P_{CR} is cross range resolution, and

θ is depression angle.

The depression angle used in this expression is the angle between the radar line-of-sight and the local terrain surface. Terrain that slopes toward the radar has an effective depression angle larger than terrain which is level or horizontal. The radar cross section of a resolved patch of level terrain grows smaller as the depression angle grows smaller because the intercepted area of the incident radiation is smaller. Many of these surfaces have been found, however, to have reflectivity, γ , nearly independent of depression angle. In these cases a single γ value characterizes the surface of nearly any depression angle. This horizontal surface relationship does not hold at steep depression angles where the radar resolution cell is larger than the surface intercepted by the radar beam.

The constant σ curves of Figures 14 and 15 could be changed to constant γ curves by the relationship:

$$\sigma = \gamma P_R P_{CR} \tan \theta \quad (3)$$

In the digitized imagery of Goosebay Air Force Base P_R is 3 m and P_{CR} is 4.5 m. The value of γ and its accompanying computer number N has been calculated and entered in Table 5. Computer numbers associated with adjacent constant γ values have been calculated and included in Table 5.

Figure 16 is a plot of computer numbers for constant horizontal surface reflectivity over a range of depression angles. This figure can be used to find a reflectivity value for any resolution cell of the radar image from the digital numbers.

Another relationship used with imagery of horizontal surfaces is reflectivity per resolution cell projected onto the horizontal plane. This is:

$$\sigma_o = \frac{\sigma}{P_R P_{CR}} \cos \theta \quad (4)$$

Values of σ_o are a function of local depression angle and are meaningless without identification of the depression angle to which they apply.

Numbers associated with constant σ_o values were calculated and entered into Table 6. These values were plotted in Figure 17 which shows intensity numbers over a range of depression angles for three constant σ_o values.

The information of Figure 17 was rearranged to show the square root relationship of intensity numbers with projected reflectivity values at a selection of depression angles. This is shown in Figure 6.

Table 5. Values of γ and Computer Numbers

Dep. σ	Angle	80°				70°				60°				50°				40°				30°				20°			
		N	γ	N	γ	N	γ	N	γ	N	γ	N	γ	N	γ	N	γ	N	γ	N	γ	N	γ	N	γ				
1,000 sq. ft.	275	6.20	240	6.50	270	3.975	410	5.77	510	8.20	340	11.92	100	18.91															
	251	1.0	152	1.0	135	1.0	170	1.0	178	1.0	98	1.0	23	1.0															
100 sq. ft.	87	.188	76	.2505	83	.3975	134	.577	160	.820	108	1.192	32	1.391															
	79	.1	48	.1	41.6	.1	50	.1	31	.1	31	.1	7	.1															
10 sq. ft.	27.5	.012	24	.02505	27	.0397	41	.0577	51	.0820	34	.01	10	.1891															
	25.1	.01	15.2	.01	13.6	.01	17.1	.01	17.8	.01	9.8	.01	2.3	.01															

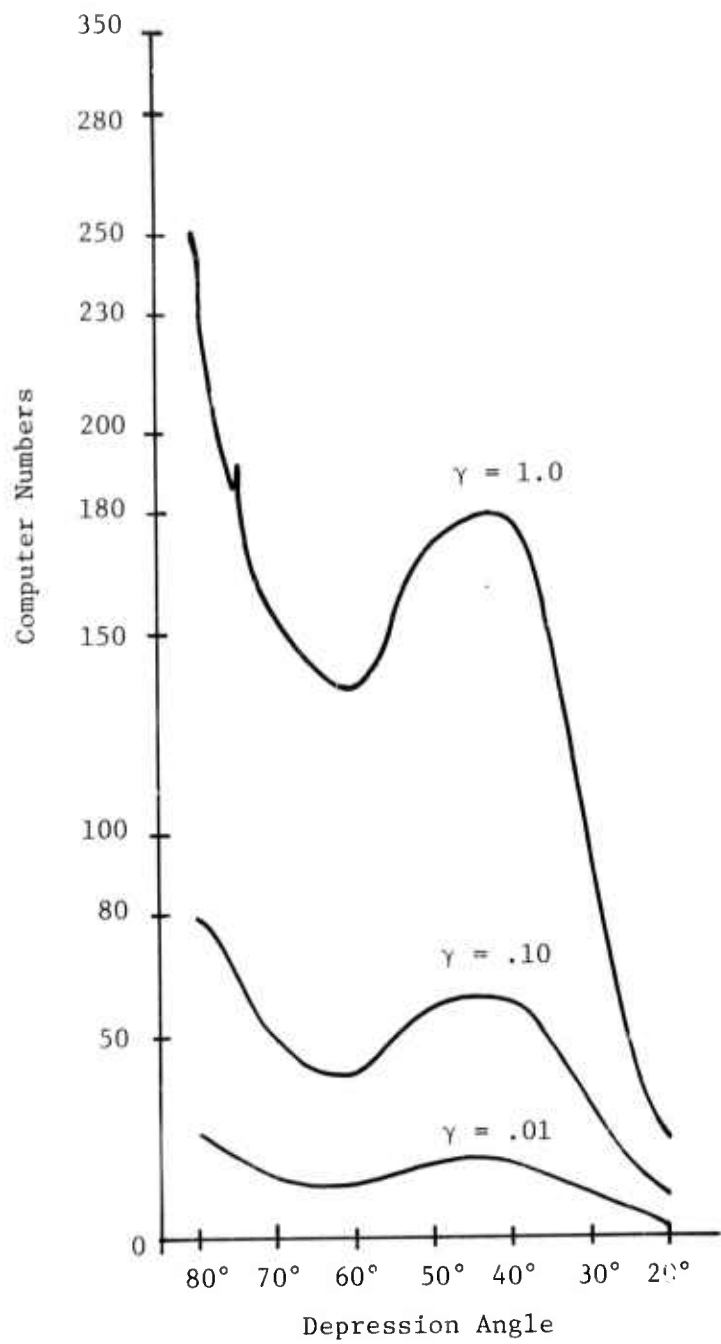


Figure 16. Plot of Computer Numbers Vs. Depression Angle for Constant γ

Table 6. Relation of Computer Numbers to σ_o Values

Dep. Ang	80°			70°			60°			50°			40°			30°			20°		
	σ_o	N	σ_o	N	σ_o	N	σ_o	N	σ_o	N											
$\gamma = 1$.9848	251	.9397	157	0.866	145	.766	194	.6428	222	.5000	139	.3420	39.3							
	1.000	252.92	1.000	161.96	1.000	155.81	1.0	221.65	1.0	276.90	1.000	196.58	1.0	67.20							
$\gamma = .1$.09848	79	.09397	49.5	.0866	44.7	.0766	54.0	.06428	69.8	.050	43.8	.03420	12.6							
	.1	79.61	.1	51.00	.1	48.03	.1	61.70	.1	87.06	.1	61.94	.1	21.54							
$\gamma = .01$.009848	25.1	.009397	15.7	.00866	14.6	.00766	19.5	.006428	22.2	.0050	13.9	.003420	3.9							
	.01	26.29	.01	16.20	.01	15.69	.01	22.28	.01	27.69	.01	19.66	.01	6.67							

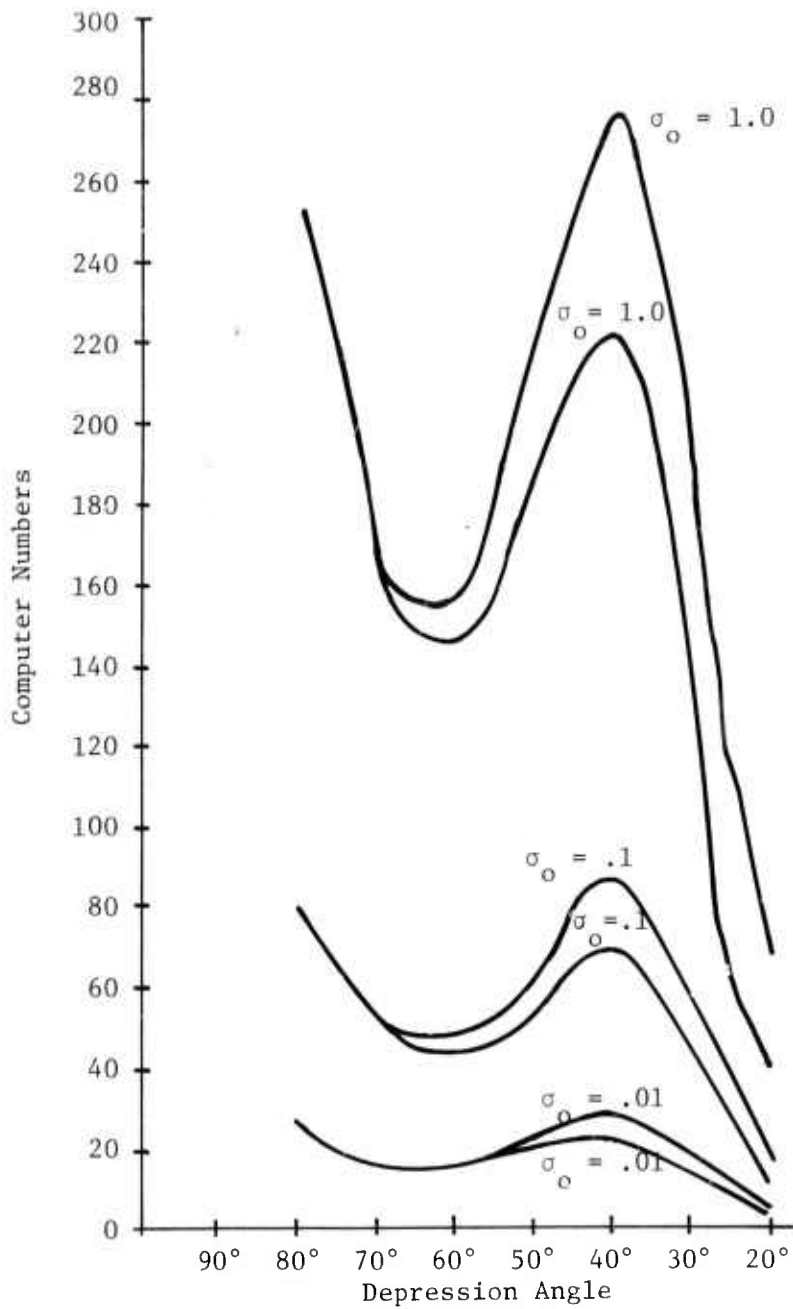


Figure 17. Plot of Computer Numbers Vs. Depression Angle for Constant σ_0

Figure 18 represents the radar cross section per unit ground area, σ_0 , as a function of the computer numbers. Curves are drawn for the three angles used in the clutter distribution statistics. Because the bright corner reflectors would saturate the image dissector the laser power had to be attenuated from 500 m watts to 50 m watts. This normalization is reflected in Table 7 where normalizing factors for the digital tapes are given.

To convert the computer numbers to σ_0 values you find the number on the vertical axis of Figure 18 and draw a straight line across until you intersect the curve of the proper depression angle and read the value for σ_0 off of the X-axis. This curve is normalized to 500 milliwatts laser power and an integration time of 900 microseconds.

2.2.2 CLUTTER DISTRIBUTION SOFTWARE DOCUMENTATION

This section describes the interactive Fortran IV program which generates relative frequency and cumulative distributions from digitized radar data. This program also tests these frequency distributions against three theoretical distributions, namely, the normal, log-normal, and gamma functions for goodness of fit. Appendix II lists the main program and associated subroutines.

The basic block of data used by the distribution program contains an ASC II header, which identifies the data, followed by the actual binary data. Each data point is a number proportional to the square root of a radar intensity return the size of one pixel. Each data block is a rectangular patch of points containing typically 256 pixels in range and 4660 pixels in azimuth. These blocks, therefore, usually contain well over a million points. In order to economize on data storage, each point is first divided by 16 and then written on computer compatible tape (CCT) in 8 bit, unsigned binary.

The distribution program is basically an averaging and distribution plotting tool with provisions for chi-squared testing. Figure 19 shows the program flow which may be divided into four major parts:

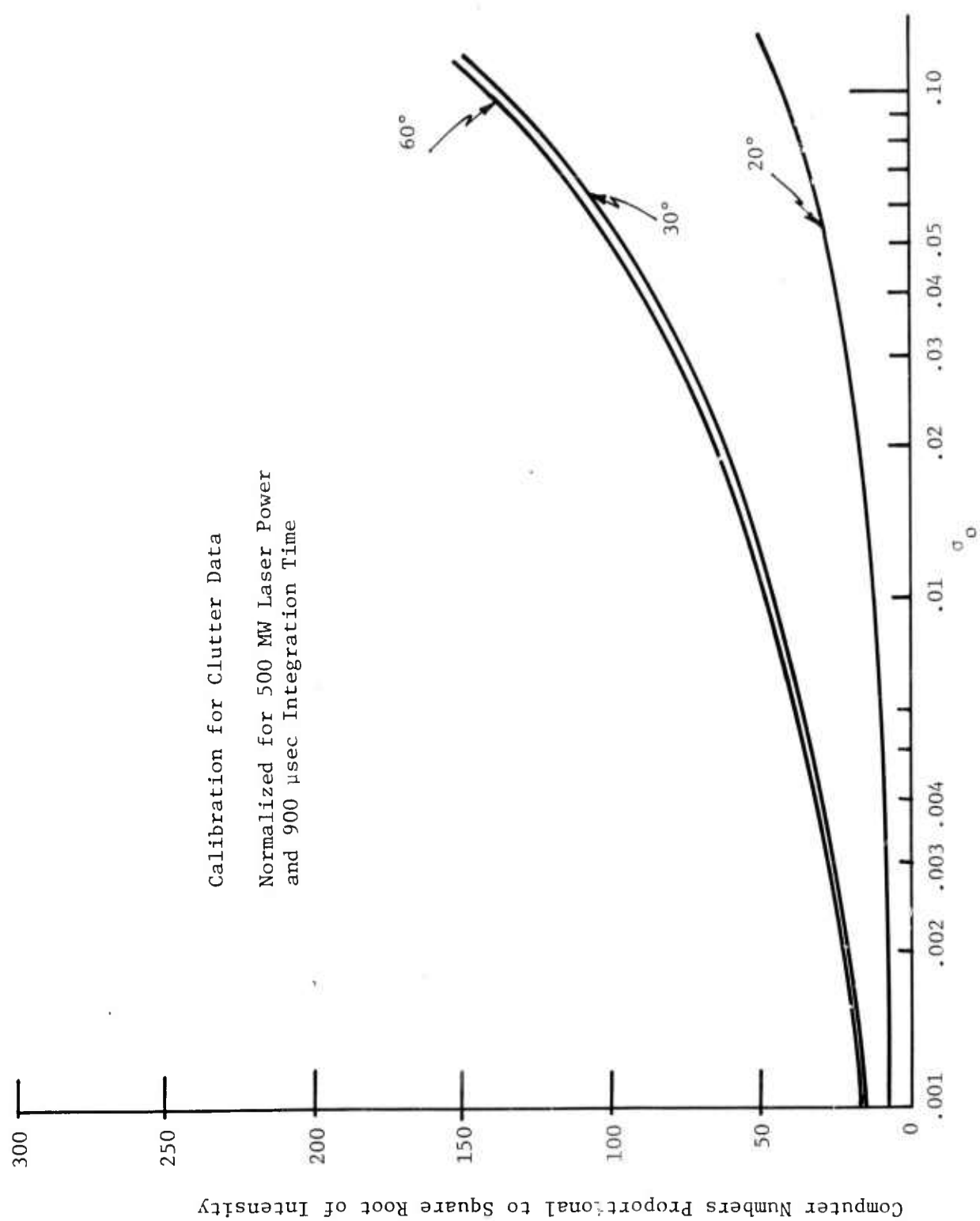


Figure 18. Plot of Computer Numbers Vs. σ_0

Table 7. Normalization Factors For All
IPL Tapes

<u>IPL Tape Number</u>	<u>Normalizing Factor</u>
407	1.0
408	1.0
409	1.0
410	1.0
411	1.0
412	1.0
431A	4.74
432	1.1

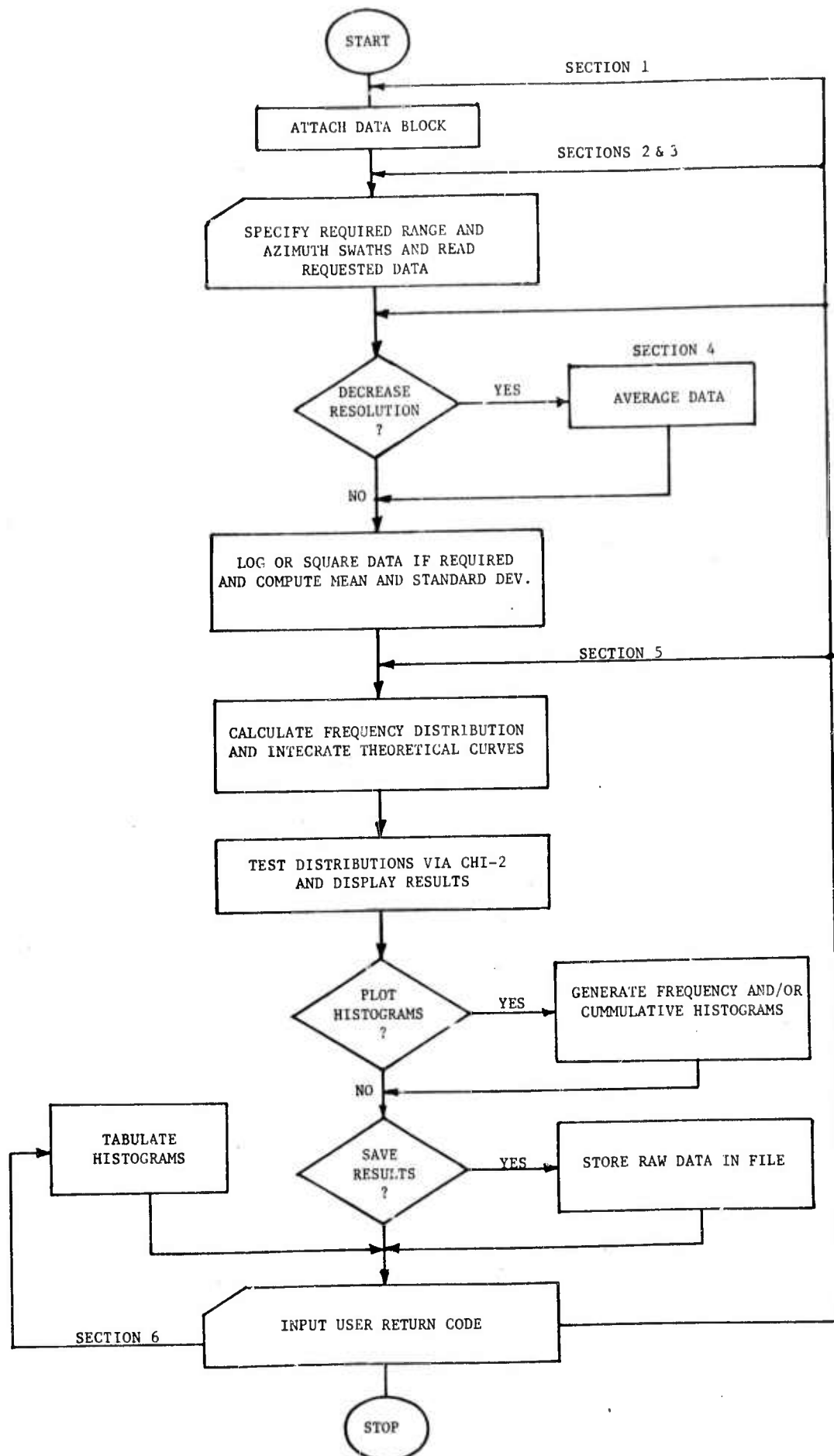


Figure 19. Computer Program Flow Chart

1. The proper data is selected.
2. Any required averaging or preprocessing is performed.
3. The frequency distribution is calculated and tested against three theoretical curves for goodness of fit.
4. The results may be plotted or saved for external post-processing.

The first major portion of the program includes sections 1, 2, and 3 of the program listing (Appendix II). Initially, the user is prompted to enter the location of the data. The program will echo the header associated with the data and then ask the user to verify that the proper data has been selected. The data, however, is not read at this time. The user must first indicate whether the raw data is to be squared or converted to decibels. Also, a subset of the entire data block must be defined before actual processing can begin since a data block may contain more than a million points, but the program can only handle a quarter million at a time. The subblock of data is specified by entering azimuth and range swaths. It is then that the program will actually read the specified data into memory. Although the data is physically stored in a one-dimensional array, it is organized in two dimensions, range and azimuth.

The next major portion of the program is identified as Section 4 in the program listing. In this section the user will be prompted to enter averaging intervals. If none are entered, no averaging will be performed. If intervals are supplied, the total number of points in each averaging cycle will be the product of the range and azimuth intervals. This has the effect of decreasing resolution in proportion to the interval size. For example, if the resolution of an area 10 pixels in azimuth and 10 pixels in range were to be halved, square data groups of 4 pixels each would be averaged together. This averaging would reduce the original 10 by 10 matrix to a 5 x 5 matrix. Note that the azimuth and range intervals are independent of each other.

After the data has been averaged (averaging one pixel square sections of the data is equivalent to no averaging), it may be squared

or converted to decibels if requested by the user. The data will then be reorganized into a one-dimensional array for the remainder of the program.

The third major portion of the program, identified as the first half of Section 5, will actually compute the frequency distribution of the data and compare it with theoretical distributions. Also computed in this section are the mean and standard deviation of the data. These computations are performed in double precision to ensure no loss of accuracy in the standard deviation calculation. After these statistics have been displayed, the user is prompted to enter the minimum and maximum values of the data to be included in the distribution along with the number of intervals to be used. The user may also optionally specify scales for plots and whether points lying outside the min-max of the distribution should be considered equivalent to the min-max values. After all the user input is accepted, the program will calculate the actual frequency distribution.

Once the raw data distribution has been calculated, theoretical distributions are computed given the mean and standard deviation of the raw data. If no decibel conversions were performed on the raw data, three theoretical curves will be computed. These are the normal, log-normal and gamma distributions. If decibel conversions were performed, only the normal distribution will be computed. These distributions are computed by integrating the area under the respective theoretical curves. Due to the integration technique, sections of curves with very steep slopes may produce small negative areas. This can superimpose small oscillations on the cumulative plots. After all the theoretical distributions have been computed, they are compared for goodness of fit with the raw data distributions using the chi-square technique. The max chi-square value, which is displayed with the chi-square results, is only an approximate figure if the degrees of freedom are over 30. All the distributions may be optionally normalized at this point.

The last major portion of the program, sections 5 and 6, will display the results of the previous computations. The user may request a histogram of the frequency and/or cumulative distribution of all the data plotted simultaneously. Optionally, a tabular listing of the results may be requested. Finally, the raw data for this run may be saved in a file to be processed by other programs, such as, an autocorrelation program.

The user is then given the opportunity to go back to any section of the program for continued processing after the cost of the run just completed has been displayed.

The program documented in this section is a powerful, cost-effective tool for statistical analysis of radar imagery. It will process up to a quarter million radar return samples interactively with the user. The histograms produced by the program are both flexible and easy to read. Finally, and perhaps most important, the user of the program is able to return again and again to any section of the program to modify or repeat any portion of his analysis.

STATISTICS FOR TERRAIN CLUTTER

During the flight of 2/24/77 over the Labrador Sea area, the FIM dual frequency, dual polarization synthetic aperture radar measured clutter return from several different kinds of terrain and/or ice surfaces. This section makes an abbreviated statistical examination, at the L-band frequency for HH polarization only, of data recorded for refrozen lead and pack ice, black ice, mountainous terrain (both with and without lakes), and tundra. Data recorded for several fields and a city on a separate flight are also included for comparison purposes.

This section defines the statistics used to examine these data (section 3.1); it also presents and discusses those distributions which are leading candidates to characterize, on the basis of the chi-square test, the data histograms (section 3.2).

Section 3.3 contains histograms of data for the various clutter types: pack ice and refrozen lead, black ice, mountainous terrain, tundra, fields, and a city (Toronto). In addition, the effect on the data histograms of averaging over various sized boxes of data (or equivalently, of increasing the resolution cell size) is examined. And finally, in section 3.4, the correlation results are presented.

3.1 STANDARD STATISTICS AND CORRELATION

The mean

$$\mu = \frac{1}{n} \sum_{i=1}^n n_i \quad (5)$$

and standard deviation

$$\sigma = \left(\frac{\sum_{i=1}^n n_i^2 - \frac{1}{n} \left(\sum_{i=1}^n n_i \right)^2}{n - 1} \right)^{1/2} \quad (6)$$

are computed from the digitized data n_i for each sample n of data to be examined. In addition, histograms for these data are also determined in the form of frequency of occurrence of n_i vs. n_i , or frequency of occurrence of the n_i in a prescribed interval vs. that interval. No higher order statistics of the data are computed, since all distributions chosen as candidates to characterize the histograms are completely specified by mean and standard deviation alone.

To study the effects of resolution size on the nature of the histograms, the data are averaged for a clutter patch size determined by certain azimuth and range intervals. The results are then used to form histograms as indicated above.

Finally, the correlation coefficient $\rho(k)$ has also been determined for various clutter types. The correlation coefficient is defined as

$$\rho(k) = \frac{1}{n \sigma^2} \sum_{i=1}^n (n_{i+k} - \mu)(n_i - \mu) \quad (7)$$

where n , n_i , μ , and σ are as defined above, and $i + k \equiv i$ (modulo n). This latter device has two effects: (1) it lines up columns of range numbers in a single line; and (2) it folds the last k of the range numbers back on the first k of the range numbers. The results could be slightly misleading when the terrain corresponding to the last range column is vastly different from the first. This consideration does not arise here, however, since n is always taken to be very much larger than k ; thus, any slight tendency toward misleading information is vastly outweighed by the programming simplicity required for the above definition of ρ .

3.2 FITTING DATA WITH STANDARD FREQUENCY DISTRIBUTIONS

This section examines the question of characterizing the various types of clutter data by means of well-known distributions. Three distributions have been examined in some detail in connection with each type of clutter data. They are the normal, log normal [5], and gamma; each is defined and discussed in further detail in section 3.2.1 below. These distributions were chosen for examination because each has appeared in connection with some type of train or sea clutter characterization (the Rayleigh distribution is a special case of the gamma distribution). There are, of course, other distributions which have appeared in connection with clutter studies but for which time limitation has permitted no study in relation to the present data. They are enumerated in section 3.2.2.

Any of the distributions to be mentioned in this discussion can be modified somewhat by introducing a "component" with a standard deviation which differs from the standard deviation of the original distribution. The result is called a "contaminated distribution." Although the term appears in the literature [6] with reference only to normal distributions, there is no reason why the concept cannot be extended to other distributions, and, in particular, to the log-normal and gamma distributions. This extension is made in section 3.2.3 for the gamma distribution and the resulting improvement of fit over an ordinary gamma distribution is illustrated and discussed for mountainous terrain data.

5. Only about 100 years old. See J. Aitchison and J. A. C. Brown, *The Log-Normal Distribution*, Cambridge Univ. Press, 1957.
6. The author is uncertain of the origins of this terminology but has found it in connection with "contaminated normal clutter" in G. V. Trunk and S. F. George, "Detection of Targets in Non-Gaussian Sea Clutter," *IEEE Trans. AES*, Vol. AES-6, pp. 620-628, Sept. 1970.

The term "improvement" is used in connection with the chi-squared test. Time has not permitted the examination of any other test, although there are several which might be appropriate. A discussion of the question of testing the fit of known distributions to the clutter data is given in section 3.2.4.

3.2.1 NORMAL, LOG-NORMAL, AND GAMMA DISTRIBUTIONS

In the present work the normal and log-normal distributions are used in essentially equivalent senses. The data are digitized so that a numerical value describing a given pixel of clutter is proportional to field strength, or square root of power. Thus, if one wishes to determine whether returned power is distributed log-normally, there are two choices of procedure. On the one hand, the digital data may be modified by applying $20 \log^*$ to each number. The modified data are then tested against a normal distribution whose mean $\mu_{20 \lg}$ and standard deviation $\sigma_{20 \lg}$ are found from the $20 \log$ data. Figure 20 shows the normal curve

$$N(x) = \frac{A}{\sqrt{2\pi} \sigma_{20 \lg}} e^{-(x-\mu_{20 \lg})^2/2\sigma_{20 \lg}^2} \quad (8)$$

superposed on a histogram of pack ice data; A is the area under the histogram. Figure 21 is an alternative presentation of the same data on probability paper. The staircase represents cumulative frequency; the straight line is a cumulative distribution corresponding to Eq. (8).

On the other hand, a log-normal distribution may be tested against the unmodified data by taking $20 \log x$ to be the independent variable of the log-normal distribution. The resulting log-normal

* The choice of $20 \log$, both here and with the log-normal distribution below, has been made so as to deal with data expressed in dB relative to some power level.

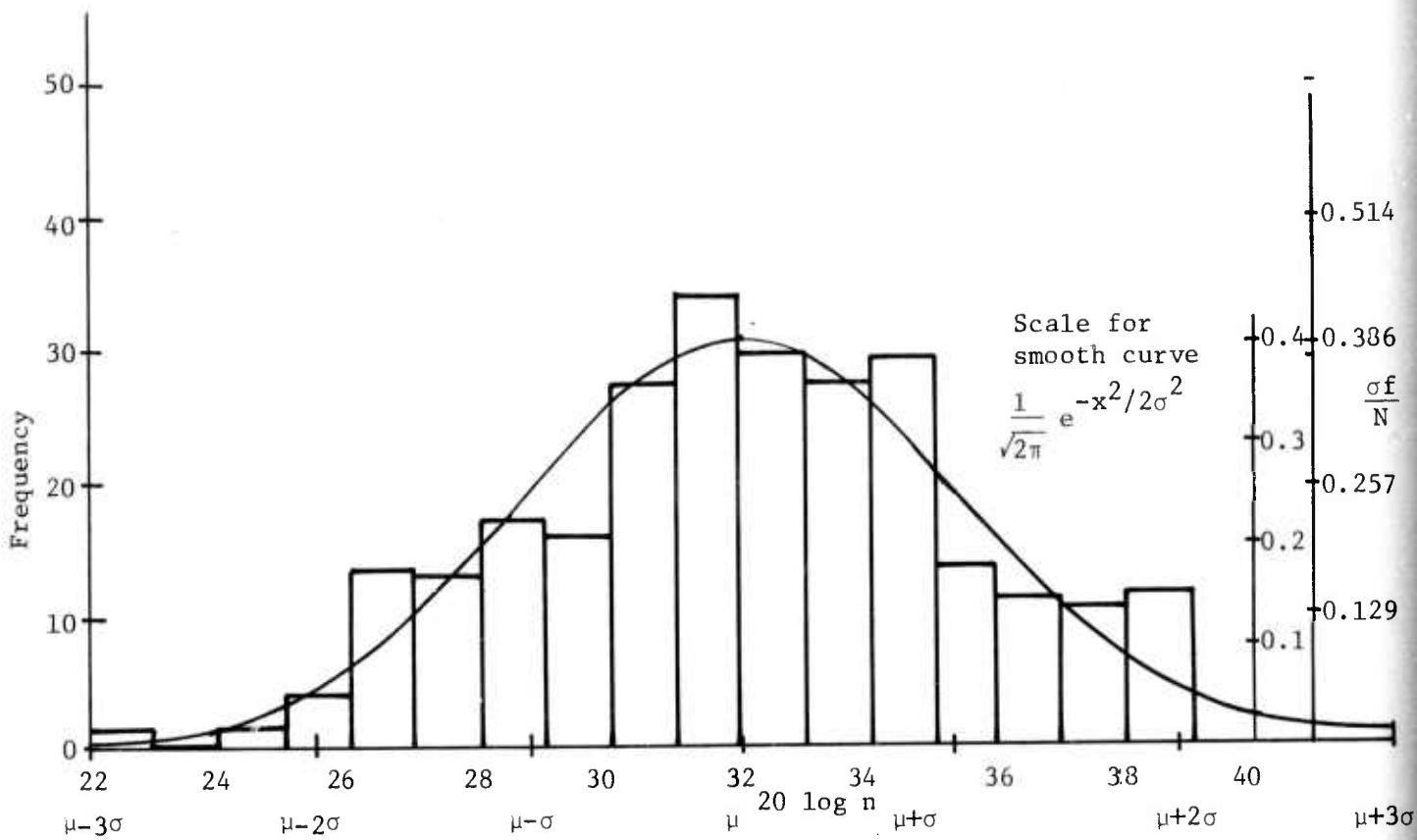


Figure 20. Histogram and Normal Density Fit for Pack Ice
(IPL 407, File 1, Pass 2, L-Band)

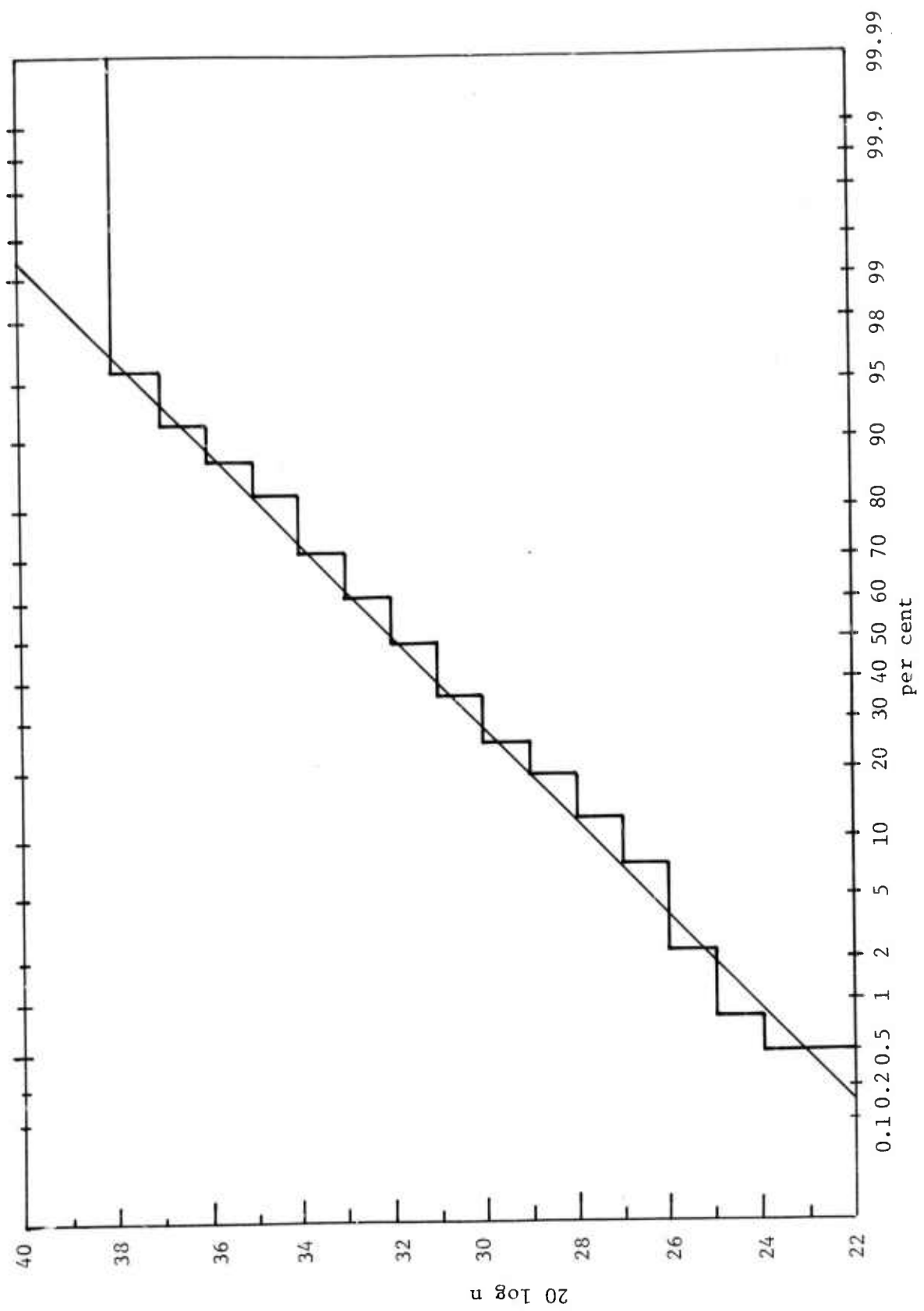


Figure 21. Cumulative Distribution for Pack Ice

curve*

$$L(x) = \frac{\frac{20}{\ln 10} A}{\sigma_{20 \lg} x \sqrt{2\pi}} e^{-[20 \lg x - \mu_{20 \lg}]^2 / 2\sigma_{20 \lg}^2}, \quad x > 0 \quad (9)$$

is shown in Figure 22 superposed on a histogram for the same pack ice data used for Figure 20; and Figure 23 shows the same information on log-probability paper. The quantities $\mu_{20 \lg}$, $\sigma_{20 \lg}$, and A have the same meanings as above; \ln denotes the natural logarithm (in contrast to \log which, of course, denotes the common logarithm). Thus, Figures 20, 21, and 22 are equivalent representations for the same information; the log-normal representation, together with others, is chosen for comparison with the data distributions to be examined in section 3.3 below.

In many studies a Rayleigh distribution has been used to fit certain data. That distribution is included here under the more general gamma distribution

$$g_{\alpha, \nu}(x) = \frac{A}{\Gamma(\nu)} \alpha^{\nu} x^{\nu-1} e^{-\alpha x}, \quad \alpha, \nu > 0, \quad x \geq 0 \quad (10)$$

The mean, variance, and mode of this distribution are, respectively,

$$\mu = \frac{\nu}{\alpha}, \quad \sigma^2 = \frac{\nu}{\alpha^2}, \quad \text{and} \quad x_m = \frac{\nu-1}{\alpha} \quad (11)$$

and the maximum value of the gamma frequency distribution at the mode is

* For this and subsequent distributions which are defined only for $x > 0$, it is always to be understood that the distribution is defined to be 0 for $x \leq 0$.

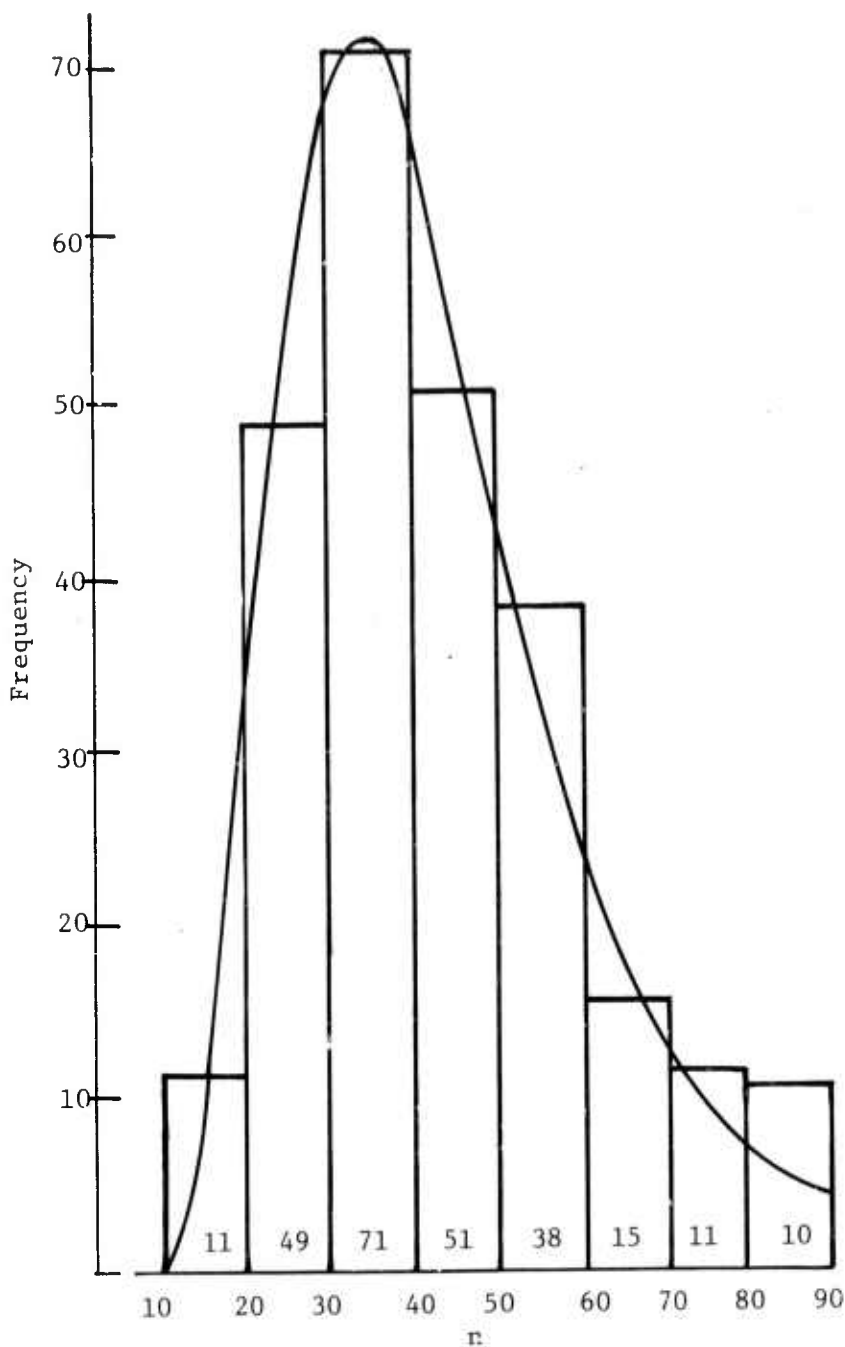


Figure 22. Histogram and Fitting Log-Normal Distribution
for Pack Ice
(IPL 407, File 1, Pass 2, L-Band)

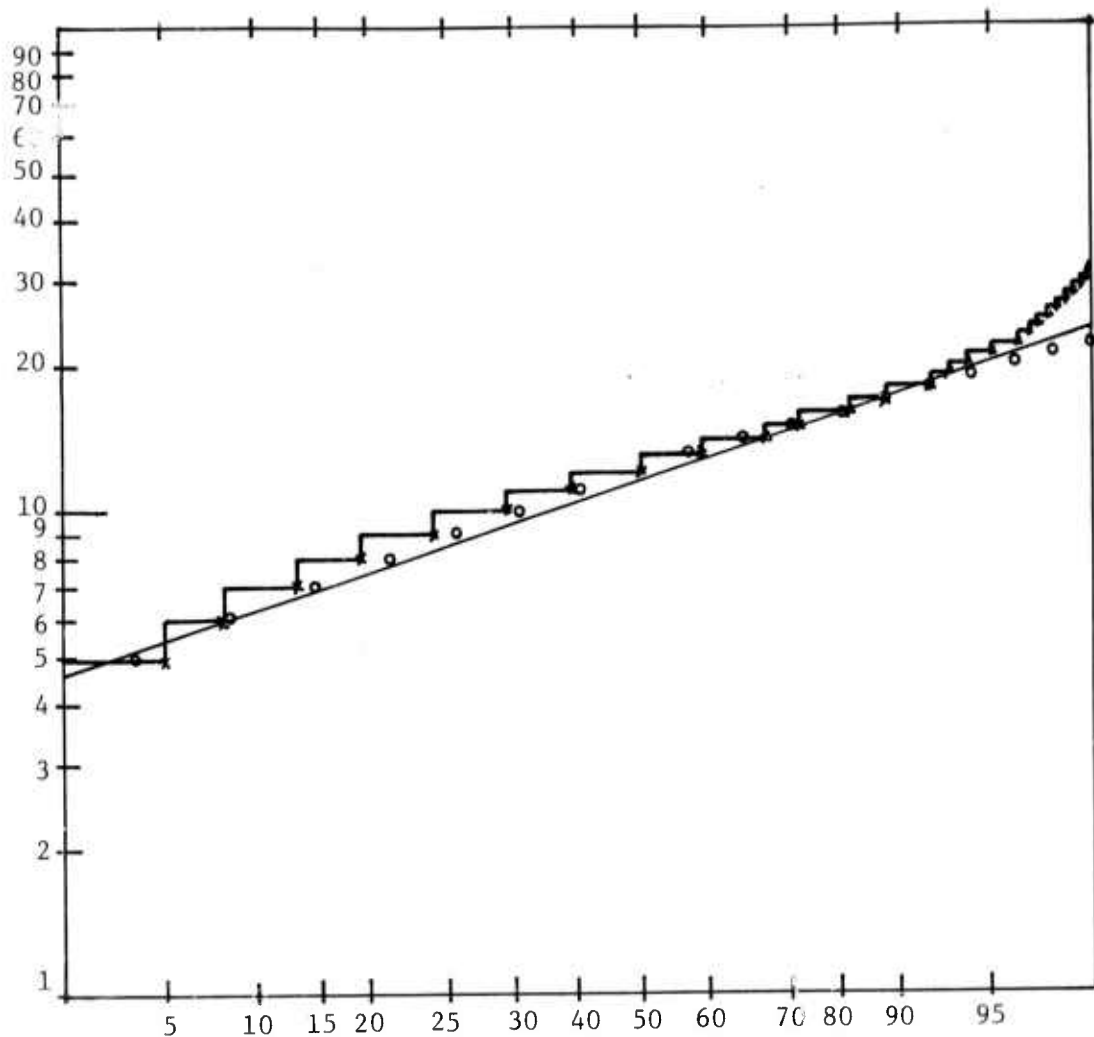


Figure 23. Mountainous Terrain (x) with Log-Normal Fit (-)
 Pass 4, $\Sigma f = 766$, $\mu_{201g} = 20.97$, $\sigma_{201g} = 3.34$ ($^{\circ}$ gamma)

$$g_{\alpha, \nu}(x_m) = \frac{\alpha A}{\Gamma(\nu)} (\nu - 1)^{\nu-1} e^{-(\nu-1)} \quad (12)$$

The parameters α and ν can be expressed in terms of two of the three quantities μ, σ and/or x_m . The first two have been chosen for the present purposes: Thus,

$$\alpha = \frac{\mu^2}{\sigma^2}, \quad \nu = \frac{\mu^2}{\sigma^2} \quad (13)$$

and so Eq. (3) can be rewritten as

$$g_{\mu, \sigma} = \frac{A}{\Gamma\left(\frac{\mu^2}{\sigma^2}\right)} \left(\frac{\mu}{\sigma^2}\right)^{\mu^2/\sigma^2} x^{\left(\frac{\mu^2}{\sigma^2}\right)-1} e^{-x\mu/\sigma^2} \quad (14)$$

Now it is easy to see that if $\nu = 1$, the gamma density (14) becomes a Rayleigh density, with $\mu = \sigma$:

$$g_{1/\sigma, 1}(x) = \frac{A}{\sigma} e^{-x/\sigma}, \quad x \geq 0 \quad (15)$$

The log-normal distribution (8) and the gamma distribution (14) together with the standard normal distribution are used in section 3.3 below to compare with histograms of various types of Labrador Sea data.

3.2.2 OTHER DISTRIBUTIONS

There are still other distributions which have been used with success by some researchers to describe certain clutter situations. Although time has not permitted their application in this work, they should certainly not be excluded from any further study.

The main distributions which should be mentioned are the Beckmann [7], the Rice, and the Hoyt distributions. Briefly, these may be defined as follows. Let rectangular variables x, y and polar variables r, ψ be related as usual and let x and y be normally distributed with mean values α and β and variances s_1 and s_2 , respectively. Then the distribution for r , which has been called the Beckmann distribution, is

$$B(r) = \frac{r}{\sqrt{s_1 s_2}} \exp \left[-\frac{\alpha^2}{2s_1} - \frac{(s_1 + s_2)r^2}{4s_1 s_2} \right] \sum_{m=0}^{\infty} (-1)^m E_m I_m \left(\frac{s_2 - s_1}{4s_1 s_2} r^2 \right) I_{2m} \left(\frac{\alpha r}{s_1} \right) \quad (16)$$

where $E_m = \begin{cases} 1, & m = 0 \\ 2, & m \neq 0 \end{cases}$, and I_m is the modified Bessel function.

If $\alpha = 0$ and $s_1 = s_2 = n/2$ ($I_m(0) = \begin{cases} 1, & m = 0 \\ 0, & m \neq 0 \end{cases}$), then Eq. (16) reduces to the Rayleigh distribution [compare (15) with $x = r^2$]

$$B(r) = \frac{2r}{n} e^{-(r^2/n)} \quad (17)$$

If $\alpha = c$ (a constant), and $s_1 = s_2 = n/2$, then Eq. (16) becomes the Rice distribution

$$R(r) = \frac{2}{n} r e^{-(r^2+c^2/n)} I_0 \frac{2cr}{n} \quad (18)$$

7. P. Beckmann, A. Spizzichino, "The Scattering of Electromagnetic Waves from Rough Surfaces," MacMillan Company, New York, 1963.

Beckmann calls this the distribution of a constant vector \bar{c} (along the x-axis) + a Rayleigh vector. Goldstein [8] has made successful application of this distribution to terrain data.

Finally, if $\alpha = 0$ and $s_1 \neq s_2$, the result is the Hoyt distribution

$$H(1) = \frac{r}{\sqrt{s_1 s_2}} \exp \left[-\frac{(s_1 + s_2)r^2}{4s_1 s_2} \right] I_0 \left(\frac{s_2 - s_1}{4s_1 s_2} r^2 \right) \quad (19)$$

Note then that both the Rice and Hoyt distributions are special cases of the Beckmann distribution.

3.2.3 CONTAMINATED DISTRIBUTIONS

In their study of sea clutter, Trunk and George [6], employ a "contaminated normal" distribution with success. There is, of course, no reason why the same contamination process cannot be applied to any of the above distributions. It has, in fact, been applied with promising results, at least for a relatively small sample (766 points) of mountainous terrain data, as the following discussion will show.

A "contaminated gamma" distribution can be created from Eq. (14) by writing

$$G_{K,\gamma}(x) = \gamma \frac{A}{\Gamma\left(\frac{\mu^2}{K^2\sigma^2}\right)} \left(\frac{\mu}{K^2\sigma^2}\right)^{\mu^2/K^2\sigma^2} x^{(\mu^2/K^2\sigma^2)-1} e^{-(x\mu/K^2\sigma^2)}$$

$$+ (1 - \gamma) \frac{A}{\Gamma\left(\frac{\mu^2}{\sigma^2}\right)} \left(\frac{\mu}{\sigma^2}\right)^{\mu^2/\sigma^2} x^{(\mu^2/\sigma^2)-1} e^{-(x\mu/\sigma^2)},$$

$$x \geq 0, 0 \leq \gamma \leq 1 \quad (20)$$

8. D. E. Kerr, "The Propagation of Short Radio Waves," MIT Rad. Lab. Series #13, McGraw-Hill, 1951.

The second term is the gamma distribution (14) (mean μ , st. dev. σ) reduced by the factor $(1 - \gamma)$ (which lies between 0 and 1). To this is added the first term which is also a gamma distribution with unchanged mean μ but standard deviation modified by the factor K ; the result is then reduced by the factor γ . If $0 < K < 1$, the peak of the gamma distribution is squeezed upward, while its sides and tail are squeezed inward and downward. If $K > 1$, the reverse occurs.

Figures 24, 25, and 26 show contaminated gamma distributions superposed on a histogram of 766 points representing mountainous terrain. In Figure 24 the gamma distribution is uncontaminated; that is, $K = 1$ (or $\gamma = 0$). The result is marginally acceptable as a fit. Actually, the chi-square test yields a statistic of $\chi^2 = 41.98$; the test statistic, at the 95% confidence level and 25° of freedom is $\chi^2_{95}(25) = 37.65$. Thus, according to the chi-square test, the gamma distribution is not an acceptable fit of the histogram.

Figure 25 shows a contaminated gamma distribution with $K = 0.7$ and $\gamma = 3/4$ superposed on the histogram. The "eye-ball test" suggests that the fit is better. But in actual fact it is worse according to the chi-square test, since it produces a statistic of $\chi^2 = 56.43$.

Figure 26 shows a contaminated gamma distribution with $K = 1.2$, $\gamma = 1/4$ superposed on the histogram. The "eye-ball test" suggests that the fit is worse. But the chi-square test indicates not only an improvement in fit but also that the fit is chi-square acceptable, since it yields a statistic of $\chi^2 = 35.49$.

The choice of the gamma distribution to illustrate the contamination process was a purely arbitrary one. If a more extensive study indicates that some other distribution is a more likely description of ice clutter data, then the contamination process should be applied to that distribution to obtain more precise data fits. It appears, from the brief examination of the application of the process to the gamma distribution, that the contamination parameters K and γ could be chosen so as to improve the distribution fit to certain parts of the histogram,

in particular, say at the tails. Thus, it should be possible to design a computer program in which the contamination parameters K and γ would be chosen so as to optimize some statistical test, such as the chi-square test.

The idea of the contaminated distribution is appealing because it suggests a possible explanation for the clutter scattering; that two (or more) types of scatterers are causing two (or more) essentially different deviations about some mean scattering return.

3.2.4 STATISTICAL TESTS

For the present work, only one test (other than the somewhat inexact but nevertheless intuitively helpful "eyeball test") has been used to determine goodness-of-fit of certain distributions to data histograms. It is the old standby, the chi-square test. A description of the test can be found in almost any statistics book, but it is useful to define the test conditions used here.

Let f_i be the frequency of occurrence of data numbers in the i th of N bins; and let F_i be the value of the distribution being tested at the center of the i th bin. The chi-square statistic χ^2 is then given by

$$\chi^2 = \sum_{i=1}^N \frac{(f_i - F_i)^2}{F_i} \quad (21)$$

The test hypothesis H is that the data sample is from the distribution F , i.e., as $N \rightarrow \infty$, the data sample distribution will approach the distribution described by the function F . The test statistic used for the present work is $\chi^2_{95}(df)$, where df denotes the degrees of freedom ($= N-3$ in the present situation since the total of frequencies, the mean, and the standard deviations of the data sample are known) of the chi-square distribution. If $\chi^2 < \chi^2_{95}(df)$, the data are to be regarded as consistent with H , with a 5% chance of error. If $\chi^2 > \chi^2_{95}(df)$, then

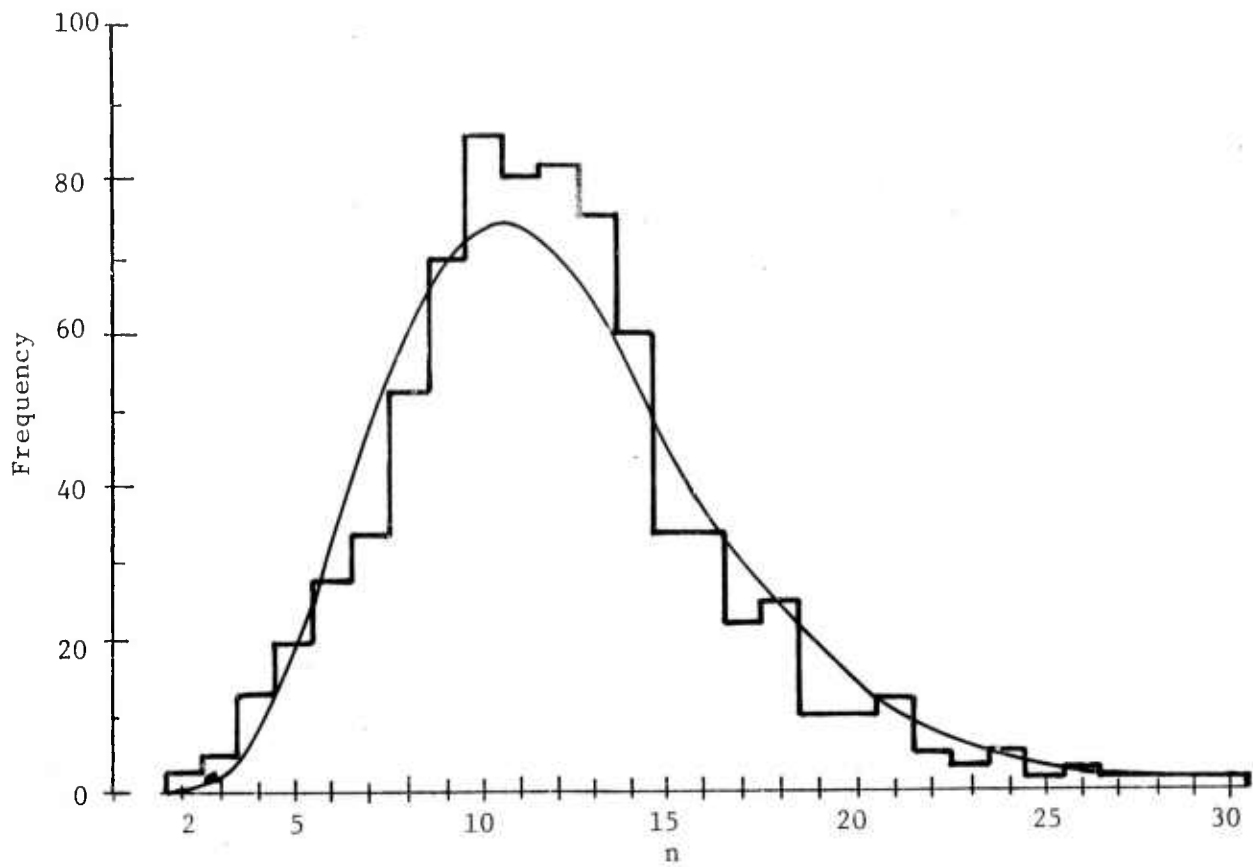


Figure 24. Histogram for Bare Mountain Data and Gamma Density Fit

$$\chi^2(25) = 37.65$$

$$\chi^2 = 41.98$$

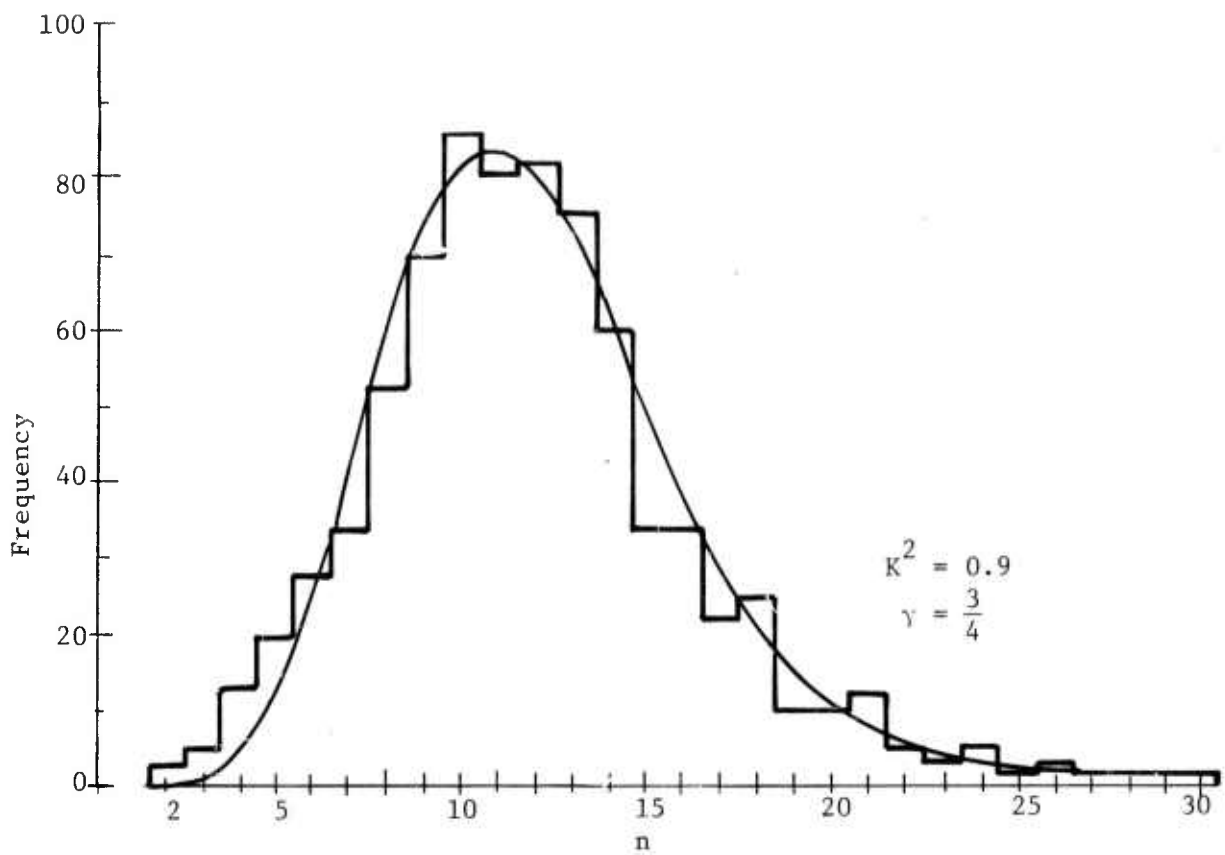


Figure 25. Histogram for Bare Mountain Data and Contaminated Gamma Density Fit

$$\chi^2_{95}(25) = 37.65$$

$$\chi^2 = 56.43$$

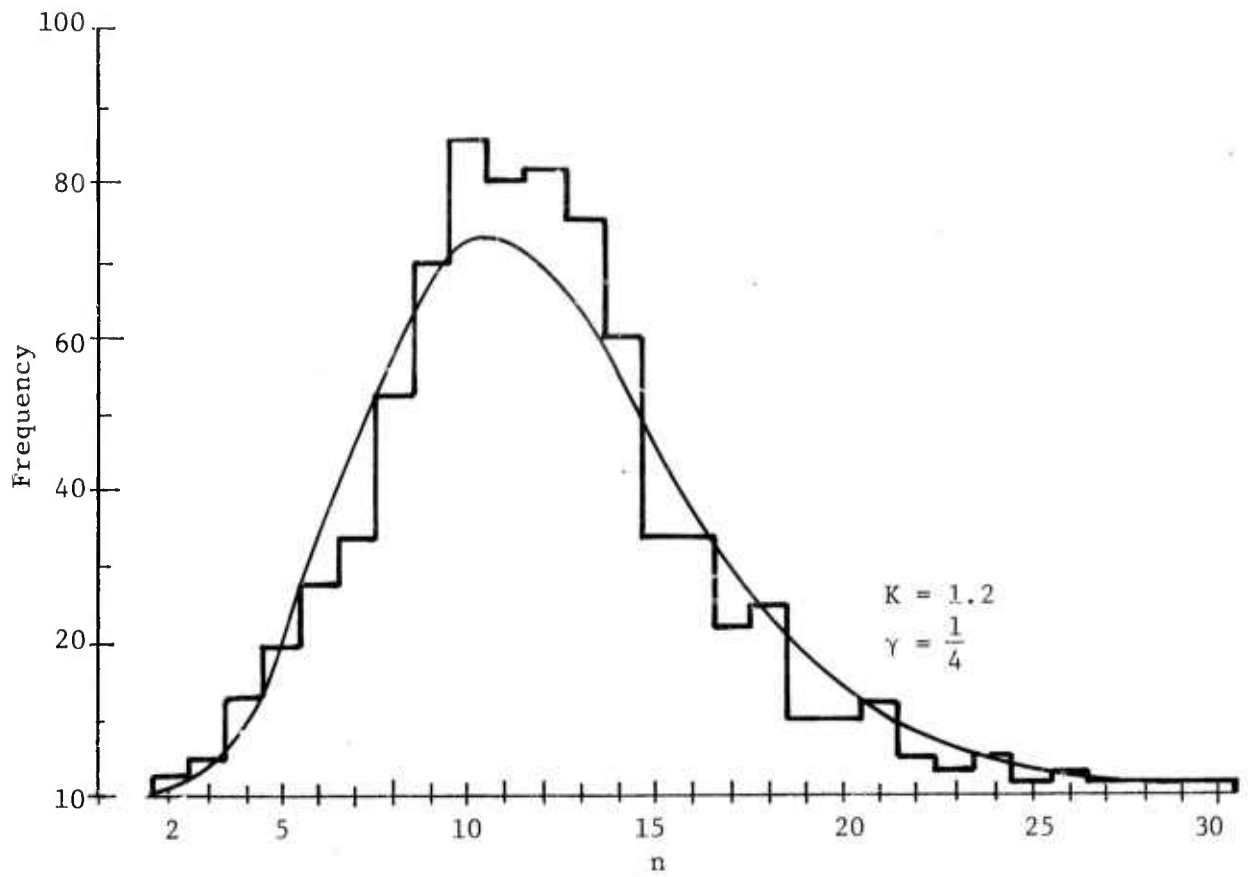


Figure 26. Histogram for Bare Mountain Data and Contaminated Gamma Density Fit

$$\chi^2_{95}(25) = 37.65$$

$$\chi^2 = 35.49$$

H is to be regarded as false (or else a somewhat rare event has occurred).

Because of the form of Eq. (21), the chi-square test places especially strong emphasis on the tails of the distribution. This fact is clearly illustrated by the data and tested distributions presented in Figures 23, 24, and 25 above. The chi-square test has been chosen as a criterion to be studied in the present program because the data at the tails of the histograms are particularly important (potential false alarm sources). However, there are other tests which may be equally good or better and which may not offend the "eyeball test" as flagrantly as the chi-square test does in Figure 25. Other test candidates include the Komolgoroff-Smirnov, the Snedecor, and the Runs tests.

3.3 DISTRIBUTIONS FOR VARIOUS TERRAIN CLUTTER TYPES AT VARIOUS RESOLUTION SIZES

This section contains a discussion of the statistical description of data for the various clutter types: pack ice; bare mountain; a city; three fields; black ice; and tundra. The vast amount of material resulting from the statistical analysis is collected in Appendix I. For each of the clutter types the following parametric and statistical information is recorded (Appendix I):

1. a definition of azimuth and range swaths (also displayed as a rectangular "box"),
2. the resulting numbers of points considered;
3. the azimuth and range averaging intervals (i.e., resolution interval size; 1,1 indicates no averaging), together with a normalizing option for the data histogram;
4. the minimum, maximum, mean, standard deviation, and histogram for that data set;
5. superposed on each histogram, the normal (:) log-normal (0), and gamma (x) distributions, each

with mean and standard deviation equal to the data mean and standard deviation (each of these distributions is uniquely determined by specifying its mean and standard deviation); and, finally,

6. The chi-square test statistic, at the 95% confidence level, for the appropriate degrees of freedom (also included) and the chi-square statistics for the normal, log-normal, and gamma distributions.

A complete description of the program and its workings is given as Appendix II.

All of the data sets to which the computer program has been applied are listed in Table 8, together with the figure number under which each appears in Appendix I. Given with each data set described in Table 8, are the critical parameters, the statistics, and the calibration information for that set; these include the depression angle, azimuth and range swaths, number of points, resolution size (i.e., averaging interval size), mean, standard deviation, the chi-square test statistic, and the chi-square statistics for the normal, log-normal, and gamma fitting distributions. In addition, the calibration information is used to convert mean and standard deviation into σ_0 values, i.e., RCS per unit illuminated area. Thus, Table 8 can be used not only as a key to the available data given in Appendix I but also as a comprehensive summary of available results.

The data figures are arranged according to the patterns shown in Tables 9a and 9b. The arrangement is built on a basic data set which is comprised of four items, each at three elevation angles for the four terrain types: a total of 48 in the basic set. The four items treated are: a large sample with no averaging; the original sample with averaging over squares 10 pixels on a side; the original sample with averaging over squares 25 pixels on a side; and the original sample with averaging over squares 50 pixels on a side. In addition, there is, for the mountain, ice, city and field terrains, a supplementary

Table 8. Data Inventory

FIGURE NUMBER	TERRAIN TYPE	DEPRESSION ANGLE	AZ SWATH	RANGE SWATH	NO. PTS.	AVGINC	μ	σ	STATISTICS		
									$\chi^2_{95}(\text{dt})$	$\chi^2(N)$	$\chi^2(L)$
1	MOUNTAIN	20	1-811	1-308	234318	1x1	9.59	5.03	38(25)	22940	4146*
2	MOUNTAIN	20	1-811	1-308	2542	10x10	8.92	4.47	20(11)	137*	356
3	MOUNTAIN	20	1-811	1-308	429	25x25	8.57	4.45	14(7)	47*	76
4	MOUNTAIN	20	1-811	1-308	119	50x50	8.01	4.51	13(6)	17.3	21
5	MOUNTAIN	30	3301-4276	1-256	248814	1x1	14.24	5.93	34(22)	14564	3520*
6	MOUNTAIN	30	3301-4276	1-256	2548	10x10	14.11	4.32	21(12)	181	47
7	MOUNTAIN	30	3301-4276	1-256	449	25x25	13.88	4.09	16(8)	36	19.1
8	MOUNTAIN	30	3301-4276	1-256	70	50x50	13.46	3.93	13(6)	12	7.9**
9	MOUNTAIN	60	1-5000	1-50	25000	1x1	32.09	13.92	52(37)	41332	11639
10	MOUNTAIN	60	1-5000	1-50	2500	10x10	32.09	9.04	52(37)	424*	948
11	MOUNTAIN	60	1-5000	1-50	400	25x25	32.09	7.40	39(26)	373*	657
12	MOUNTAIN	60	1-5000	1-50	100	50x50	32.09	6.11	25(15)	72	27*
13	PACK ICE	20	1-811	1-308	249788	1x1	12.38	4.92	33(21)	24723	6226*
14	PACK ICE	20	1-811	1-308	2542	10x10	12.28	3.03	16(8)	82*	431
15	PACK ICE	20	1-811	1-308	429	25x25	12.23	2.77	13(6)	46*	115
16	PACK ICE	20	1-811	1-308	119	50x50	12.18	2.64	11(5)	27*	47
17	PACK ICE	30	3685-4660	1-256	249856	1x1	38.12	14.77	52(37)	23076	1351*
18	PACK ICE	30	3685-4660	1-256	248	10x10	33.01	9.47	35(23)	225*	404
19	PACK ICE	30	3685-4660	1-256	440	25x25	37.70	8.33	25(15)	107*	155
20	PACK ICE	30	3685-4660	1-256	120	50x50	37.12	7.97	22(13)	38*	51
21	PACK ICE	60	1-4659	1-50	232950	1x1	36.09	13.42	52(37)	30231	1359*
22	PACK ICE	60	1-4659	1-50	2330	10x10	36.09	6.14	31(20)	501	41*
23	PACK ICE	60	1-4659	1-50	374	25x25	36.08	3.16	20(11)	218*	10265
24	PACK ICE	60	1-4659	1-50	94	50x50	36.06	1.97	8(3)	1.22	1.23
25	CITY	20	1-811	2193-2500	248384	1x1	5.64	4.76	21(12)	29660*	
26	CITY	20	1-811	2193-2500	2542	10x10	5.61	3.36	40(27)		43
27	CITY	20	1-811	2193-2500	429	25x25	5.64	2.72	21(12)	363	127
28	CITY	20	1-811	2193-2500	119	50x50	5.68	2.37	14(7)	94.14	889
29	CITY	30	1-976	1687-1943	250232	1x1	8.82	7.34	28(17)	12269*	82489

*BEST
**BEST, AND ACCEPTABLE BY CHI-SQUARE TEST

Table 8. Data Inventory (Continued)

FIGURE NUMBER	TERAIN TYPE	DEPRESSION ANGLE	AZ SWATH	RANGE SWATH	NO. PTS.	AVGING	μ	σ	χ^2_{95} (df)	χ^2_{95} (N)	χ^2 (L)	χ^2 (G)
30	CITY	30	1-976	1687-1943	2548	10x10	8.76	5.43	28(17)	36*	761	
31	CITY	30	1-976	1687-1943	440	25x25	8.57	3.94	21(12)	150*	170	
32	CITY	30	1-976	1687-1943	120	50x50	8.35	2.89	11(5)	58	24*	27
33	CITY	60	1-5000	1-50	250000	1x1	6.53	3.47	28(17)	12527*	39480	
34	CITY	60	1-5000	1-50	2500	10x10	6.50	2.40	20(11)	559*	6541	
35	CITY	60	1-5000	1-50	400	25x25	6.50	1.85	11(5)	40*	142	
36	CITY	60	1-5000	1-50	100	50x50	6.50	1.46	4(1)	2	1.37	1.06**
37	FIELD A	1-624	1-118	73632	1x1	34.39	11.47	52(37)	1500	303*	1371	
38	FIELD A	1-624	1-118	756	10x10	34.48	5.26	25(15)	173	22**	36	
39	FIELD A	1-624	1-118	125	25x25	34.39	2.94	14(7)	58	17*	22	
40	FIELD A	1-624	1-118	39	50x50	34.55	2.29	11(5)	20	18	17*	
41	FIELD B	1-536	1-198	106128	1x1	41.35	11.82	52(37)	9025	401*	920	
42	FIELD B	1-536	1-198	1080	10x10	41.36	4.91	25(15)	59	19**	23	
43	FIELD B	1-536	1-198	176	25x25	41.40	2.84	11(5)	5	3**	3	
44	FIELD B	1-536	1-198	44	50x50	41.37	2.14	6(2)	4	3**	3	
45	FIELD C	1-624	1-238	146512	1x1	45.92	16.48	52(37)	13209	644*	3005	
46	FIELD C	1-624	1-238	1512	10x10	45.89	8.84	39(26)	130	39**	54	
47	FIELD C	1-624	1-238	250	25x25	45.73	7.11	25(15)	34	25**	26	
48	FIELD C	1-624	1-238	65	50x50	45.61	6.22	18(10)	30	28*	28*	
49	MOUNTAIN	20	1-1	1-308	308	1x1	11.45	5.42	20(11)	29	28	16**
50	MOUNTAIN	20	1-10	1-308	3080	1x1	11.30	5.38	20(11)	103*	365	164
51	MOUNTAIN	20	1-50	1-308	15400	1x1	11.21	5.84	28(17)	3394	1672	423*
52	MOUNTAIN	20	1-100	1-308	10800	1x1	11.09	5.78	28(17)	5074	3069	716*
53	MOUNTAIN	30	3301-3301	1-2°	256	1x1	15.22	5.45	25(15)	62	20.1**	20.2
54	MOUNTAIN	30	3301-3310	1-256	2560	1x1	15.53	5.32	25(15)	389	82	65*
55	MOUNTAIN	30	3301-3350	1-256	12800	1x1	15.29	5.21	28(17)	1225	1025	188*
56	MOUNTAIN	30	3301-3400	1-256	25600	1x1	15.30	5.45	28(17)	2549	1571	322*
57	MOUNTAIN	30	3301-4276	1-256	6264	2x2	14.18	5.54	31(20)	47070	1871	305*
58	MOUNTAIN	30	3301-4276	1-256	15616	4x4	14.18	5.00	28(17)	3956	151	90*
59	MOUNTAIN	30	3301-4276	1-256	976	16x16	14.18	4.05	17(9)	62	44	37*
60	MOUNTAIN	30	3301-4276	1-56	244	32x32	14.20	3.85	14(7)	24	19	18*

Table 8. Data Inventory (Continued)

FIGURE NUMBER	TERAIN TYPE	DEPRESSION ANGLE	AZ STAT ^(c)	RANGE SWATH	NO. PTS.	AVGNG	μ	σ	$\chi^2_{95}(\text{df})$	$\chi^2(\text{N})$	$\chi^2(\text{L})$	$\chi^2(\text{G})$
61	MOUNTAIN	30	3301-4300	1-256	256000	1x1	14.30	5.98	35(23)	14703	3608*	
62	MOUNTAIN	30	3301-4300	1-256	64000	2x2	14.25	5.59	31(20)	44305	1837	332*
63	MOUNTAIN	30	3301-4300	1-256	16000	4x4	14.25	5.04	29(18)	4816	145	93*
64	MOUNTAIN	30	3301-4300	1-256	1008	16x16	14.27	4.10	17(9)	64	40	35*
65	MOUNTAIN	30	3301-4300	1-256	256	32x32	14.32	3.89	14(7)	23	14.7	14.6*
66	PACK ICE	30	4061-4660	1-256	153600	1x1	41.42	14.12	56(42)	22923	469*	2730
67	PACK ICE	30	4061-4660	1-256	1560	10x10	41.30	7.06	30(19)	21	36	17**
68	PACK ICE	30	4061-4660	1-256	72	50x50	40.23	5.38	16(8)	8*	10	9
69	PACK ICE	30	4061-4660	1-256	255	1x1	46.70	13.47	44(30)	36	29	27**
70	PACK ICE	30	4651-4660	1-256	2560	1x1	38.08	13.78	52(37)	316	47**	67
71	PACK ICE	30	4641-4660	1-256	5120	1x1	38.17	13.62	52(37)	466	70*	70*
72	PACK ICE	30	4641-4660	1-256	2560	1x1	42.34	13.26	52(37)	280	42**	61
73	PACK ICE	30	4641-4660	129-256	2560	1x1	34.01	12.66	52(37)	390	40**	68
74	PACK ICE	30	4611-4660	1-256	12800	1x1	38.88	14.17	52(37)	1340	75*	198
75	PACK ICE	30	4561-4660	1-256	25600	1x1	39.21	13.93	52(37)	2636	124*	391
76	PACK ICE	30	2801-2810 (4R LEAD)	1-256	2560	1x1	39.50	17.04	52(37)	501	74*	176
77	PACK ICE	30	2801-2900 (4R LEAD)	1-256	25600	1x1	36.67	13.86	52(37)	4040	205*	770
78	PACK ICE	30	4561-4660	1-3	300	1x1	41.89	12.41	52(37)	920	41**	60
79	PACK ICE	30	4561-4660	1-30	3000	1x1	46.32	14.51	52(37)	409	51**	93
80	PACK ICE	30	4061-4660 (HOMOG.)	1-256	153600	1x1	41.42	14.12	52(37)	1544	463*	2608
81	PACK ICE	30	4061-4660	1-256	38400	2x2	41.42	12.88	52(37)	5183	64*	641
82	PACK ICE	30	4061-4660 (HOMOG.)	1-256	9600	4x4	41.42	10.48	52(37)	2519	28**	97
83	PACK ICE	30	4061-4660	1-256	608	16x16	41.37	6.05	52(37)	44**	105	70
84	PACK ICE	30	4061-4660 (4R LEAD)	1-256	264	25x25	40.89	5.64	21(12)	8**	21	15
85	PACK ICE	30	4061-4660 (HOMOG.)	1-256	152	32x32	41.38	5.22	18(10)	11**	20	16
86	PACK ICE	30	3685-4660 (4R LEAD)	1-256	249856	1x1	38.12	14.77	52(37)	25076	1351*	2914
87	PACK ICE	30	3685-4660 (4R LEAD)	1-256	440	25x25	37.70	8.33	25(15)	107*	155	163

Table 8. Data Inventory (Continued)

FIGURE NUMBER	TERRAIN TYPE	DEPRESSION ANGLE	AZ SWATH	SWATH	RANGE	NO. PTS.	AVGINC	U	σ	$\chi^2_{95}(\text{df})$	$\chi^2(\text{N})$	$\chi^2(\text{L})$	$\chi^2(\text{G})$
88	MOUNTAIN	30	3685-4660	1-256	120	50x50	37.12	7.97	22(13)	38*	51	54	
89	CITY	30	1-1	1687-1943	257	1x1	6.63	2.21	9(4)	40	15*	17	
90	CITY	30	1-10	1687-1943	2570	1x1	6.68	2.36	14(7)	40447	115*	186	
91	CITY	30	1-50	1687-1943	12850	1x1	6.73	2.50	14(7)	49438	526*	791	
92	CITY	30	1-100	1687-1943	25700	1x1	7.30	3.46	14(7)	5948	1049*	3601	
93	CITY	30	1-976	1687-1943	62951	2x2	8.79	7.05	28(17)	57551	3961*	24670	
94	CITY	30	1-976	1687-1943	15860	4x4	8.77	6.54	28(17)	21219	1540*	6779	
95	CITY	30	1-976	1687-1943	1627	1.6x16	8.65	4.69	28(17)		166*	274	
96	CITY	30	1-976	1687-1943	279	32x32	9.46	3.54	14(7)	88	34*	48	
97	FIELD A	1-10	1-118	118	1x1	30.10	7.49	24(14)	9**	17	15		
98	FIELD A	1-10	1-118	1180	1x1	31.82	10.45	44(30)	318	38**	59		
99	FIELD A	1-50	1-118	5900	1x1	32.32	11.22	52(37)	12698	64*	222		
100	FIELD A	1-100	1-118	11800	1x1	33.06	11.06	52(37)	5510	73*	235		
101	FIELD A	1-624	1-118	18408	2x2	34.39	10.07	52(37)	44119	96*	475		
102	FIELD B	1-10	1-198	199	1x1	41.98	9.54	38(25)	31	33	23**		
103	FIELD B	1-150	1-198	1980	1x1	40.80	10.93	41(28)	159	38**	48		
104	FIELD B	1-50	1-198	9900	1x1	40.28	11.35	52(37)	961	99	82*		
105	FIELD B	1-100	1-198	19800	1x1	40.56	11.31	52(37)	1477	217	134*		
106	FIELD B	1-336	1-198	26532	2x2	41°35	10.51	52(37)	5676	43**	325		
107	FIELD C	1-1	1-238	238	1x1	40.95	14.52	52(37)	427	58*	68		
108	FIELD C	1-10	1-238	2380	1x1	42.82	14.14	52(37)	403	38**	77		
109	FIELD C	1-50	1-238	11900	1x1	45.33	15.11	52(37)	1134	91*	250		
110	FIELD C	1-100	1-238	23800	1x1	45.52	15.37	52(37)	2054	116*	393		
111	FIELD C	1-624	1-238	37128	2x2	45.92	15.01	52(37)	3362	173*	871		
112	BLACK ICE	30	1-976	1-256	249856	1x1	15.99	6.65	52(37)	18954*			
113	BLACK ICE	30	1-976	1-256	2548	10x10	15.95	4.07	52(37)				
114	BLACK ICE	30	1-976	1-256	440	25x25	15.83	2.94	17(9)	798*	1132		
115	BLACK ICE	30	1-976	1-256	120	50x50	15.64	2.42	11(5)	168	30*	34	
116	BLACK ICE	30	1-10	1-256	2560	1x1	14.68	4.76	25(15)	511	273	54	
117	BLACK ICE	30	1-100	1-256	25600	1x1	15.91	6.65	25(15)	4040	918*	2236	
118	TUNDRA	30	3685-4660	1-256	249856	1x1	26.83	10.56	52(37)	3405*	6328		
119	TUNDRA	30	3685-4660	1-256	2548	10x10	26.70	6.76	29(18)	153	52	39*	

Table 8. Data Inventory (Continued)

FIGURE NUMBER	TERRAIN TYPE	DEPRESSION ANGLE	AZ SWATH	RANGE SWATH	NO. PTS.	AVGING	μ	σ	χ^2_{95} (df)	χ^2 (N)	χ^2 (L)	χ^2 (G)
120	TUNDRA	30	3685-4660	1-256	440	25x25	26.26	5.97	21(12)	13*	23	19
121	TUNDRA	30	3685-4660	1-256	120	50x50	25.58	5.63	17(9)	21*	24	24
122	TUNDRA	30	3685-3685	1-256	256	1x1	25.71	10.43	36(24)	68	38	37*
123	TUNDRA	30	3685-3694	1-256	2560	1x1	24.82	9.41	43(29)	1167	53*	96
124	TUNDRA	30	3685-3784	1-256	25600	1x1	28.19	10.95	52(37)	8148	167*	469
125	TUNDRA	30	3685-3694	1-256	2560	1x1	24.82	9.41	43(29)	1167	55*	96
126	TUNDRA	30	3685-3784	1-256	25600	1x1	28.19	10.95	52(32)	4604	154*	455
127	MOUNTAIN	60	1-100	1-50	5000	1x1	19.84	7.24	34(22)	2398	91*	103
	IPL #410-2											
128	MOUNTAIN	20	1-100	1-308	28-98	1x1	7.89	4.35	25(15)	--	3093*	3119
	IPL #412-3											
129	MOUNTAIN	30	3365-3621	1-256	65792	1x1	25.58	11.71	52(32)	7482	1442	674
	IPL #411-3											
130	MOUNTAIN	60	1-100	1-50	5000	1x1	27.01	9.52	34(22)	531	88*	131
	IPL #410-3											
131	MOUNTAIN	20	1-100	1-308	27412	1x1	7.18	3.33	18(10)	66711	4155	1333*
	IPL #412-4											
132	MOUNTAIN	30	901-1000	1-256	25600	1x1	29.81	9.90	52(37)	104*	166	687
	IPL #411-4											
133	MOUNTAIN	60	1-100	1-50	5000	1x1	27.80	10.01	40(27)	940	60*	152
	IPL #410-4											

Table 9. Figure Numbers

a. Figure Numbers for Basic Data Set

<u>Elevation</u>	<u>Mountain</u>	<u>Ice</u>	<u>City</u>	<u>Field</u>
20°	1-4	13-16	25-28	A: 37-40
30°	5-8	17-20	29-32	B: 41-44
60°	9-12	21-24	33-36	C: 45-48

Each set of four figures is arranged according to averaging over squares of pixel size: 1 x 1, 10 x 10, 25 x 25, and 50 x 50.

b. Figure Numbers for Supplementary Data Set

<u>Elevation</u>	<u>Mountain</u>	<u>Ice</u>	<u>City</u>	<u>Field</u>
20°	49-52			A: 97-101
30°	53-65	66-88	89-96	B: 102-106
60°				C: 107-111

c. Figure Numbers for Additional Data Set

<u>Elevation</u>	<u>Black Ice</u>	<u>Tundra</u>
20°		
30°	112-117	118-124
60°		

data set which is based on a variation of sample size and further averaging square sizes. Finally, additional data have been processed for black ice and tundra terrains; these are enumerated in part c of Table 9.

Figures 3, 4, and 6 show, respectively, the images of the ice, mountain, and city areas which have produced the clutter data for this study. In addition, three fields, chosen for their homogeneity of image and medium brightness of scatter, have been included for comparison purposes. They are shown in Figures 7, 8, and 9. The depression angles appropriate to their data are: Field A, Field B, Field C.

The relative sizes of mean return and especially of deviation about the means are shown in Figure 27. The reader should take account of the fact that the numbers for the city scattering should be increased by a factor of 4.74 (as is indicated on the figure) (note that the standard deviation must also be increased by the factor 4.74). The mean of city data is relatively insensitive to elevation angle; moreover, the standard deviation of city data is not only relatively insensitive to elevation angle but also to averaging square size.

For the bare mountain and pack ice data the mean and standard deviations for 20° elevation are quite similar in behavior. But for the other elevations they are not. In fact, the behavior of the bare mountain and pack ice data appears to be reversed at 30° and 60° elevations. More precisely, for moderate (25 x 25) to large (50 x 50) averaging square sizes the standard deviation behavior of homogeneous ice at 30° elevation resembles that of the bare mountain at 60°. One can readily surmise (see next paragraph) that the bare mountain topography may be at least part of the cause of this interesting standard deviation behavior with averaging square size.

The mean and standard deviation of the bare mountain data at 30° depression angle very much resemble those respective statistics for black ice at the same depression angle. In fact, their entire

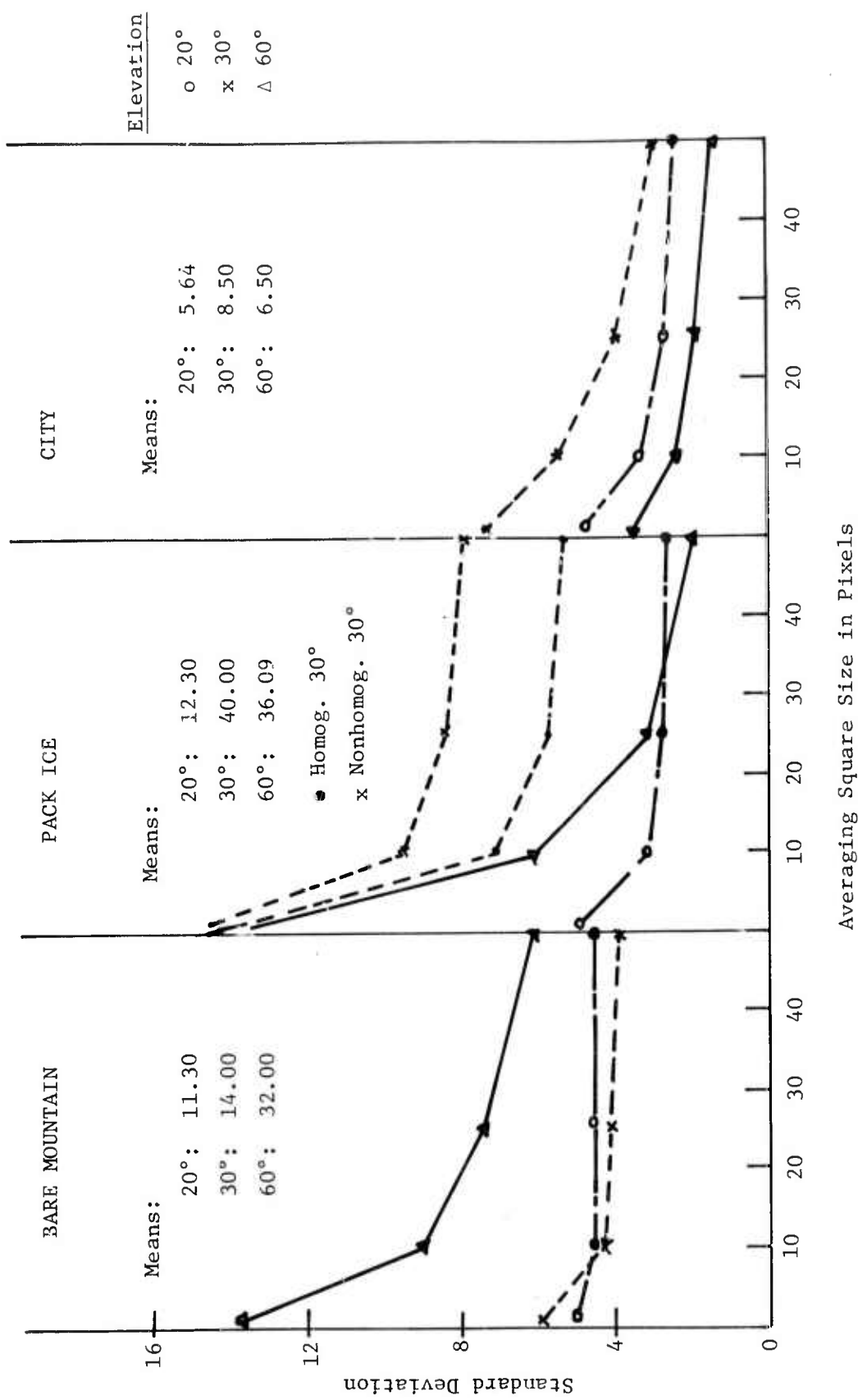
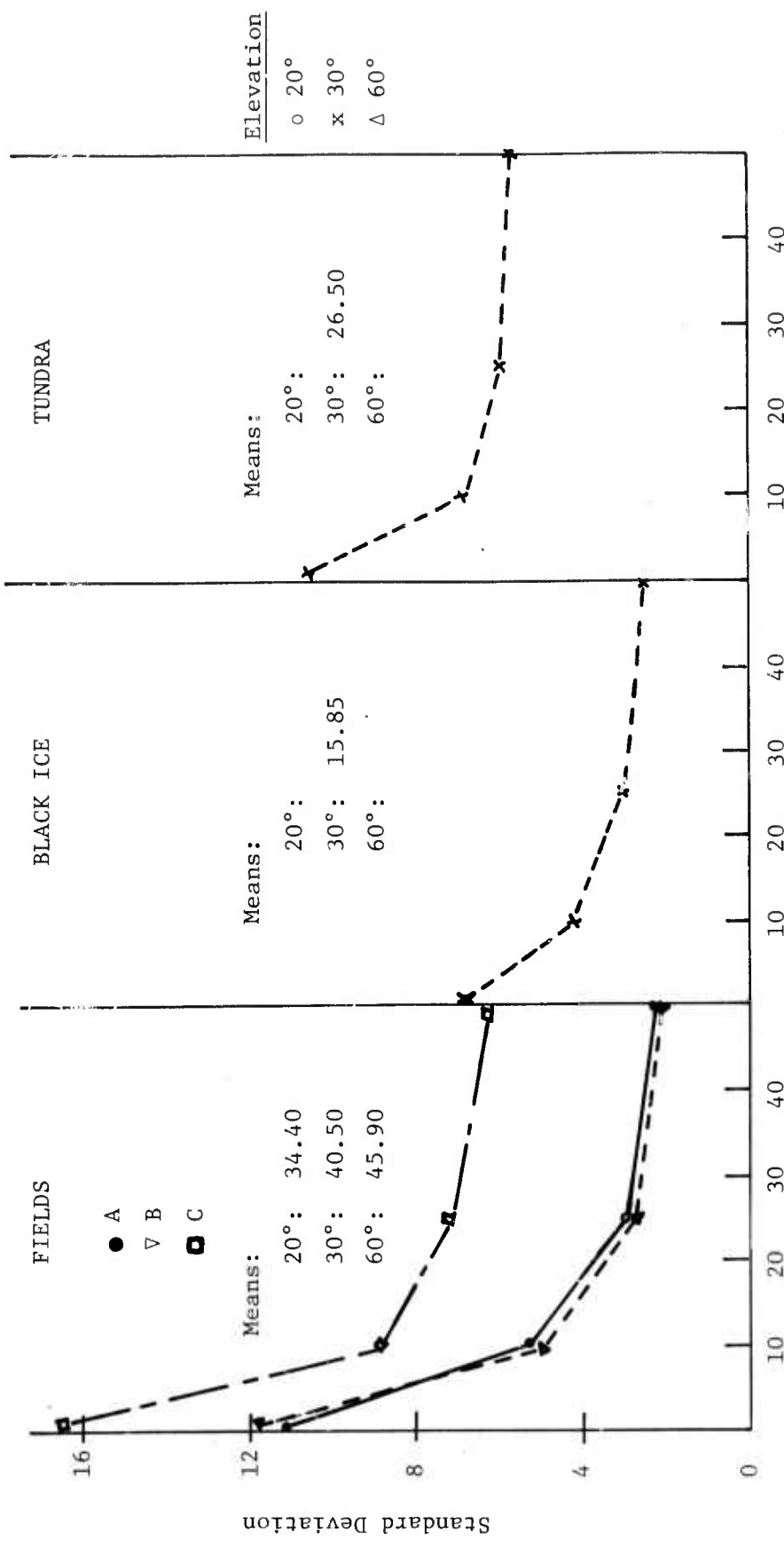


Figure 27. Standard Deviation Vs. Resolution



Averaging Square Size in Pixels

Figure 27. Standard Deviation Vs. Resolution (Continued)

distributions are quite similar, as Figure 28 shows. Now even though the mountain terrain is quite bare and in many places covered by ice (from ground truth recorded by the experimenters), one would expect somewhat higher values of σ_o than those observed in Figures 5 through 8 (and Figures 53 through 65 in Appendix I as well). Thus, a re-examination of the mountain terrain was made (see Figure 3). The area chosen for analysis, although quite homogeneous and moderately bright in the imagery, appears to be very possibly situated on a reverse slope. New sample areas were chosen for comparison and these produced much higher (10 or more dB in σ_o) mean values. The resulting wide variation in average σ_o values from bare (and somewhat icy) mountainous terrain is an important fact to be noted.

In general, with the exception of the 20° elevation cases, the standard deviation about the mean return declines steeply as averaging square size increases, and this trend is, of course, to be expected since individual scatterers have less opportunity to make their individual returns stand out.

As was remarked at the outset of this section, the distributions, both density and cumulative, for the data sets enumerated above in Tables 8 and 9 have superposed on them a normal, log-normal, and a gamma distribution. These three analytic distributions are chosen to have mean and standard deviation equal to the mean and standard deviation for the data histogram, whether or not any of the three distributions is an acceptable fit by the chi-square test. In fact, some of the chi-square statistics for the normal, log-normal, and gamma distributions are ridiculously high in comparison to the test chi-square statistic for the data in question. But they are included, whether they are high or not, to indicate which analytic distribution best fits the data, however badly or well.

To indicate at a glance which distributions best fit the various data sets, a tabulation is given in Table 10. In more than half of the cases, the log-normal distribution provides the best fit, with the

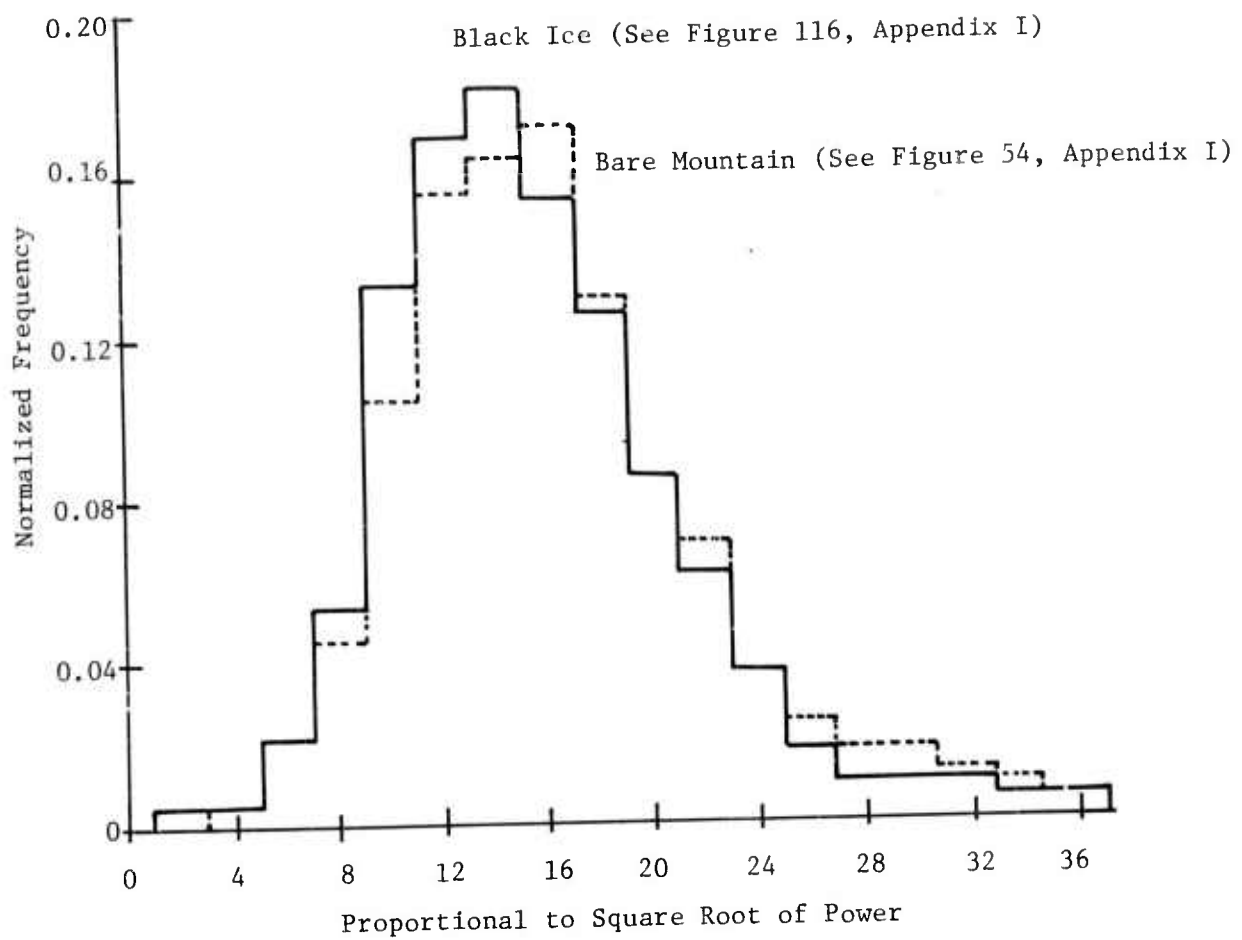


Table 10. Fitting Distributions

		Mountains			Ice			City			Fields		
		20	30	60	20	30	60	20	30	60	A	B	C
(100's)	Small Sample	G	G		G			L			L	G	L
(1000's)	Medium Sample	N	G		L			L			L	L	L
(10,000's)	Large Sample	G	G	L	L	L	L	L	L	L	L	L	L
(10 x 10)	Small Res.	N	G	L	N	G	L	-	L	L	L	L	L
(25 x 25)	Medium Res.	N	G	L	N	N	N	G	L	L	L	L	L
(50 x 50)	Large Res.	G	G	L	N	N	G	G	L	G	G	L	L

		Black Ice			Tundra		
		20	30	60	20	30	60
(100's)	Small Sample		L			G	
(1000's)	Medium Sample		G			L	
(10,000's)	Large Sample		L			L	
(10 x 10)	Small Res.		-			G	
(25 x 25)	Medium Res.		L			N	
(50 x 50)	Large Res.		L			N	

gamma and normal distributions appearing more frequently (the gamma twice as often as the normal) as resolution (or averaging) size is increased.

It is of considerable interest to compare not only means and standard deviations of the data, as has been done above, but also to compare the histograms themselves for the various terrain types. Such a comparison is made in Figure 29 for bare mountain, pack ice, field B, and tundra [the data are actually taken from Figures 54 (mountain), 70 (pack ice), 103 (field B), and 123 (tundra) of Appendix I]. The pack ice distribution has the longest tail, while the bare mountain has the shortest. Field B and the tundra distributions are quite similar in shape but the field B distribution is displaced considerably to the right, because of its larger mean, of the tundra distribution.

3.4 CORRELATION RESULTS

Let ξ be a random variable whose behavior is described by the density function $p(\xi)$. The expectation E of a function $f(\xi)$ is taken as

$$E[f(x)] = \int f(\xi) p(\xi) d\xi, \quad (22)$$

where the integration is taken over the defined domain of ξ . The mean μ and standard deviation σ used in this discussion are well known [9]:

$$\mu = E[\xi] = \int \xi p(\xi) d\xi \quad (23)$$

$$\sigma^2 = E[(\xi - \mu)^2] = \int (\xi - \mu)^2 p(\xi) d\xi \quad (24)$$

Let η be a second random variable with density $q(\eta)$. If $\mu_{\xi\eta}$ is the joint central moment

$$\mu_{\xi\eta} = E[(\xi - \mu_{\xi})(\eta - \mu_{\eta})], \quad (25)$$

9. H. Cramér, "Mathematical Methods of Statistics," Princeton University Press, Princeton, 1958.

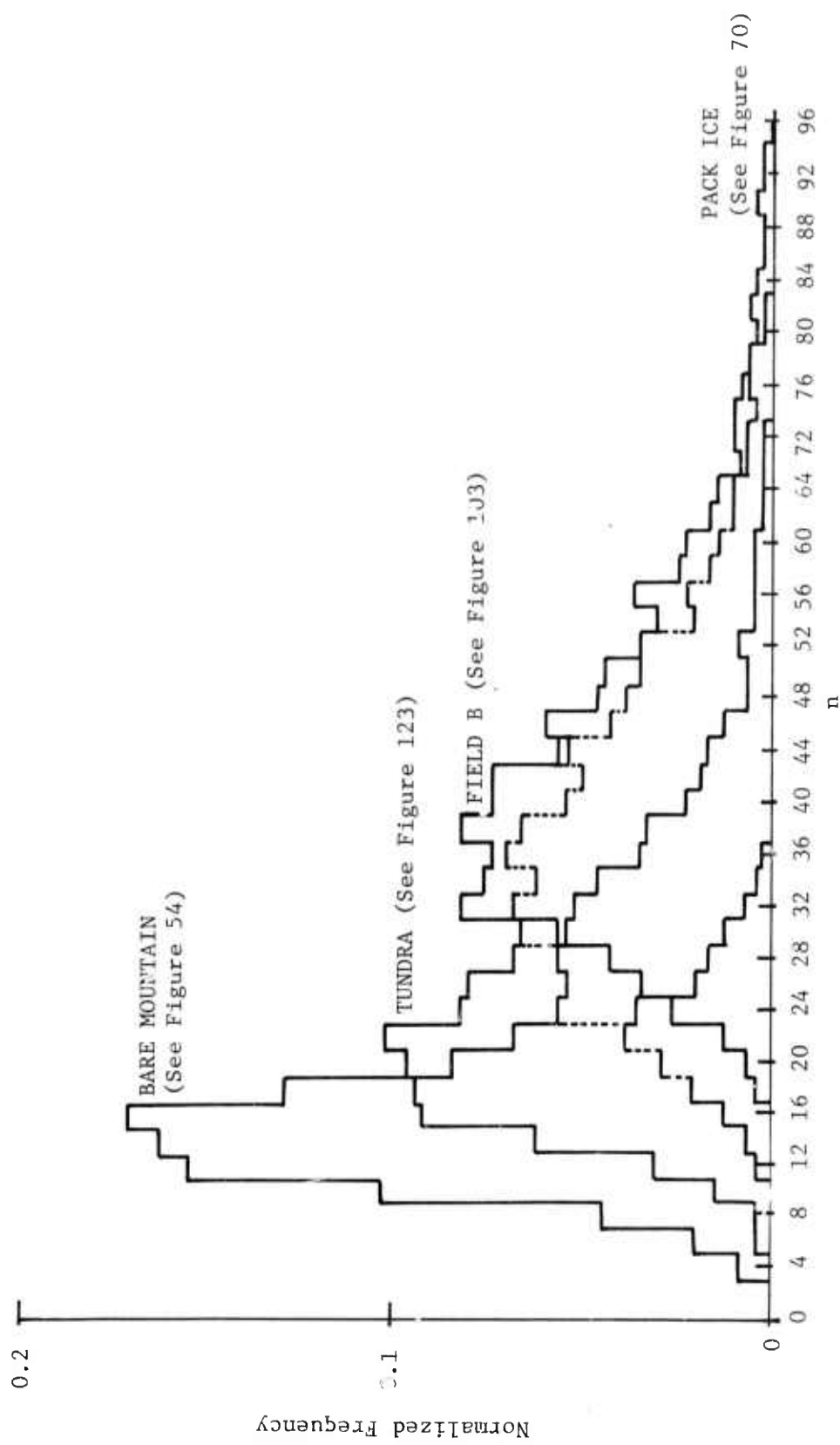


Figure 29. Comparison of Histograms

then the correlation ρ between the random variables ξ and η is defined to be

$$\rho = \frac{\mu_{\xi\eta}}{\sigma_{\xi} \sigma_{\eta}} \quad (26)$$

where the subscript denotes the variable to which the statistic pertains. If the expectation $\mu_{\xi\eta}$ is expanded, one obtains the alternative correlation formula

$$\rho = \frac{E[\xi\eta] - \mu_{\xi} \mu_{\eta}}{\sigma_{\xi} \sigma_{\eta}} \quad (27)$$

The correlation coefficient ρ has the range $-1 \leq \rho \leq 1$.

The definition (26) affords

$$\frac{y - \mu_{\eta}}{\sigma_{\eta}} = \rho \frac{x - \mu_{\xi}}{\sigma_{\xi}} \quad (28)$$

as a best linear mean square regression of η by means of ξ , i.e., the square of η minus a linear function of ξ , viz.

$$\left\{ \eta - \left[\left(m_{\eta} - \frac{\rho \sigma_{\eta}}{\sigma_{\xi}} \right) + \frac{\rho \sigma_{\eta}}{\sigma_{\xi}} \xi \right] \right\}^2,$$

is as small as possible. Alternatively, a best linear mean square regression of ξ by η produces

$$\frac{y - \mu_{\eta}}{\sigma_{\eta}} = \frac{1}{\rho} \frac{x - \mu_{\xi}}{\sigma_{\xi}} \quad (29)$$

If ρ is 1, or -1, then the whole mass of the distribution is located on a straight line. If ρ is 0 then (28) reduces to $y = \mu_{\eta}$ and (29) reduces to $x = \mu_{\xi}$ which are lines parallel to the y - and x -axes, respectively, and the random variables ξ and η are independent.

The above definitions and interpretation of correlation ρ have been applied to the clutter data as follows. Suppose there are N lines of data between two desired azimuths, each line containing M pixels corresponding to the same fixed range interval. A sample of MN values from a random variable ξ is created by arranging in tandem the N azimuth lines (of M pixels each). If a circular arrangement of the MN pixels is made by closing the last with the first, then the second random variable is generated by shifting the data through some desired number of points. The result is actually an auto-correlation. More precisely, let $x(m)$, $m = 1, 2, \dots, MN$, represent the sample points, with $x(MN + m) = x(m)$. Then the correlation coefficient ρ becomes (from Eq. (27)

$$\rho(n) = \frac{E[\xi(\xi + n)] - \mu_{\xi}\mu_{\xi+n}}{\sigma_{\xi}^2} \quad (30)$$

The bare mountain terrain data have been examined for two cases at the 30° depression angle (both from IPL 411, File 1, Flt. 2/23/77, Pass 4 (L-band)). The first set is a sample of 256 range points from azimuth line 3301. The autocorrelation coefficient

$$\rho(n), n = 1, 2, \dots, 10 \quad (31)$$

is determined and plotted to show the actual values of $\rho(n)$. Figure 30 contains the results. For example, one reads that $\rho(5) = 0.27967$, while $\rho(1) = 0.83421$.

Figure 30. Correlation Coefficients (n) , $n = 1, \dots, 10$ for 1 Line of Bare Mountain Data (IPL 407, File 5, Pass 2)

The second set is a sample of 25600 points from the 100 azimuth lines 3301 through 3400 (i.e., the range swath is 1-256 and the azimuth swath 3301-3400). The results for $\rho(n)$, again for $n = 1, \dots, 10$, are shown in Figure 31. This time one finds $\rho(5) = 0.32559$ and $\rho(1) = 0.85329$.

COEFFICIENTS	
1	.85329
2	.67369
3	.49924
4	.38286
5	.32559
6	.30190
7	.28951
8	.28143
9	.27260
0	.26308
1	.38112
2	.49916
3	.61720
4	.73524
5	.85329

Figure 31. Correlation Coefficients $\rho(n)$, $n = 1, 2, \dots, 10$ for 100 Lines of Bare Mountain Data (IPL 407, File 3, Pass 2)

SIMULATION OF RADAR SIGNALS FROM AN
R, \dot{R} CLUTTER MAP

The clutter data statistics were generated for the purpose of generating clutter models for northern region terrain types, as an input for the generation of space radar clutter in the form of magnetic data tapes. A necessary part of this effort was to prepare a space radar system model which simulates the impact of sensor system parameters on clutter. This simulation addressed the effects of platform orbit, antenna pattern, waveform bandwidth, and viewing geometry. This simulation of radar signals from a range (R) and range rate (\dot{R}) clutter map is described in this section.

The procedures developed were integrated into a computer program which was used to model the effect of the radar transfer function and to synthesize time-dependent radar returns from ground clutter in order to create data tapes which can simulate signals at the output of the analog-to-digital converter. These tapes contained approximately the equivalent of 150 msec of radar signal at 10 MHz simulated bandwidth. Both in-phase (I) and quadrature phase (Q) channels were provided. Also, target signature data was analyzed and target signals synthesized in a compatible format to be used with the clutter tapes.

The clutter signal as a function of time (t) is given as

$$c(t) = c_0 \int_{R, \dot{R}} A(R, \dot{R}) e^{4\pi j t R / \lambda} s(t - 2R/c) dR d\dot{R} \quad (1)$$

where $s(t)$ is the waveform, c_0 is a complex constant, λ is the wavelength, R is the range, c is the speed of light, R is the range rate, $j = \sqrt{-1}$, and $A(R, \dot{R})$ is the complex reflection coefficient of clutter whose expected value $E|A(R, \dot{R})|^2$ is the clutter RCS per unit range and range rate. The latter, the clutter RCS density, or "clutter map" is a subject in itself and requires careful modeling to faithfully include effects of viewing geometry and terrain type. It requires antenna patterns, platform and earth motion, and viewing angles. Equally important and least well-defined is the sigma-zero model which is also required. Essentially the radar cross-section per unit area for every point on the earth, could be handled by maps based on actual clutter data, a stochastic model based on probability distributions and spatial correlations of actual data, or a suitable combination of the two. Realistically, the last solution is probably the most suitable in most cases.

For notational simplicity we define the following quantities

$$\begin{aligned} t' &= 2 R/c \\ v' &= 2 R/\lambda \\ w &= e^{-2\pi j} \\ w_N &= e^{-2\pi j/N} \end{aligned}$$

Hereafter, j can be used as an index as well as $\sqrt{-1}$ since its meaning should be clear from context.

For the moment consider the waveform to be a weighted train of δ function pulses

$$s(t) = s_0 \sum_{n=0}^{N-1} w_n \delta(t - n\Delta) \quad (2)$$

where s_0 is a constant, w_n is a set of complex weights and Δ is the inter-pulse period. The δ -function is defined such that for an arbitrary function g :

$$\int_{-\infty}^{\infty} g(t) \delta(t - t') dt = g(t')$$

Substituting (2) into (1) and integrating yields

$$c(t) = c_0 s_0 \sum_n \int_{-\infty}^{\infty} dv' A(t - n\Delta, v') w^{-tv'} w_n \quad (3)$$

Now suppose that $c(t)$ is sampled at discrete times $t_0 + m\Delta$ for N samples (pulses).

$$\begin{aligned} c(t_0 + m\Delta) &= c_0 s_0 \sum_n \int_{-\infty}^{\infty} dv' A(t_0 + m - n)\Delta, v') w^{-m\Delta v'} w_n \\ &= c_0 s_0 \sum_n \int_{-\infty}^{\infty} dv' A(t_0 + n\Delta, v) w^{-m\Delta v'} w_{m-n} \\ &= \sum_n c_n(t_0 + m\Delta) \quad -(N-1) \leq n \leq N-1 \end{aligned} \quad (4)$$

where $c_n(m\Delta) = c_0 s_0 \int_{-\infty}^{\infty} dv' A(n\Delta, v') w^{-m\Delta v'} w_{m-n}$.

Hereafter, the reference time t_0 will not be noted unless referred to specifically.

Consider the discrete Fourier transform (DFT) of $c_n(m\Delta)$ given by

$$\begin{aligned} c_n(v) &= \sum_{m=0}^{N-1} c_n(m\Delta) w^{m\Delta v} \\ &= c_0 s_0 \int_{-\infty}^{\infty} dv' A(n\Delta, v') \sum_{m=0}^{N-1} w^{m\Delta(v-v')} w_{m-n} \\ &= c_0 s_0 \int_{-\infty}^{\infty} dv' A(n\Delta, v') x_n(v - v') \end{aligned} \quad (5)$$

where

$$\begin{aligned} x_n(v - v') &= \sum_{m=0}^{N-1} w_{m-n} w^{m\Delta(v - v')} \\ &= \text{DFT}(w_{m-n})^* \\ n &= 0, \pm 1, \dots, \pm(N - 1). \end{aligned} \tag{6}$$

From (5) and the "additive" property of the DFT, we note that

$$c(v) = \text{DFT}(c(t)) = \sum_n c_n(v) \tag{7}$$

Thus a procedure for computing $c(t)$ is

1. compute $A(R, \dot{R})$
2. compute $x_n(v)$ $- (N - 1) \leq n \leq N - 1$ by Eqn 6
3. compute $c_n(v)$ $- (N - 1) \leq n \leq N - 1$ by Eqn 5
4. compute $c(v)$ by Eqn 7
5. inverse DFT to compute $c(t)$.

This procedure is undesirable, however, for several reasons which can be remedied by considering the following alternate procedure.

This alternate procedure makes use of the fact that temporal and spectral clutter samples are independent. Unlike the first method, this allows the major portion of the work to be performed with real quantities $\bar{\sigma}(R, \dot{R})$ and $|x_n(v)|^2$, where

$$\bar{\sigma}(R, \dot{R}) = \overline{|A(R, \dot{R})|^2} \tag{8}$$

The bar over a quantity denotes the expected value of the quantity.

* Note that DFT is used both as an abbreviation for discrete Fourier transform and as a function representing the result of the discrete Fourier transform of the variable(s).

In addition to being real, x^2 and $\bar{\sigma}$ are now deterministic and, therefore, far fewer random numbers need to be generated and these only in the later stages of the process.

Consider the expected value of the square of $c_n(v)$

$$|c_n(v)|^2 = |c_0|^2 |s_0|^2 E \left\{ \int_{-\infty}^{\infty} dv' dv'' A(n\Delta, v') A(n\Delta, v'') \right. \\ \left. \times x_n(v - v') x_n^*(v - v'') \right\} \quad (9)$$

The statement that spectral samples are independent can be expressed as

$$E [A(n\Delta, v') A^*(m\Delta, v'')] = \bar{\sigma}(n\Delta, v') \delta(v - v'') \delta_{mn}$$

where $\delta_{mn} = \begin{cases} 1 & \text{if } m = n \\ 0 & \text{otherwise} \end{cases}$ (10)

Therefore,

$$|c_n(v)|^2 = |c_0 s_0|^2 \int_{-\infty}^{\infty} dv' \bar{\sigma}(n\Delta, v') x_n^2(v - v') \quad (11a)$$

$$\text{and } |c(v)|^2 = \sum_n \overline{|c_n(v)|^2} \quad (11b)$$

Note further that since x_n^2 is computed from a regular, discrete sample, it is a periodic function whose period is equal to the pulse repetition frequency, $\text{PRF} \equiv f_r = 1/\Delta$. Thus it is possible to break-up $\bar{\sigma}(n\Delta, v')$ into a sum as follows:

$$\bar{\sigma}(n\Delta, v') = \sum_k \bar{\sigma}_k(n\Delta, \bar{v}') \quad k = 0, \pm 1, \dots, \pm \infty \quad (12)$$

where

$$\begin{aligned} \bar{\sigma}_k(n\Delta, \bar{v}') &= \bar{\sigma}(n\Delta, \bar{v}' + kf_r) & 0 \leq \bar{v}' < f_r \\ &= 0 & \text{otherwise} \end{aligned} \quad (13)$$

Now we have

$$\overline{|c_n(v)|^2} = |c_0 s_0|^2 \int_0^{f_r} dv' \sum_k \bar{\sigma}_k(n\Delta, v') x_n^2(v - v') \quad (14)$$

The right-hand-side of (14) is a periodic convolution and is most efficiently done using the convolution theorem and fast Fourier transform (FFT). The convolution-theorem is written as follows:

$$\text{If } z_n = \sum_{m=0}^L x_n \bar{y}_{n-m} \quad (15a)$$

where \bar{y} is periodic, $\bar{y}_n = y_{n+kL}$, $k = 0, \pm 1, \dots, \pm \infty$, then

$$z_n = \frac{1}{L} \sum_m A_m B_m W_L^{-nm} = \text{inverse DFT}(AB) \quad (15b)$$

$$\text{where } A_m = \sum_\ell x_\ell W_L^{m\ell} = \text{DFT}(x) \quad (15c)$$

$$B_m = \sum_\ell y_\ell W_L^{m\ell} = \text{DFT}(y) \quad (15d)$$

We apply this theorem to Eqn (14) with the approximation

$$\int_0^f dv' \longrightarrow \frac{f}{L} \sum_{m=0}^{L-1} \quad (16a)$$

$$\text{and } v' = mf_r/L \quad (16a)$$

The integer L must be chosen such that each "lobe" of $x_n^2(v)$ is sampled at least twice. This requires, if there are N pulses, that $L \geq 2N$.

Now we have the following procedure for computing $\overline{|c(v)|^2}$ for $v = \frac{mf_r}{L}$, $m = 0, 1, \dots, L-1$.

$$1. \quad \text{Compute } \overline{\sigma}(R, \dot{R}) - \begin{cases} R = n\Delta c/z & -1 \leq n \leq N-1 \\ R = \frac{mf_r \lambda}{4N} & 0 \leq m \leq 2N-1 \end{cases}$$

$$2. \quad \text{Compute } x_n^2(v), \quad n = 0, \pm 1, \dots, \pm (N-1)$$

for $v = mf_r/2N$, $m = 0, \dots, 2N-1$

$$3. \quad \text{Convolve } \overline{\sigma} \text{ with } x^2 \text{ using (15) and (16).}$$

$$4. \quad \text{Sum over } n \text{ to obtain}$$

$$\overline{|c(v = mf_r/2N)|^2} \equiv \overline{|c_m|}$$

$$5. \quad \text{Smooth to obtain } N \text{ distinct samples from the } 2N \text{ available points.}$$

$$6. \quad \text{Compute } c_m = |c_m| e^{i\phi_m}. \quad \text{Here } |c_m| \text{ is a Rayleigh distributed random variable with expected value } \sqrt{|c_m|^2} \text{ and } \phi_m \text{ is a random variable uniformly distributed between } 0 \text{ and } 2\pi.$$

7. Inverse DFT to obtain the sequence
8. Repeat for every required value of t_0 .

At this point it is worthwhile to describe the physical significance of Steps 1 through 8 above.

Step 1 is the production of a valid clutter map taking into account terrain features and viewing geometry. The procedure is documented elsewhere and involves a translation of area in earth coordinates into radar coordinates (R, R) weighted by appropriate factors in the radar equation (e.g., antenna pattern, σ^0 model, and R^4 factor). For a realistic simulation the σ^0 model should reflect a grazing angle dependence and appropriate terrain mix. In addition, fluctuation from mean value and spatial correlations should be included either by means of a stochastic model or by using actual unsmoothed σ^0 data.

Step 2 is the computation of the cross ambiguity function x^2 of the transmitted waveform with no receive weights (receive weights will be included in simulated processing of the simulated signal produced here). This is done by the FFT algorithm.

Step 3 is the convolution of x^2 with the expected clutter in frequency space. Physically each point of the convolution is the expected clutter at that frequency taking into account Doppler ambiguities and Doppler sidelobes.

Step 4 is the summation of each of the ambiguous range strips into one equivalent Doppler spectrum.

Step 5 is simple combining points which lie in the same Doppler filter.

Step 6 is the production of a signal spectrum having Rayleigh statistics and whose expected magnitude squared equals that computed in Steps 1 through 5.

Step 7 is simply the computation by DFT of the time sequence of radar pulses at the receiver.

Step 8 is not really a separate step but a reminder that the process must be repeated for every range resolution cell to be processed. The results for the numerous range strips are not independent since they all come from a clutter map (Step 1) which takes into account spatial correlations.

There is another step which could be called Step 9 which has not been mentioned heretofore. Since the pulses have a finite width and some frequency modulation, the single pulse waveform (assuming each pulse is identical except for a complex weight) must be convolved with the time sequence generated in Steps 1 through 8. This is derived mathematically below. In essence it folds together results of nearby range cells, leaving it up to the pulse compression process of the processing simulation to untangle them.

This procedure is valid only for δ -function waveforms of the type (3). In general the waveform will be a train of identical pulses of finite length. This is given by

$$s(t) = \int_{-\infty}^{\infty} dt' s_0(t') T(t - t')$$

where $T(t)$ is a train of δ -function as in (3), and $s_0(t)$ is the envelope of the individual pulses.

Equation 3 now becomes

$$\begin{aligned} c(t) &= c_0 s_0 \int dv' \int dt' A(t', v') w^{-tv'} \int dt'' \sum_n \delta(t - t' - t'' - n\Delta) \\ &\quad \times w_n s_0(t'') \\ &= c_0 s_0 \sum_n \int dv' \int dt'' A(t - t'' - n\Delta, v') w^{-tv'} w_n s_0(t'') \\ &= \int c^1(t - t'') s_0(t'') dt'' \text{ where } c^1(t) \text{ is now given by (3).} \end{aligned}$$

Since the process of convolving a long sequence

$$c^1(t^0 + m\Delta) \quad t_{\min} \leq t^0 \leq t_{\max}, m = 0, \dots, N - 1$$

with a short one such as $s_0(t)$ (the individual pulse length is certainly less than Δ and probably much shorter) is straightforward, it seems appropriate to first compute $c^1(t)$ and then convolve it with $s_0(t)$ by means similar to the FFT convolution algorithm (15).

5
SUMMARY

The above sections of Volume I and the appendices in Volume II contain Labrador Sea clutter data taken at L-band, HH polarization. These data cover pack ice (and refrozen lead), bare mountains, tundra, and black ice. For comparison purposes data are also included for a city (Toronto) and three homogeneous fields. Methods of measurement, recording, and processing (including calibration, digitization, and imagery) of the data, as well as the test sites, are described in Section 2. These clutter data are, of course, best described by statistical quantities. Section 3 gives a preliminary examination of some of the statistics by which the data can be characterized. If the data are to be used to formulate a mathematical model for target detection and/or tracking in the presence of clutter, then it is useful to learn whether various types of clutter data can be fitted by analytic distributions. Section 3 also addresses this question and finds that the log-normal distribution seems to be the number one candidate for most acceptable fitting distribution. There seems to be some promise that an analytic distribution, such as the log-normal, can be contaminated (see section 3.2.3) so as to produce a distribution whose fit is acceptable to a statistical test such as the chi-square.

The numerical values of the data, resulting from digitization of recorded signals, are proportional to the square root of intensity (or received power). These numerical values provide a convenient basis in terms of which to do further processing and analysis. This approach has been used exclusively in the above discussions. It is, however, straightforward, with the help of the calibration information, to convert these square-root-of-intensity numbers into radar cross section per unit illuminated area $\bar{\sigma}_0$. This conversion is done for averages of square-root-of-intensity numbers for pack ice, bare mountain, field, and city (Toronto) data in order that they may be compared with existing data.

Figure 32 contains the results, showing $\bar{\sigma}_0$ vs. depression angle

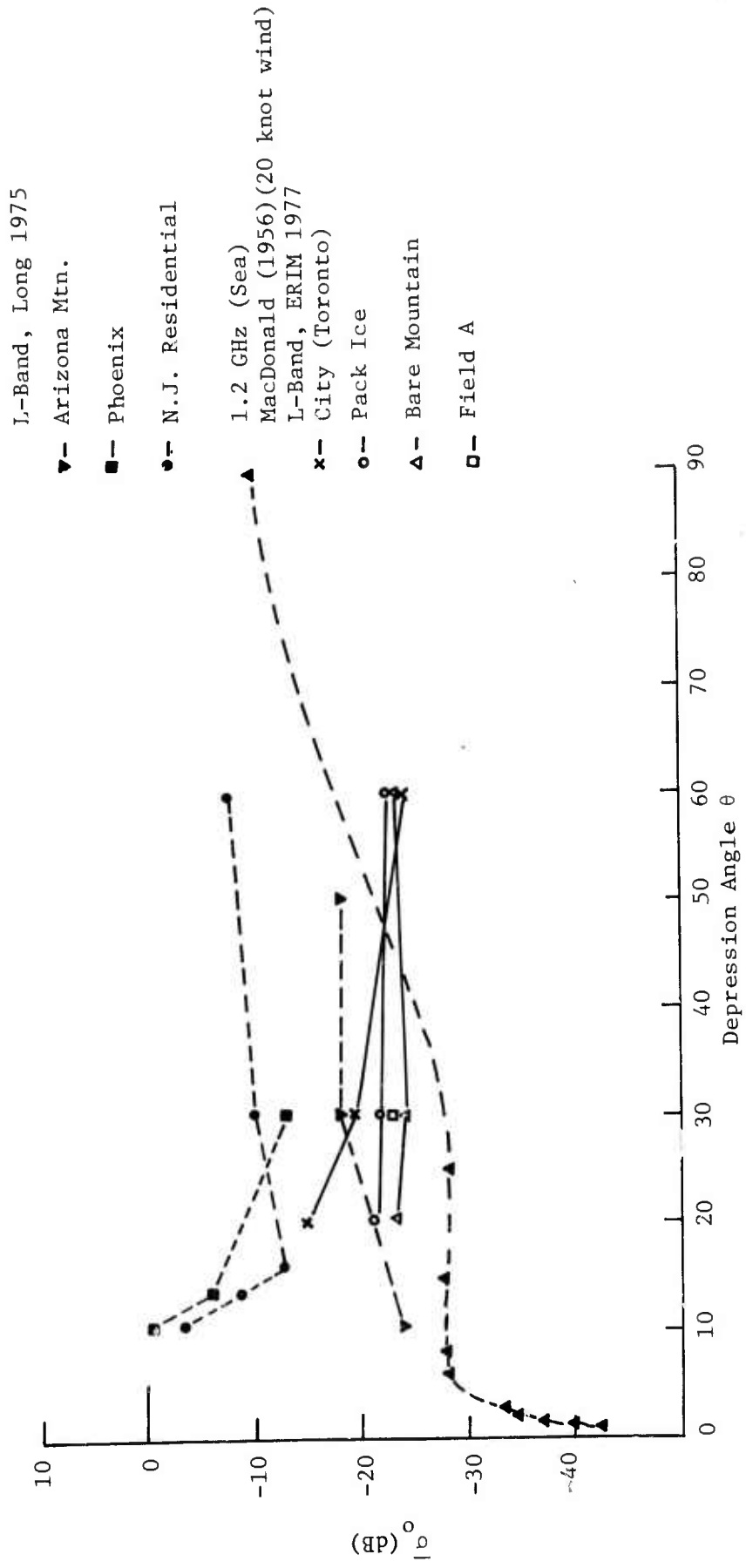


Figure 32. Comparison of L-Band Clutter Data from Various Terrain Types
 (Solid Lines: ERIM Data; Dashed Lines: Ref. Data)

θ . The city data are highest valued at the 20° depression angle, being about -15 dB on the average. This level of $\bar{\sigma}_0$ then falls off to approximately -20 dB at $\theta = 30^\circ$, and still further to about -24 dB at $\theta = 60^\circ$. It seems quite reasonable that the largest values should occur at smallest depression angles since there the buildings form dihedrals with the longest base sides. However, the city $\bar{\sigma}_0$ levels recorded in Figure 32 are some 6 to 15 dB below levels for Phoenix and a New Jersey residential area reported by Long [4], with the largest difference occurring at $\theta = 60^\circ$ for the New Jersey residential area. Rooftops may be largely responsible for the higher return from this New Jersey residential area.

The bare mountain data agree rather well with the Arizona mountain data from Long, the former being only some 6 to 8 dB lower. Such lower values of the mountains of the Labrador Sea area could very well be attributable to their smoothness and to the fact that large shadow areas (on reverse slopes) can be present in a given scene.

L-band clutter data are in short supply. So to provide added material for comparison, one sea data curve from MacDonald, 1956, [10] is included in Figure 32. The data are for a sea under a 30 knot wind and thus may be reasonably comparable with the pack ice data. One sees in fact only a 5 or so dB difference between them.

The field data provide only one $\bar{\sigma}_0$ value at $\theta = 30^\circ$. The field was homogeneous and was chosen for its fairly bright image. Thus, it should and does compare well with the pack ice which appeared to have about the same level of return in the imagery.

10. F. C. MacDonald, "The Correlation of Radar Sea Clutter on Vertical and Horizontal Polarizations with Wave Height and Slope," 1956 IRE Convention Record, Pt. 1, pp. 29-32, 1956.

In summary then, the clutter data for the pack ice, bare mountain, city, and field seem to provide quite believable $\bar{\sigma}_0$ values which are in reasonable agreement with the small amount of L-band clutter data presently existing in the literature.

The ERIM clutter data presented in Figure 32 has some interesting aspects. One would normally expect the $\bar{\sigma}_0$ curves to decrease with smaller depression angles. The city data exhibits the opposite dependence, i.e., the $\bar{\sigma}_0$ increases with decreasing depression angle. This is probably explained by the large flat sided buildings found in cities. The radar return becomes more specular at low depression angles. A similar dependence is observed on the pack ice data. The pack ice $\bar{\sigma}_0$ changes by approximately 3 dB between 20° and 60° depression angle and shows a larger $\bar{\sigma}_0$ at 20° than it does at 60°. This would seem to go against ones intuition even though the difference is only 3 dB. This small reversal in the slope of the curve could be due to calibration errors.

One of the fundamental assumptions inherent in the calibration procedure was that the antenna pattern was reasonably accurate and that any deviation of the measured values of RCS from the computed values for the corner reflectors was due to errors in the RCS of the corner reflectors. In retrospect, this may not be the case. The difference could have been due to antenna gain variations in the elevation plane. Again using hindsight, it probably would have been better to assume that the corner reflectors were of the correct RCS and that any differences between calculations and measurements were due to deviations from the antenna patterns used for the calculations.

Section 4 contains a description of a radar signal simulation by Philip Tomlinson of Decision-Science Applications, Inc. This simulation was used to provide magnetic tape data for use in testing signal processor techniques. This simulation is capable of accepting as input the clutter data and statistics generated on this program. However, much more can be done with the more extensive data now available.

CONCLUSIONS AND RECOMMENDATIONS

The data presented and discussed in this report are valuable additions to the very small amount of existing data on L-band terrain clutter. They represent a rather small percentage of the total amount of data recorded over the entire Labrador Sea measurement flight. Thus, there is available a virtually untapped mine of data for various types of terrain (and sea) clutter. A sufficient amount of analysis is now in-hand to offer a rather tantalizing possibility for the characterization of these data.

Although this data is not fully amplitude calibrated, the partial calibration used allows one to draw some conclusions with respect to this L-band clutter data. The principle conclusions are:

1. The clutter statistics generated on this program appear to be well behaved. This is a good indication that the hardware and software implementations used are performing satisfactorily.
2. The log-normal distribution seems to be the number one candidate for most acceptable fitting distribution for data whose amplitudes are proportional to the square root of intensity. There seems to be some promise that an analytic distribution, such as the log-normal or the gamma, can be contaminated (see section 3.2.3) so as to produce a distribution whose fit is acceptable to a statistical test such as a chi-square.
3. The clutter data for pack ice, bare mountain, city and field provide σ_0 values which are in reasonable agreement with the small amount of L-band clutter data presently existing in the literature.
4. When the resolution cell size is increased, i.e., when the data are averaged over range-azimuth rectangles of increasing size, the standard deviations of the resulting distributions of averaged data decrease correspondingly. The rates of standard deviation decrease vary with incidence angle as well as with the type of terrain.

The following recommendations are made with regard to additional work in clutter statistics by ERIM, RADC, or other organizations. There is now a rather complete computer program library to generate clutter statistics which will make the analysis of clutter data more efficient in the future.

1. Since some questions remain on the behavior of the clutter data at the smaller depression angles, the attempted calibration at these angles should be repeated using the assumption that the RCS of the corner reflectors imaged is correct. This technique avoids the problem of knowing the antenna pattern and it does not restrict calibration to depression angles where there are corner reflectors, i.e., 26° , 27° , 30° , 42° , and 44° .
2. The radar simulation derived by DSA and described in Section 4 of this report was used to provide magnetic tape data for use in testing signal processing techniques. However, with the more extensive data now available, more realistic radar clutter data simulation could now be performed. It is recommended that work continue in the areas of appropriate statistics, generation of clutter "maps" and on determination of the spatial correlations of actual data.
3. In order to analyze the data at coarser resolutions corresponding to specific radar designs, long (160 km) strips of data can be digitized and analyzed. The 160 km strip could be digitized with 100 m range resolution and a variety of cross range resolutions. This would lead to an investigation of clutter statistics as a function of terrain types along a continuous 160 km strip. The statistics thus derived would apply directly to the design parameters of the space based radars being considered. The software developed on the present program can be used to derive the required statistics.
4. There are a number of tasks which would improve accuracy and establish additional credibility to the clutter statistics. These would concentrate on analyzing and interpreting the results. The present calibration technique can be analyzed to establish achievable accuracy. The computer programs can be extended to normalize out the R^{-3} term and the antenna elevation gain pattern from the digitized data. This presently restricts us to looking at statistics along track and over small elevation angles.

Other statistical distributions can be examined and compared including:

- a. contaminated log-normal
- b. contaminated gamma (or chi-square)
- c. Beckmann Distribution,
- d. Rice Distribution (or chi), and
- e. Hoyt Distribution.

In addition, it may also be useful to attempt a nonparametric estimation of a density function. Also, other statistical tests can be studied to further define a "good fit". Other tests besides the chi-square which can be examined are:

- a. Komolgoroff-Smirnov Test,
- b. Snedecor Test,
- c. Runs Test.

The spatial correlation properties of the data, as well as spatially varying properties of the distributions, can also be examined.

5. In order to derive a parametric model for clutter, one can study the relationship of radar cross-section per unit area (σ^0) as a function of wavelength, polarization, aspect angle, terrain type, etc. A model then could be used in analytic or simulation radar performance evaluations.
6. The present work could be extended to X-band (using available data) and to sea clutter at X-band and L-band.
7. Cross-polarized data can be used to investigate whether the use of a cross-polarized channel can result in a significant decrease in clutter return. This would include a review of limited data in the L- and X-band cross polarized channels of the ERIM radar and comparison to the same polarization channels.
8. If future programs justify extensive additional data collection, then we would recommend that adequate amplitude calibration instrumentation and procedures be added to the X-L radar to ensure accurate calibration.
9. The ERIM X- and L-band dual polarization radar used to collect the imagery used in this program is in the process of being transferred into another aircraft. The new aircraft (a convair 580) will be used in a pilot program to determine microwave sensor requirements for Canada.

This program will generate a minimum of 15,000 line miles (54,000 square miles) of radar imagery. Included in the data set will be agricultural areas, wildlife preserve areas, and forested areas. Also included will be ice studies from both coast lines as well as the artic regions. The open ocean and coastal areas will also be imaged.

The imagery collected during this program (July 78 through April 79) will be available to ERIM for clutter statistics analysis.

There is at the present time no funding for adding amplitude calibration to the X-L radar. The value of the data collected could

be enhanced by:

1. Adding amplitude calibration
2. Conducting an error analysis on the present system to put error bounds on the data.

This system will remain available to ERIM and its sponsors for the duration of the program through the normal channels.

REFERENCE LIST

1. D. A. Ausherman, "Radar Data Processing and Exploitation Facility," Record from the IEEE International Radar Conference, 1975.
2. G. T. Ruck, "Radar Cross Section Handbook," Penum Press, 1970.
3. R. L. Cosgriff, W. H. Peake, R. C. Taylor, "Terrain Scattering Properties for Sensor System Design," Engineering Experiment Station Bulletin 181. Ohio State University, 1960.
4. Maurice W. Long, "Radar Reflectivity of Land and Sea," D.C. Heath and Company, Lexington, Mass., 1975.
5. J. Aitchison and J. A. C. Brown, "The Log-Normal Distribution," Cambridge Univ. Press, 1957.
6. G. V. Trunk and S. F. George, "Detection of Targets in Non-Gaussian Sea Clutter," IEEE Trans. AES, Vol. AES-6, pp. 620-628, Sept. 1970.
7. P. Beckmann, A. Spizzichino, "The Scattering of Electromagnetic Waves from Rough Surfaces," MacMillan Company, New York, 1963.
8. D. E. Kerr, "The Propagation of Short Radio Waves," MIT Rad. Lab., Series #13, McGraw-Hill, 1951.
9. H. Cramér, "Mathematical Methods of Statistics," Princeton University Press, Princeton, 1958.
10. F. C. MacDonald, "The Correlation of Radar Sea Clutter on Vertical and Horizontal Polarizations with Wave Height and Slope," 1956 IRE Convention Record, Pt. 1, pp. 29-32, 1956.

THIS REPORT HAS BEEN DELIMITED
AND CLEARED FOR PUBLIC RELEASE
UNDER DOD DIRECTIVE 5200.20 AND
NO RESTRICTIONS ARE IMPOSED UPON
ITS USE AND DISCLOSURE.

DISTRIBUTION STATEMENT A

APPROVED FOR PUBLIC RELEASE,
DISTRIBUTION UNLIMITED.